# Numerical simulation of morphogenetic movements in Drosophila embryo

Rachele Allena

# Numerical simulation of morphogenetic movements in *Drosophila* embryo

## THÈSE

présentée et soutenue publiquement le 16/09/2009

pour l'obtention du

**Doctorat de l'Ecole Centrale Paris**

**(spécialité mécanique)**

par

Rachele Allena

sous la direction de D. Aubry

**Composition du Jury**

| | |
|---|---|
| *Président :* | D. Barthès-Biesel (UTC - Genie Biologique) |
| *Rapporteurs :* | J. Muñoz (Universitat Politècnica de Catalunya)<br>P. Tracqui (Equipe DynaCell, Laboratoire TIMC) |
| *Examinateurs :* | E. Farge (Institut Curie)<br>A. Mouronval (Ecole Centrale Paris) |

**Laboratoire de Mécanique des Sols, Structures et Matériaux - CNRS U.M.R. 8579 - 2007-03**

$asap\ \ fsl^{PhD}$

# Aknowledgements

In this section of the work *remerciements obligent*.

First of all: no jury, no thesis. Therefore I would like to thank all the members of the committee not only for their presence at my defense, but also and especially for the time they have spent reading my manuscript.

Particular thank you to Emmanuel Farge and his passion for the *Drosophila Melanogaster*, which has made possible this work. Even if sometimes it seemed to me very hard to catch your biological-physical vocabulary, as an engineer I have been pleased to work with you.

Thanks to Emmanuel Beaurepaire, Anne-Sophie Mouronval and José Muñoz for the interesting and helpful discussions.

I, me and myself say *un enorme grazie* to Denis Aubry: it has been amazing to share with you my thoughts, even the silly ones!

Special thanks to Amélie, Elsa, Ghizlane and Sofia the best co-bureau ever...you are the best cadeau of MSSMat!

Finally to *mssmat.tous@ecp.fr* and to all those people with whom I have laughed, cried, kidded around and many others during these last three years: *grazie, grazie di cuore*!

# Motivation

Ourselves and all the endless forms we can observe around us are just the final result of a series of complex and still enigmatic processes that regulate nature. It is astonishing to discover little by little that we are part of an immense scheme where each single component knows exactly where to go, what to do and when and how to do it. Still more fascinating is to find out that the smallest parts of this system, at first sight the simplest ones, are instead the most organised and fundamental for the success of the global plan. Cells can for sure be included in this category.

A cell is like a "social being": alone, even if extremely intelligent, it can not completely express itself, but together with other cells it can do unbelievable things. They are able to divide, proliferate, migrate and many others, but more importantly they strongly co-operate to give rise to amazing 3D organisms. From the beginning of the embryogenesis therefore, everything is perfectly synchronized and the slightest imperfection may compromise the final result.

Since ever biologists have observed and studied intriguing developmental phases, trying to unveil the cryptic process by which an embryo is transformed in a living organism. Then mechanics may be very helpful in deciphering part of the whole problem. Each modification of the embryonic structure is actually driven by forces generated within the cells that properly react and respond so that the global architecture changes, but the embryo can progressively perform more specialised functions.

The strong connection between mechanics and genetics has been studied for a long time, showing how genes control and influence the occurrence of many morphogenetic movements during embryogenesis. Only recently the inverse process has been detected; it seems in fact that some mechanical forces might induce the expression of specific genes, elsewhere than their usual area of action in the embryo.

Therefore two main conclusions can be drawn. First, embryonic cells, as similarly as other types of cells in nature, are mechanosensible and able to adapt themselves when an external load is applied on them. Second, a mechanotransduction pattern is present in the early embryo, so that a mechanical stimulus is transformed into a chemical signal. If cells behaviour has been largely analyzed and explained through many and different experiments on cultures, it is still not so clear how mechanics transform a genetic information into a physical form. It would have been too ambitious to try to cover this gap, but at least with the present study we would like to

offer to the reader an exhaustive description of part of this complex process that is embryogenesis.

The huge advances made in numerical modeling allow today to couple together biology and mechanics. Therefore it is possible not only to investigate those systems that so far appeared unapproachable, like the embryo, but also and more surprisingly to discover that the minimal change of peculiar parameters may provide unexpected and unordinary results. In this work we use computer simulations to reproduce some of the most interesting and studied events of *Drosophila Melanogaster* development. The main goal is to provide a useful support for biologists in order to confirm their hypotheses resulted by experimental observations, but also and especially to point out unexplored aspects so that new issues are suggested.

# Thesis outline

The present thesis is developed through four principal chapters. The first one provides a brief but rather exhaustive description of the context, with a global overview on the complex process of the embryogenesis in *Drosophila Melanogaster*. We amply focus on the three morphogenetic movements that will be numerically simulated, with particular emphasis on both the mechanical and the biological aspects that constitute the main peculiarity of each event. Also we propose a short review on the related previous works.

The second chapter supplies the abstract tools for the analysis of the whole problem and points out the hypotheses that, for sake of simplicity, have been made. The gradient decomposition method is presented together with some interesting interpretations that better clarify the approach and put forward novel issues that have to be considered. By the Principle of the Virtual Power, we are able to write the mechanical equilibrium of the system which consists of the forces internal to the embryo domain and of the boundary conditions, such as the yolk pressure and contact with the vitelline membrane, that are essential for consistent results. A special concern is attributed to the choice of the constitutive law of the mesoderm that, from a biological point of view, may appear too simplistic. Here a Saint-Venant material is used in contrast with the Hyperelastic models found in literature; therefore a comparison between the two is proposed together with the advantages and the limitations of our study. Finally, we provide some simple examples that validate our model and support the exploited method.

The third chapter can be divided into two parts. In the first one, by the parametrical description of the embryo geometry, we obtain the analytical formulations of the active deformation gradients for each morphogenetic movement according to the elementary forces introduced. Such expressions will be combined with the passive gradients in order to get the final deformation of the tissues. In the second part we interpret the results for each simulation. In particular, we provide a parametrical analysis for the simulation of the ventral furrow invagination, while for the germ band extension a comparison with experimental data is done. Furthermore we have been able to estimate the effects induced by the local deformations within the tissues; specifically, we have evaluated the magnitude of the pressure forces and the shear stress that may develop at long distance in the embryo when the active forces

are applied in restraint regions. To conclude, we propose a collateral study on the influence of the global geometry of the embryo on the final results.

Given the consistence of the results for the individual simulations, we have decided to test the concurrent simulation of the events, by two or three of them. In the last chapter, we show the results for a first essay for which we use the most intuitive method; it does not require in fact further manipulations of the analytical formulations previously obtained, but we simply couple together the active deformation gradients, following the chronological order of the movements. Although the method works well for the simulation of the two furrows, some drawbacks are detected when we introduce the germ band extension. Therefore we propose a new approach, more rigorous and appropriate, which allows to take into account some aspects so far put aside, but still significant for a realistic and complete reproduction of the different phases of the *Drosophila* gastrulation.

# Resumé

Ce travail de recherche a eu comme objectif principal la conception d'un modèle numérique aux éléments finis donnant une représentation réaliste des mouvements de l'embryon de la *Drosophila Melanogaster*. Les simulations de trois mouvements durant la phase de gastrulation de l'embryon ont été realisées soit individuelles soit simultanées, ce qui jusqu'à présent, n'a jamais été proposé, constituant ainsi une contribution originale de cette étude.

La thèse est composée de quatre chapitres. Le premier fournit une brève mais assez complète description du contexte dans lequel ce travail se situe. Le processus complexe de l'embryogénèse chez la *Drosophila Melanogaster* est presenté en se focalisant sur les trois mouvements morphogénetiques qui seront ensuite simulés numériquement: l'invagination du sillon ventral, la formation du sillon céphalique et l'extension de la bande germinale. Chaque événement est décrit du point de vue biologique et mécanique, ce qui permet donc de mettre en avant les aspects les plus intéressants des différents mouvements. Une revue des plus récents travaux est aussi proposée à fin de

Dans le deuxième chapitre on présente les outils analytiques pour l'analyse du problème dans son intégrité. Etant donnée la complexité du système biologique, plusieurs hypothèses ont été introduites pour simplifier l'approche numérique utilisée. Seul le mésoderme est modélisé comme un milieu continu dans un espace tridimensionel par un ellipsoïde épais régulier de $500\mu m$ de longueur. La méthode de la décomposition du gradient de déformation, dont quelques interprètations alternatives sont presentées, permet de coupler les déformations passives et actives subies par chaque point matériel du milieu. L'équilibre mécanique est écrit à partir du Principe des Puissances Virtuelles: les forces internes du système sont donc prises en compte avec les conditions aux limites. Dans notre cas particulier celles-ci sont fondamentales pour obtenir des configurations finales réalistes et comprennent le contact entre le mésoderme et la membrane vitelline externe et le pression exercée par le yolk sur la surface interne du mésoderme. Les propriétés mécaniques des tissus embryonnaires ne sont pas faciles à déterminer expérimentalment. Une approximation a été faite pour ce qui concerne la loi de comportement du mésoderme qui a été modélisé comme un matériau de Saint-Venant linéaire, élastique et isotrope. Notre choix étant en contraste avec le modèle hyperélastique qu'on retrouve souvent en litéra-

ture, une comparaison entre les deux matériaux est proposée tout en considérant les avantages et les limitations de notre démarche. La méthode de la décomposition du gradient de déformation a été auparavant testée sur des cas géométriquement très simples dont la solution analytique peut être facilement calculée et validée par les résultats obtenus à partir des simulations numériques.

Le troisième chapitre peut être divisé en deux parties distinctes. Dans la première, grâce à la description paramétrique de l'ellipsoïde qui représente l'embryon, on calcule les expressions analytiques des positions intermédiaires où on voit apparaître les déformations actives responsables de chaque mouvement morphogénétique. Les gradients de déformation active sont donc couplés avec les gradients passifs pour obtenir la déformation finale. La deuxième partie du chapitre concerne l'analyse des résultats pour les simulations individuelles des événements. Pour la simulation de l'invagination du sillon ventral une étude paramétrique a été conduite pour évaluer l'influence de certains paramètres sur la configuration finale. Pour la simulation de l'extension de la bande germinale les résultats ont été comparés avec les données expérimentales. En particulier on s'est intéressé à l'analyse des contraintes mécaniques (les pressions et les contraintes de cisaillement) induites au niveau du pôle antérieur où un chemin de mécanotransduction aurait lieu et conduirait à l'expression du *twist*, un gène normalement exprimé seulement dans la partie ventrale de l'embryon. Pour conclure, d'autres géométries que celle de l'ellipsoïde ont été utilisées pour les simulations de l'invagination du sillon ventral et de l'extension de la bande germinale. Ces nouvelles représentations de l'embryon permettent de prendre en compte deux aspects intéressants: d'un côté l'arrondissement des deux pôles, de l'autre l'aplatissement de la partie dorsal par rapport à la partie ventrale.

Le dernier chapitre du manuscrit introduit la simulation simultanée des trois mouvements qui a été mise en place pour deux raisons principales. Tout d'abord le fait que les événements analysés se produisent l'un après l'autre lors du développement de l'embryon. Deuxièmement, les résultats obtenus pour les simulations individuelles sont très encourageants et ont permis aussi de confirmer plusieurs hypothèses avancées par les biologistes; d'où l'intérêt de coupler les mouvements pour permettre une vision encore plus réaliste de cette phase importante de la gastrulation chez l'embryon de la *Drosophila Melanogaster*. Deux méthodes différentes ont été testées. La première, la plus intuitive et simple, permet de combiner les gradients de déformation active de chaque mouvement et ne requiert pas de manipulations supplémentaires des équations précédemment trouvées, tout en prenant en compte le déphasage réel entre les événements. Cette approche ne pose pas de problèmes quand seulement les deux sillons sont couplés, alors que l'introduction de l'extension de la bande germinale donne lieu à quelque limitations. Une nouvelle démarche est donc proposée, plus rigoureuse et précise, qui nous a permis de considérer certains aspects importants pas encore développés d'un point de vue théorique.

# Contents

# List of Figures

# Chapter 1

# Introduction

This chapter can be divided into two parts. The first one provides a general overview of the embryogenesis so that the reader may get familiar with the embryo vocabulary (Sec. 1.1). The different phases of *Drosophila* embryo development are described with particular emphasis on the biological aspects of the process (Sec. 1.2). In the second part instead, we focus on the three morphogenetic movements that are numerically simulated later; ventral furrow invagination (Sec. 1.2.3), cephalic furrow formation (Sec. 1.2.4) and germ band extension (Sec. 1.2.7). We first describe the different class movements to which the specific events previously mentioned belong (Sec. 1.2.2, 1.2.5); then we switch to a more detailed analysis of each event pointing out the mechanics of the problem, without omitting the influence exerted by specific genes on them. Aware that mechanical modeling plays an important role in the understanding of the different phases of embryogenesis, we also present a review of the works we have found in literature. Particularly, Sec. 1.2.3.1 is dedicated to ventral furrow invagination while Sec. 1.2.6 to convergence-extension movements.

## 1.1 Embryogenesis

Embryogenesis - how the tissues and organs of the developing embryo take their forms - is a very complex process which has traditionally been explained in terms of genes, hormones and chemical gradients. Usually it begins once the egg has been fertilized and it involves multiplication of cells (by mitosis) and their subsequent growth, movement and differentiation into all the tissues and organs of a living insect. Given the remarkable similarity in genes responsible for organizing the fundamental body plan in vertebrates and invertebrates, in the last few years the field of insect embryology has played a significant role in the understanding of developmental processes of humans and other vertebrate organisms. Even if much of insect embryology still remains mysterious, there has been a notable progress in knowledge thanks to new methods in molecular biology and genetic engineering. Particularly, it

has recently been shown that biomechanics plays an important role in the formation, repair and function of bones, organs and arteries (Holzapfel [2000], Taber [2004]), but it plays an equally important role at the scale of cells and the scale of the embryo. For this reason, developmental processes have been largely studied in terms of mechanics and physics, although still little is known on how a genetic information can be translated via mechanics (i.e. forces and movements) into a physical form.

Insect embryogenesis can be described through a precise series of common stages; in the next section we provide a general overview (also refer to LeMoigne and Foucrier [2004] and to Forgacs and Newman [2006]) of the processes involved. Later on we will focus on *Drosophila Melanogaster* development, which is the object of the present study; the analysis of three specific morphogenetic movements will point out the strong connections between biology and mechanics. Actually, it has been recently shown that not only genetics may control mechanical forces and deformations of the embryo, as it has been observed and demonstrated so far, but also the vice versa can occur and therefore mechanotransduction and mechanosensibility paths may be analyzed and taken into account (Brouzés and Farge [2004], Farge [2003]).

### 1.1.1 General overview of insect embryogenesis

An insect's egg is much too large and full of yolk to simply divide in half like a human egg during its initial stages of development; for this reason, insects "clone" the zygote nucleus by mitosis without cytokinesis through 12-13 division cycles to yield about 5000 daughter nuclei. This process of nuclear division is known as superficial cleavage; once formed, the cleavage nuclei migrate through the yolk toward the perimeter of the egg and they subside in the band of periplasm where they construct the membranes to create individual cells. The final result of the cleavage is the blastoderm, a one-cell-thick layer of cells surrounding the yolk. The first cleavage nuclei to reach the vicinity of the oosome are "reserved" for future reproductive purposes, thus they do not travel to the periplasm and do not form any part of the blastoderm. Instead, they stop dividing and form germ cells that remain segregated throughout much of embryogenesis: these cells will eventually migrate into the developing gonads and only when the adult insect finally reaches sexual maturity they will begin by meiosis to form gametes of the next generation. This means that germ cells never grow or divide during embryogenesis, therefore DNA is conserved from the very beginning of the development. The principal reason of this strategy is to minimize the risk of an error in replication that would accidently be passed on to the next generation.

The blastoderm cells start enlarging and multiply on one side of the egg and this region, called germ band or ventral plate, is exactly where the embryo's body will develop. The rest of the cells become part of a membrane, the serosa, that forms the yolk sac; these cells grow around the germ band, enclosing the embryo in an amniotic membrane.

At this stage of embryogenesis, when the embryo is composed by a single layer of

cells, a specific group of control genes, the so called homeotic selector genes, become active. These genes, by proteins with special active site, bind with the DNA and interact with particular locations in the genome where they activate or inhibit the expression of other genes. Practically, each selector gene, within a restricted domain of cells according to their location in the germ band, controls the expression of other genes that produce hormone-like "organizer" chemicals, cell-surface receptors and structural elements. Also the selector genes guide the development of individual cells and channel them into different functions. Such process is called differentiation and continues until the fundamental body plan is mapped out; firstly into general regions along the anterior-posterior axis, secondly into individual segments and finally into specialized structures or appendages.

When the germ band starts enlarging, it is possible to observe it lengthening and folding so that its final shape corresponds to a layer of cells on the outside, the ectoderm, and another one on the inside, the mesoderm. Once the lateral edges of the germ band fuse along the dorsal midline of the embryo, the dorsal closure occurs. At this stage, ectodermal cells grow and differentiate forming the epidermis, the brain, the nervous system and most of the insect's tracheal system. Furthermore, the ectoderm folds inward at the front (foregut) and rear (hindgut) regions of the digestive system. On the other hand, mesodermal cells differentiate to form other internal structures such as muscles, glands, heart, blood and reproductive organs. The midgut generates from a third layer, the endoderm, which arises near the fore and hindgut invaginations and eventually fuse with them to complete the alimentary canal.

During early development, the embryo looks most like a worm and only later first segments become visible near the anterior end, to move through the thorax and the abdomen. Generally, the rate of embryonic development is influenced by the temperature and by the specific characteristics of species. The entire process ends when the yolk's contents have been completely consumed so that the insect is fully formed and ready to hatch the egg. The eclosion may take place by a chewing of the insect through the egg's chorion or simply the insect can swell in size until the egg shell cracks along a predetermined line of weakness. Contrary to the general thought, the larva does not end its development with the hatching process, but it will continue to develop and mature.

## 1.2 *Drosophila* embryo

*Drosophila melanogaster* is a two-winged insect that belongs to the species of the flies. The species is usually known as the common fruit fly and it is the most studied organism in biological research, particularly in genetics and developmental biology. There are several reasons:

- it is small and easy to grow in laboratory;
- it has a short generation time (about two weeks) so several generations can be studied within few weeks;
- it presents high fecundity;
- it has only four pairs of chromosomes;
- genetic transformation techniques have been available since 1987;
- its compact genome was sequenced and first published in 2000 (Adams et al. [2000]).

*Drosophila melanogaster* has also some similarities with the human embryo; in fact 75% of known human disease genes have a recognizable match in the genetic code of fruit flies and 50% of fly protein sequences have mammalian analogues (Reiter [2001]). Embryogenesis in *Drosophila* has been extensively studied since the small size and short generation makes it ideal for genetic studies. It is also unique among model organisms in which cleavage occurs in a synctium.

### 1.2.1 Stages of development

The embryonic development of *Drosophila melanogaster* has been subdivided into 18 stages by Hartenstein and Campos-Ortega (Campos-Ortega and Hartenstein [1985], Fig. 1.1). The egg is bilaterally symmetrical and distinction between the dorsal and ventral surfaces is indicated by differences in curvature, in fact the dorsal side is flattened while the ventral side is somewhat convex. The dimensions of the egg are variable; an average length is $500\mu m$, the diameter is about $150\mu m$. The mature egg is enclosed by two envelopes, an inner homogeneous vitelline membrane and an outer tough, opaque chorion, which is ornamented with hexagonal and pentagonal figures representing the impressions of the ovarian follicle cells on the original soft membrane.

Following fertilization and mitosis, nuclear division begins, however cytokinesis, division of the cytoplasm, does not occur in the early *Drosophila* embryo, resulting in a multinucleate cell called syncytium or syncytial blastoderm. The common cytoplasm allows morphogen gradients to play a key role in pattern formation. At the tenth nuclear division, the nuclei migrate to the periphery of the embryo and at the thirteenth division, the 6000 or so nuclei are partioned into separate cells. This occurs at the fifth stage which corresponds to the formation of the cellular blastoderm. Although not yet evident, the major axes and segment boundaries are determined. Subsequent development results in an embryo with morphologically distinct segments. It is at stage sixth that gastrulation starts. Gastrulation is the invagination of the blastula creating the mesodermal and ectodermal germ layers

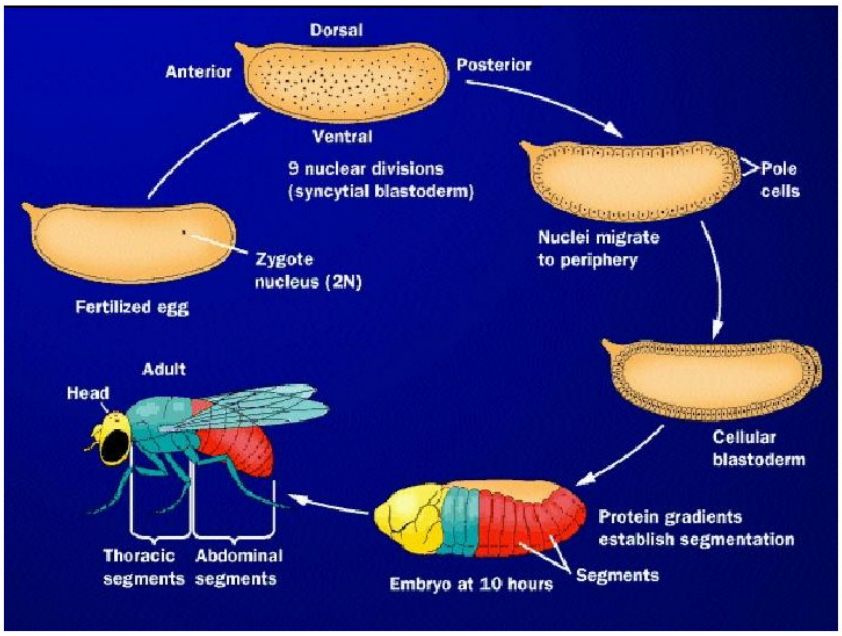


*Figure 1.1:* Successive phases of *Drosophila* embryo development (http://biology.kenyon.edu).

and usually is a very complex phase of the development of vertebrates; in the fly it is overwhelming. There is not just a single site for cell invagination, but taken together, one finds approximatively ten morphogenetic movements, three of which can be considered gastrulation proper and seven more that should be analyzed in order to understand *Drosophila* embryogenesis as a whole. Of the three events one is involved in mesoderm formation, the ventral furrow invagination, and two others involve endoderm formation, both anterior and posterior midgut invagination (Costa et al. [1993]). Seven other events resembling gastrulation are listed below:

- formation of the cephalic furrow;
- formation of dorsal transverse folds;
- germ band extension;
- germ band retraction;
- segmentation;
- dorsal closure;
- head involution.

It has to be known that there are other programs of cell movement, including trachea formation, imaginal disc development and segregation of neuroblasts from the neuroectoderm. The initial structuring for most of these events can be traced back to the four maternal systems which establish polarity in the egg and, as a consequence, in the zygote. Thus these events are related to segmentation patterns built early in development. Ventral furrow formation and dorsal closure have their origin in the dorsal-ventral system; the other eight events originate with the anterior and the posterior group of maternal genes, that are responsible for anterior-posterior polarity.

Gastrulation begins three hours after fertilization; by this time there have been thirteen mitotic cycles. Prior to the tenth cycle, the dividing nuclei lie in the interior of the egg, but move out toward the surface, going through four more division cycles at the periphery until cellularization occurs (Foe et al. [1993]). Immediately after cellularization, a process taking less than a hour to complete, the ventral furrow, which marks the beginning of gastrulation, begins to form.

During *Drosophila* gastrulation it is possible to observe two major invaginations: the ventral furrow and the posterior midgut, that internalize mesodermal and posterior endodermal precursor cells respectively (Sweeton et al. [1991]). Cells that internalize by the ventral furrow invagination will give rise to the mesoderm and about eight minutes after the ventral furrow begins to form, the posterior midgut invagination starts at the posterior pole with internalization of cells rising the endoderm.

As underlined above, in *Drosophila* embryo several mechanical movements occur. Even if they take place at different stages of development and at different regions of the embryo, some of them are thought to be driven by the same coordinated changes in shape of individual cells at the site of active movement, which generate global changes in tissue organization (Costa et al. [1993], Leptin and Grunewald [1990], Leptin [1999], Keller et al. [2003]). In particular, ventral furrow and posterior midgut invagination appear to be very similar since associated with cell shape change from columnar to trapezoidal. Further support that ventral furrow and posterior midgut formation are governed by the same underlying cellular mechanisms might be obtained from mutations that specifically affect these invaginations, but leave other morphogenetic aspects of gastrulation unaffected. Two such useful loci on both invaginations are folded gastrulation and concertina. The folded gastrulation locus was originally identified by a zygothic letal mutation; in contrast, concertina is a maternal effect gene whose product is supplied by maternal transcription during ovogenesis. Many are the differences in the genetics of both mutants, but the most obvious and common defect is a failure to form a posterior midgut invagination (Sweeton et al. [1991]). Simultaneously with ventral furrow invagination at stage six, cephalic furrow forms and generates a partial necklace of inturning tissue which demarcates head from thorax in the fly.

Approximatively from stage six to stage nine, when invaginations occur, the

*Drosophila* embryo is composed by a thin layer of columnar epithelial cells. This layer of cells is surrounded by a rigid shell comprehensive of a rigid chorion and a vitelline membrane and it contains a slightly compressible viscous liquid, the yolk. If we observe the blastoderm by a cross-section, we can see an approximatively circular array of columnar cells which have the apico-basal axes aligned along the axis of radial symmetry, with the apical surfaces facing outward. It is interesting how the embryo maintains this configuration, where each cell is in contact with its neighbours, over a period of twenty minutes after which the blastoderm becomes a multilayered structure. Once the ventral furrow has formed, the thick ventral portion of the embryo consists by a one cell thick outer layer of columnar cells (ectoderm) and an invaginated inner layer of irregular shaped cells, several cells deep (endoderm). Taken together, these layers form the germ band that undergoes an extension along the anterior-posterior axis. In about 105 minutes the germ band doubles its length and halves its width; this process pushes the posterior midgut invagination closed and compresses the flattened dorsal tissue of the embryo. During germ band extension, cells shift their positions relative to one another; actually, they intercalate so that they are forced to narrow and extend.

While germ band extension is accompanied by cellular interdigitation, germ band retraction at stage twelve is coupled with the transition from a parasegmental to segmental division of the embryo. Meanwhile the dorsal tissues previously compressed spread out to cover the entire dorsal region of the embryo. At this time, deep ventral-lateral grooves form, corresponding to the segmental boundaries that will be the sites for future muscles attachment. During segmentation, the segregation of the the imaginal discs can also be observed. Imaginal discs are sacs of cells that give rise to adult structures.

Stage fourteen includes the dorsal closure which takes place progressively. It takes about two hours to complete during which stretched dorsal tissues are covered by epidermal cells that will ultimately fuse at the dorsal midline. Head involution occurs at the same time of dorsal closure; the anterior ectoderm moves to the interior, beginning with stomodeal invagination. After that advanced denticles become visible and the nerve cord starts shortening. It is finally at stage eighteen that the larva begins the process of hatching.

### 1.2.2 Invagination

Invagination is the production of a tube by local in-pushing of a surface. There are two forms of invagination: axial and orthogonal. Axial invagination occurs at a point and can only produce a dent or a tube; practically the surface pushes inward directly down the axis of the tube so that a hollow column of epithelium invades the cavity of the embryo. On the other hand, orthogonal invagination takes place along a line rather than at a single point and generates a trough, the axis of which is parallel to the original surface and therefore at right angles to the direction of

invagination (Davies [2005], Fig. 1.2).

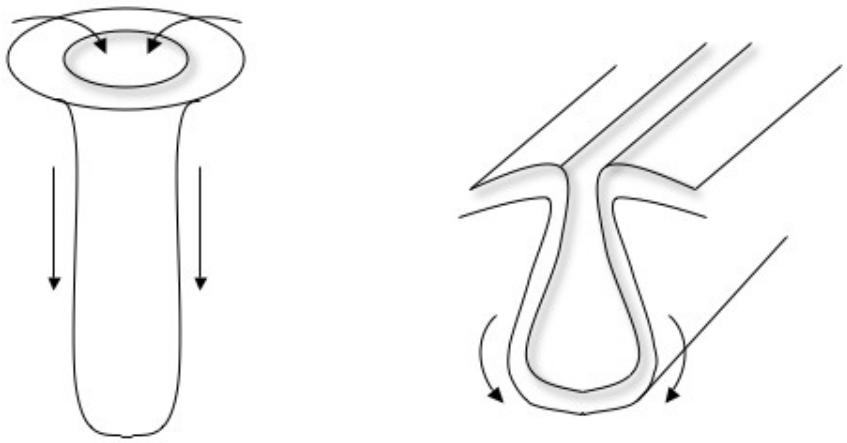

*Figure 1.2:* Axial (left) and orthogonal (right) invaginations (modified from Davies [2005]).

The invagination is locally driven and cells show a strong expression of actin/myosin filaments that run mainly circumferentially under their junctions. Actually, the contraction of these filaments squeezes the cytoplasm from the apical to the basal end of each cell and therefore expands it, so that the basal surface of the epithelium is forced to bow inward. There is therefore a local increase of the surface tension and the surface contacts between the cells are apically reduced; together with the constriction it is also possible to observe a change in the morphology of the apical surfaces. The surface of contact, that was initially convoluted, acquires a straight form which is consistent with an upregulation of cortical tension (Lecuit and Lenne [2007]). The invagination mechanism is more related to the mechanics of the extracellular matrix rather than the cells themselves. The extracellular matrix is a thick layer on the external surface of epithelial cells and it consists in an inner apical lamina and an outer layer. During invagination, the apical layer of the extracellular matrix expands while the outer layer does not and it is actually this differential expansion that forces the matrix to buckle inward. The curvature of the tissues is localized at specific hinge points and can generate convex or concave bending de-

pending on where it takes place. Therefore cells acquire a distinct wedge shape; they are apically constricted when located at the median hinge point, while basally in the case of dorsolateral hinge point (Fig. 1.3).

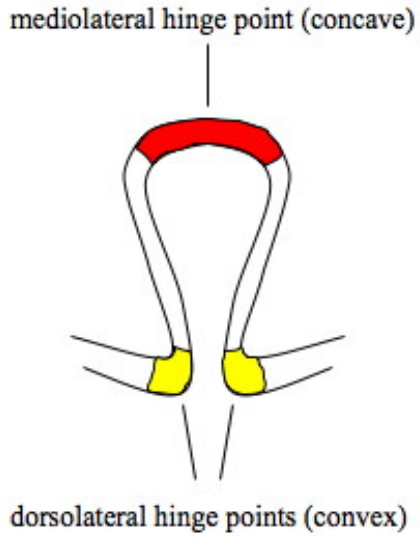


*Figure 1.3:* The hinge points during the invagination process (modified from Davies [2005]).

### 1.2.3 Ventral furrow Invagination

Ventral furrow invagination (VFI) starts at stage six at the onset of gastrulation; it is one of the most interesting morphogenetic movements in *Drosophila Melanogaster* from a mechanical point of view given the multiple elementary deformations and forces involved.

The ventral furrow is initiated as a median longitudinal cleft that extends between 20% and 70% egg length, along the ventral embryonic midline; over a period of approximately 10 minutes the ventral furrow will extend further by incorporating additional cells at its anterior and posterior tips, until it extends between 6% and 85% egg length. The ventral furrow forms as a result of cell shape changes which affect an area of about 12 cells in width centered on the ventral midline. A total of about 800 cells will become internalized through the ventral furrow: 730 cells

represent the mesoderm primordium and 70 cells represent the anterior endodermal midgut primordium (Fig. 1.4).

Ventral furrow invagination is regulated by a precise series of events. The first of them is a flattening of the apical surfaces of cells of the blastoderm, followed by the constriction of the apical domain of scattered cells within this population (Leptin and Grunewald [1990]). Once the apical changes become more widespread, it is possible to observe a superficial but effective indentation along the ventral surface of the embryo (Odell et al. [1981]). Simultaneously, cells within the furrow start elongating along their apical-basal axis until they reach almost 1.7 times their original height. Only once the furrow has formed, cells shorten back to their original length altough they maintain their apical ends constricted so that they assume a wedge-like form (Costa et al. [1993]). Even if this second event is considered to be the final step able to drive furrow invagination (Leptin [1995]), many other authors have suggested that lateral and dorsal ectodermal cells could be involved in this process pushing laterally on the sides of the embryo. This would facilitate and definitely reinforce its internalization (Costa et al. [1993], Leptin [1995], Muñoz et al. [2007]). The first result of these successive events is the formation of the ventral furrow, which is completely internalized. It is possible to observe a dispersion of single cells which divide, attach to the mesoderm and finally migrate out on the ectoderm and the mesoderm becomes then muscle and connection tissues. Simultaneously with the mesoderm, the ectoderm too starts to deform at the two poles of the embryo. The anterior endoderm invaginates as the most part of the ventral furrow. The cells of the posterior endoderm apically constrict and may invaginate while the posterior pole of the embryo is pushed dorsally by other independent elementary movements (Leptin [1999]).

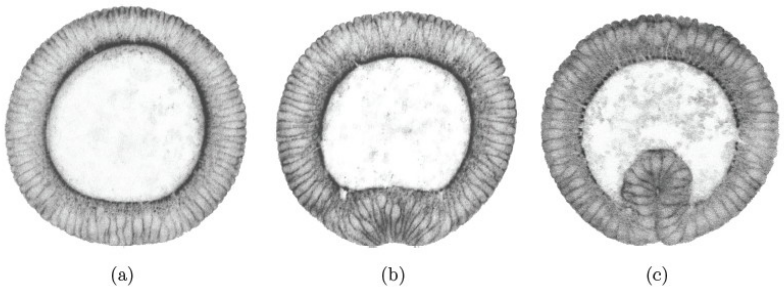


*Figure 1.4:* Successive phases of ventral furrow invagination during *Drosophila* embryo development (Conte et al. [2008]).

Where the ventral furrow invaginates is regulated by two-ventrally expressed transcriptions factors, *twist* and *snail* (Leptin [1995]). From genetic studies it has

been observed that:

- none of the morphogenetic events that accompany ventral furrow formation occurs in the absence of *twist* and *snail*;
- the co-expression of *twist* and *snail* is sufficient to generate ectopic furrows.

| *DROSOPHILA* | TWIST | SNAIL | apical flattening | apical constriction | apical-basal lengthening | apical-basal shortening | basal wedging | INVAGINATION |
|---|---|---|---|---|---|---|---|---|
| *wild* type | ✓ | ✓ | ✓ | ✓ | ✓ | ✓ | ✓ | ✓ |
| *snail* mutants | ✓ | × | ✓ | × | ✓ | × | × | × |
| *twist* mutants | × | ✓ | × | × | × | ✓ | × | × |
| *twist - snail* mutants | × | × | × | × | × | × | × | × |

*Figure 1.5:* The table shows the strong control exerted by the genes *twist* and *snail* on ventral furrow invagination. The symbols ✓/X indicate the activation/repression of the corresponding gene, the presence/absence of the corresponding cell shape change in the mesodermal primordium or the success/failure of ventral furrow invagination (Conte et al. [2008]).

*Twist* is a transcriptional activator that plays a common role in every gastrulation movements in insects (Roth [2004]). Specifically, it induces the expression, in the ventral region of the embryo, of Fog and T48 (Kolsch et al. [2007]), that recruit RhoGEF2 a contractile actin/myosin network at apical adherens junctions (Barrett et al. [1997]) to induce apical constriction of the cells. On the other hand, *twist* increases the expression of *snail*, which can actually rescue several defects observed in *twist* mutant embryos (Costa et al. [1993]). During ventral furrow formation in *Drosophila*, *snail* inhibits ectodermal cell fate; in addition it is highly required for apical constriction and may also influence the rearrangement of adherens junctions within the epithelial layer (Kolsch et al. [2007], Oda and Tsukita [2000]). A combination of *twist* and *snail* leads to ventral furrow invagination via mechanical events such as apical flattening, apical constriction, early apico-basal elongation, late apico-basal shortening and basal wedging (Fig. 1.5). Although only apical constriction and the signaling pathway inducing it are well understood so far, while information on the other forces involved in ventral furrow invagination still remain unknown or less understood. In particular, it is still difficult to distinguish, among

the deformations mentioned above, the active and the passive processes. The first ones are represented by the forces internal to each cell, which would trigger a pure deformation if the cells were isolated and not part of system, in contact with one each other. The second ones instead correspond to the passive response due to the incompatibility generated by the active deformations.

Several experimental observations have been conducted on mutant embryos in which particular aspects of the normal morphogenetic process have been genetically uncoupled. These studies have provided new information on active forces involved in furrow formation. In *twist* mutants embryos for example, the cells in the mid-ventral region elongate to the same length as in the wild type embryos, even if they do not undergo apical constriction or furrow formation. This leads to a thicker mesodermal primordium (Leptin and Grunewald [1990]); therefore apico-basal elongation is not simply a passive response to the apical constriction as nuclei and cytoplasm are pushed basally (Costa et al. [1993]). For what concerns instead *snail* mutants embryo, they show an opposite behaviour. In fact they shorten and generate a thinner mesodermal primordium, even if, also in this case, apical constriction and apical flattening do not affect the final shape of the cells so that it is possible to deduce an independence between *snail* and *twist* (Leptin and Grunewald [1990]). To conclude, it seems reasonable to think that the shape modifications mentioned above are in strong connection with one another and they drive ventral furrow invagination.

#### 1.2.3.1 Modeling of ventral furrow invagination

By previous paragraphs we can easily deduce how biomechanics plays a significant role during the different phases of embryo development. Therefore, the need more and more evident of mechanical models and in particular numerical ones, that can contribute to a complete understanding of the biological system as a whole. Computer simulations provide a realistic reproduction of the biological events and may point out interesting aspects omitted through experimental observations, so that new issues and questions are introduced.

In the last decades, several 2D models have been designed to analyze invagination (also refer to Taber [1995]). The two very first of them (Jacobson and Gordon [1976], Jacobson [1980]) focused on neurulation in the newt using experiments and geometric analysis. The authors concluded that the deformation occurring is not simply a rolling into a tube, but there is also an elongation of the neural plate in the anterior-posterior direction as the neural tube forms. Jacobson (Jacobson [1980]) also suggested that such elongation may lead to the buckling of the epithelium with a furrow forming along the direction of the stretch engendering eventually the neural tube.

The work of Odell (Odell et al. [1981]) provides an epithelial model based on apical microfilaments contraction. The main characteristics of the model are:

- the cells in the sheet are tightly bound;

- the cytoplasm is a viscoelastic solid;
- the apical surface of each cell includes a network of microfilaments. When a small amount of these filaments is stretched, they act as passive viscoelastic material, while when a threshold value of stretch is achieved, an active contractile force is developed, which remains for all time thereafter.

In order to obtain these features, each cell is represented as a four-sided, two-dimensional truss element composed by six viscoelastic units, each of which includes a spring (k) and a dashpot ($\mu$) in parallel (Fig. 1.6). The diagonal components correspond to the cytoskeleton, while the others to the cell membrane. Only the apical unit is able to actively contract.


*Figure 1.6:* Representation of a cell in the Odell's model (Odell et al. [1981]).

Each element is governed by the equation

$$F = k(L - L_0) + \mu L \tag{1.1}$$

where $F$ is the load applied at the ends, $L(t)$ is the current length and $L_0(t)$ is the inital length of the unit. The activation is obtained letting $L_0$ vary with time according to the following relation

$$L_0 = G(L, L_0) \tag{1.2}$$

where $G = 0$ for a passive unit. The model behaviour therefore depends on the choice of $G$ and the authors have chosen a relatively simple form for it, allowing

to have two stable equilibrium values for $L_0$: one for the passive zero-stress length and the other for the active zero-stress length. The model was tested for amphibian gastrulation, *Drosophila* furrow formation and amphibian neurulation (Fig. 1.7). It was found that the observed morphology could be obtained by adjusting the activation parameters in Eq.[1.2].

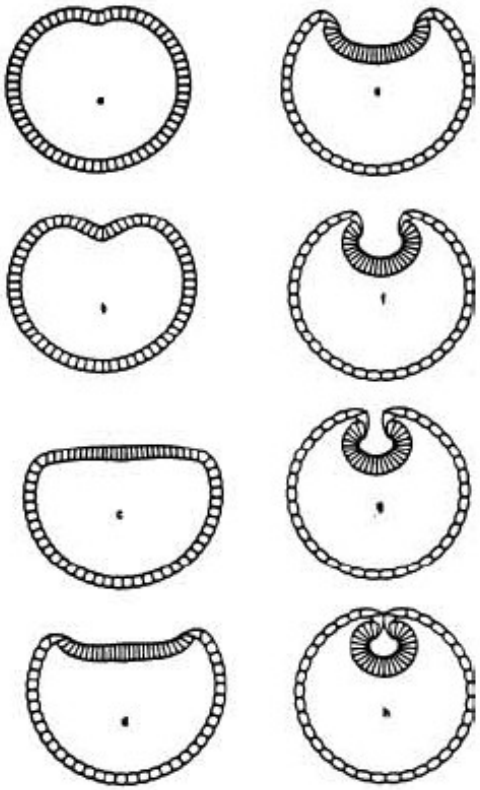

*Figure 1.7:* Results for the Odell's model (Odell et al. [1981]).

Later Oster and Alberch (Oster and Alberch [1982]) used this model to illustrate epithelial bifurcation (change in local or global stability and equilibrium) during development. Particularly, they demonstrated how, only by fairly changing the viscoelastic properties of the cells, they were able to obtain the gastrulation model buckling outward rather than inward. This behaviour may influence epithelial morphogenesis since invagination engenders hair or skin glands, while evagination leads to the formation of feathers or scale. Therefore a small variation of some parameters can induce significant global changes.

In 1986, Jacobson (Jacobson et al. [1986]) proposed a cortical tractor model in

which the motile behaviour of the epithelial cells is similar to that of mesenchymal cells. The model is based on some important assumptions:

- cytoplasm flows continuously in a cell from the basal and lateral surfaces to the apex and then back toward the base (Fig. 1.8); This flow pattern is the "cortical tractor"
- adhesion molecules enter the flow at the basal end and move with the flow to the apical end where they are resorbed;
- the resorption rate for the adhesion molecules is slower than their insertion in the flow; thus molecules accumulate at the apex keeping the cells bound together at the apical surface (Fig. 1.8).

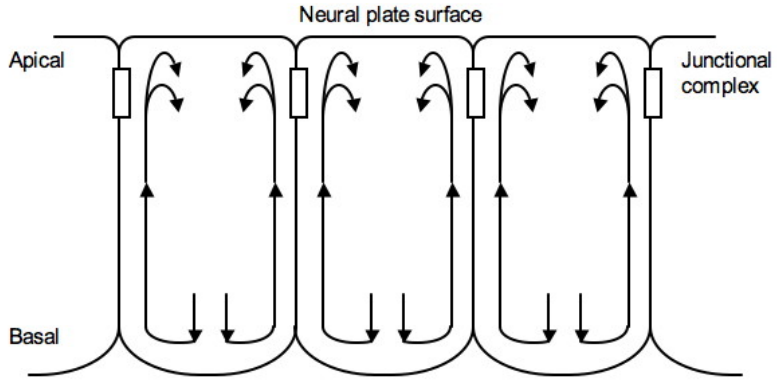


*Figure 1.8:* The cortical tractor model proposed by Jacobson. Intracellular flow pattern (modified from Jacobson et al. [1986]).

The authors showed how the model could be used to simulate placode formation, invagination, folding of the neural tube and cells rearrangement. The first two processes are controlled by differential flow rates between the cells; on the other hand, if the flow rates of all the cells are equal, they all remain in the plane of the sheet. Each epithelial cell is modeled as a quadrilateral filled with a viscous fluid. Both the passive elastic deformation of the cells and the active shear due to the differences in flow velocity between adjacent cells are included in the model. The authors simulated various aspects of amphibian neurulation and they found many of the observations pointed out by Jacobson and Gordon (Jacobson and Gordon [1976]), specifically the elongation of the neural plate and the rolling of the cells into the neural tube.

Very often from a macroscopical point of view it is more convenient to represent the epithelium as a plate or a shell, therefore as a continuum; Hardin and Cheng (Hardin and Cheng [1986]) proposed a model in which axisymmetric shell theory was used to simulate *Sea Urchin* gastrulation. They analyzed large deformations but the shell material was taken linear and isotropic. They obtained the gastrulation of the epithelium applying forces through the archenteron to opposite sides of a spherical shell representing the blastula (Fig. 1.9). Since the material properties in the entire structure are considered uniform, the authors observed a flattening of the blastula roof which is inconsistent with experimental results; furthermore, the model does not take into account the internal fluid in the blastula whose pressure may help the closure of the blastopore which is not obtained here.

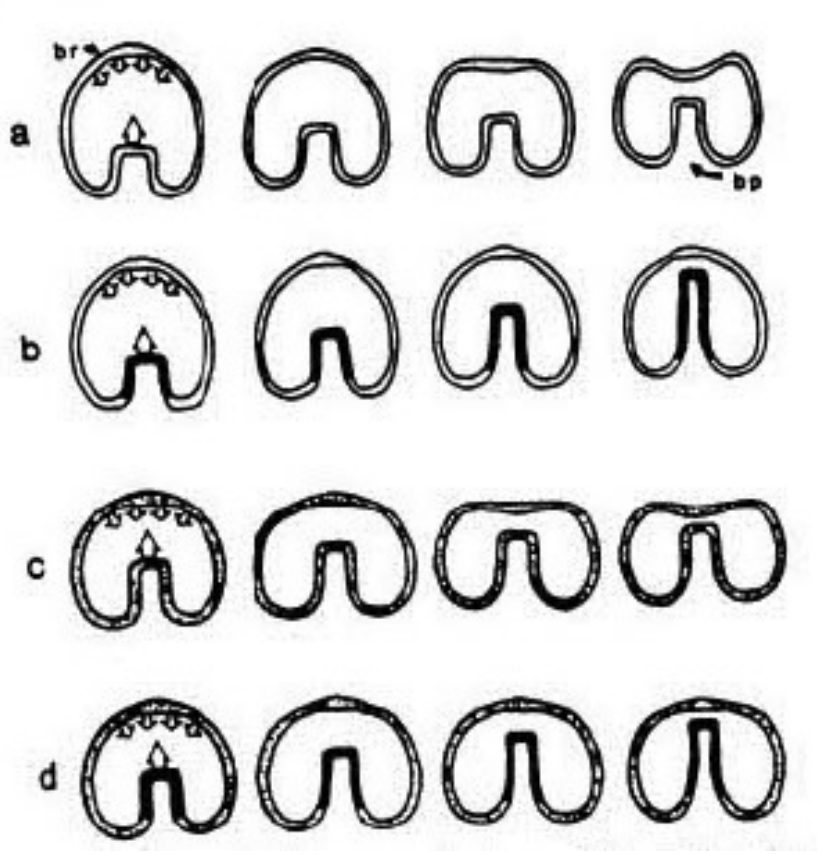


*Figure 1.9:* The shell model for gastrulation proposed by Hardin and Cheng (Hardin and Cheng [1986]).

A limited number of other shell models have been published. Mitthenthal (Mitthenthal [1987]) used a fluid-elastic thin-shell theory based on the assumption that

the shell resists bending and isotropic in-plane stresses elastically, but it cannot support static shear stresses. Gierer (Gierer [1977]) proposed a model based on adhesive potential, while Zinemanas and Nir (Zinemanas and Nir [1987]) modeled the blastula as a viscous drop of liquid surrounded by a fluid membrane and embedded in an ambient fluid.

Davidson (Davidson et al. [1995]) studied very accurately the forces that drive the *Sea Urchin* invagination; he proposed a series of finite elements simulations that test five hypothesized mechanisms and demonstrated that each one of them can generate invagination. The models he proposed are the following:

- an apical constriction model in which an imposed gradient of constriction along the cell axis drives the contraction of the apical surface and the expansion of the basal surface so that the cell volume remains constant;
- a cell contractor model obtained by appending contractile protrusions to a ring of cells at about $20\mu m$ from the center of the plate, a region that includes most of the cells that participate in primary invagination;
- an apical contractile ring model based on the wound healing mechanism observed in *Xenofus* embryos. A contractile ring of approximatevely $40\mu m$ in diameter and centered on the vegetal plate is installed at the apical surface of the cell layer; the contraction of this cable triggers both the invagination of the plate and the coordinated changes in shape occurring to the cells;
- an apico-basal contraction model in which contractile elements are embedded across the thickness of the cell layer within $20\mu m$ from the center of the vegetal plate. The forces generated by these contractile units are sufficient to buckle the epithelial sheet to the correct geometry;
- a gel swelling model where the vegetal plate apical lamina covers the region which normally invaginates and swells isotropically. The vegetal plate, which is constrained by the surrounding epithelium, buckles inward as the apical lamina expands.

The success of each mechanism depends on the passive stiffness of the cell layer relative to the stiffness of the two extracellular matrix layers. The cell tractoring, the apicobasal contraction and the gel swelling mechanisms work only when the extracellular matrix is very stiff with respect to the cell layer. On the other hand, the apical constriction and the apical contracting ring models work with a more deformable extracellular matrix.

In 1993 Clausi and Brodland (Brodland and Clausi [1993]) used apical constriction as primary driving force in their finite elements model for neurulation. They assumed that the microfilament force increases with contraction and they obtained very realistic results.

We also mention the work of Pouille (Pouille and Farge [2008]) in which an epithelium of cells is immersed in an incompressive viscous fluid. Some structural elements are used to describe the cell membranes, their actin cortex connected by apical and basal junctions and the apical adherens junctions connected to the contractile actin/myosin ring. These units are connected to each other to shape the cells of the epithelium enclosing the yolk. The cells and the yolk maintain their internal volumes of incompressible viscous fluid constant. The cell membranes are under the contractile elastic tension due to the actin/myosin cortex, while the contractibility of the adherens junctions is obtained putting additional springs crossing the disc. The authors pointed out how only the increase in the apical-cortical surface tension is the control parameter change required to simulate the main multicellular and cellular shape changes in *Drosophila* gastrulation. Therefore, most of the behaviours observed *in vivo* (apical junctions movements at the onset of gastrulation, cell elongation and consequent shortening during invagination) appear to be in this model a passive response to the genetically controlled apical constriction of the cells.

A common feature of all these models is the presence of structural units as actuators that reproduce elements of the cytoskleton such as microtubules and microfilaments. These elements lead the necessary shape changes, mainly apical constriction or axial elongation on certain region of the embryo. More recently, Muñoz (Muñoz et al. [2007]) proposed a model with no structural elements (Fig. 1.10). He simulated ventral furrow invagination using a deformation gradient decomposition method to model the permanent active deformations and the passive hyperelastic deformations as a local quantity applied to the continuum that schematises the epithelial layer. Each point of the epithelial cell layer is able to reproduce the two main deformations modes involved in invagination: apical constriction and apico-basal elongation.

A similar approach was used by Taber (Ramasubramanian and Taber [2006], Taber [2007]) that based his models on the Beloussov's hyper-restoration hypothesis (Beloussov [1998], Beloussov and Grabovsky [2007]) by which morphogenesis is regulated in part by feedback from mechanical stress. According to this hypothesis, active tissue responses to stress perturbations tend to restore, but go beyond the original target stress; the rate of growth or contraction depends on the difference between the current and the target stresses. He tested several finite elements models for stretching of epithelia, cylindrical bending of plates, invagination of cylindrical and spherical shells and early amphibian development. In each of these cases, an initial perturbation leads to a mechanical response which changes the global shape of the tissues.

Conte (Conte et al. [2008], Fig. 1.11) extended the work of Muñoz to develop the first three-dimensional model for ventral furrow invagination. The method used is the same as for the two-dimensional model previously described so that any point in the epithelial layer can contribute to the global deformation. In the model, there are no external constraints other than the presence of the vitelline membrane and the yolk. The former is modelled as a rigid sleeve-shaped shell constraining the

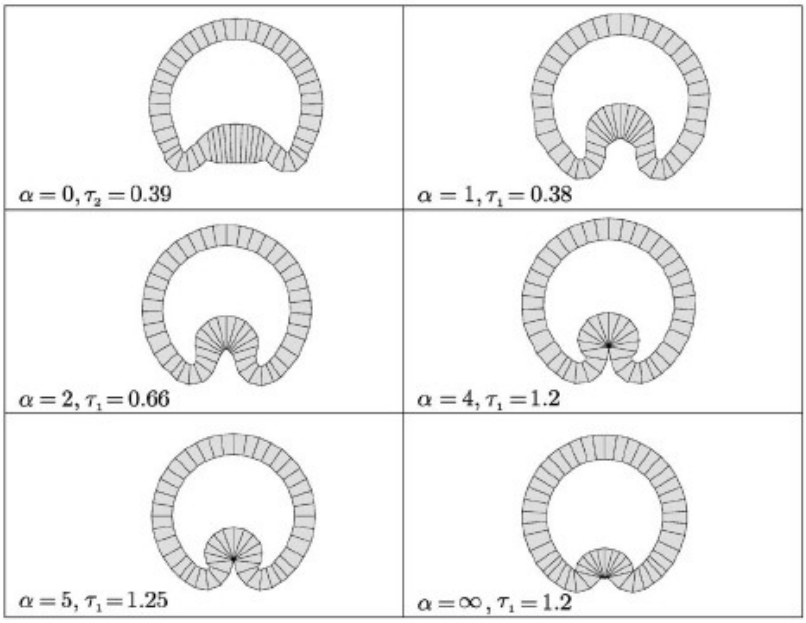


*Figure 1.10:* Deformed configurations for Muñoz's model; both apical constriction and apico-basal elongation were implemented depending on two parameters $\tau_1$ and $\tau_2$ respectively that define the temporal evolution of the active deformations. Images correspond to results obtained for different values of $\alpha = \frac{\tau_1}{\tau_2}$ (Muñoz et al. [2007]).

deformation and the latter imposes a constant volume constraint to the volume within the epithelium. The results are very interesting (Fig. 1.11). The authors also showed the influence of some parameters together with the presence or the absence of the vitelline membrane and the yolk (Fig. 1.12).

### 1.2.4 Cephalic furrow formation

The cephalic furrow (CF), first of the seven additional gastrulation-like events listed in Sec. 1.2, forms at the same time as the ventral furrow and it is triggered by almost the same mechanical forces described for ventral furrow (Fig. 1.13). It first becomes visible as a latero-ventral slit at about 65% egg length. Later, it extends transversely from the dorsal midline, at about 60% egg length, to the ventral midline at about 75% egg length. Unlike the ventral furrow invagination, the cephalic furrow is only transient. In fact at the completion of germ band extension, all cells involved slowly unfold back onto the surface of the embryo to contribute to the ectoderm (Campos-Ortega and Hartenstein [1985], Costa et al. [1993], Foe et al. [1993]).

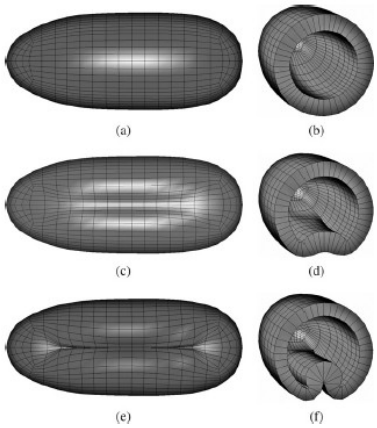


*Figure 1.11:* The first 3D model of ventral furrow invagination provided by Conte (Conte et al. [2008]). Three deformed configurations show respectively a ventral view (a, c, e) and a cross sectional view (b, d, f).

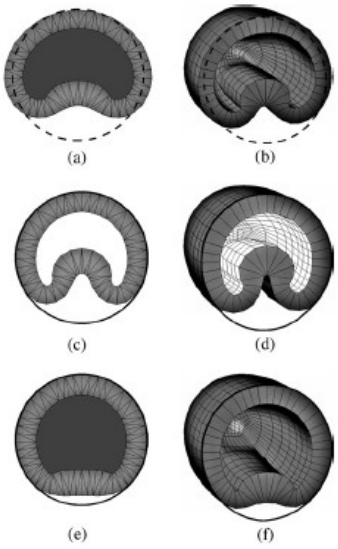


*Figure 1.12:* Simulations with the modified boundary conditions and unusual active deformations (Conte et al. [2008]). (a, b) Simulations where no vitelline membrane is considered, 2D section (a) and 3D view (b). (c, d) Results when yolk pressure was not implemented, 2D section (c) and 3D view (d). (e, f) Simulations where apico-basal elongation was not considered, 2D section (e) and 3D view (f).

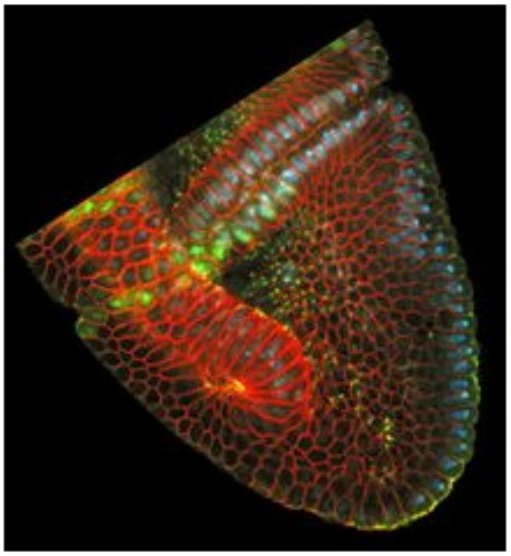

*Figure 1.13:* The formation of the cephalic furrow at the anterior end of a developing *Drosophila Melanogaster* embryo visualized with the help of several fluorescent stains (www.invitrogen.com).

Even though the cephalic furrow is a prominent morphological event of the early gastrula, its developmental role remains enigmatic (Vincent et al. [1997]). It has not been possible so far to isolate specific mutations affecting only this event; furthermore,, the cellular and genetic mechanisms that control its formation are still unknown. Eventually, the absence of a cephalic furrow in embryos derives from mothers mutant for *bicoid* (Frohnhofer and Nusslein-Volhard [1986]) and the reproducible shifts in its position and its lateral extent indicates that the cell shape is directly affected by positional information (Zusman and Wieshaus [1985]). Nevertheless, these particular information do not provide interesting tips on how positional information are translated into specific changes in cellular morphology.

The cephalic furrow forms at an interesting region of the embryo, at the juxtaposition of the patterning systems that define the head and the trunk segments; these two systems involve different groups of zygotically active genes, specifically cephalic furrow coincides with the expression of the pair-rule gene *eve* and it has been observed (Costa et al. [1993]) that in *eve* mutant embryos the cephalic furrow is eliminated or abnormal, which suggests a strong control of *eve* on the morphogenetic event. In addition, the activity of the head gap-like segmentation gene *buttonhead* may also influence the formation of the furrow (Vincent et al. [1997]).

The lack of accurate information has definitely restrained mechanical modeling of the cephalic furrow formation even if it represents one of the most interesting

morphogenetic event in *Drosophila* embryo. Therefore, the present work is original in this sense since it provides an innovative finite elements model able to simulate the formation of the furrow.

### 1.2.5 Convergence-extension movements

During morphogenesis, epithelial tissues undergo changes in shape very rapidly and often cell division does not play a role in this process. More particularly, tissues seem to behave like membranes that stretch and bend; usually these mechanical movements are accompanied by a change in shape of individual cells or by a rearrangement of the cells so that they change their neighbours.

#### 1.2.5.1 Occurrence of the convergence-extension

The convergence-extension is a key process leading to the formation of an elongated axis in many animal phyla (Kimmel et al. [1994], Schoenwolf and Alvarez [1989]). Also it can take place in epithelial tubes as in the case of the *Sea Urchin*, where once the gut has formed, the cells around its circumference decrease, while the number along its length increases (Davies [2005]). For sure, one of the most studied examples is the elongation of the germ band in *Drosophila Melanogaster* (Irvine and Wieschaus [1994]), which we are going to describe and analyze more in details in the next section.

Convergence and extension are normally used to indicate the narrowing and the lengthening of tissues respectively (also refer to Keller et al. [1991b] and Keller et al. [1991a]). Convergence can be coupled directly to extension with conservation of tissue volume, therefore a decrease in width occurs with a proportional increase in length. In other cases, convergence may engender thickening as well as lengthening. Thus the term "convergence-extension" is often used for convenience, but one has to remember and consider the complex relationship between convergence, extension and thickening. Actually, convergence-extension movements can be included in a larger and more general class of "mass movements", involving change in tissue proportions with approximate conservation in volume (Keller et al. [2000]). In addition, these type of movements may be a passive response to forces generated elsewhere in the embryo or they may be active and force-producing processes.

These "mass movements" represent a very interesting challenge and also a great opportunity to better understand the functions of the cells with respect to embryogenesis. So far, little is known about the cellular, molecular and biological mechanisms of these movements so that it is not easy at all to evaluate their role and importance in shaping the embryo's body. Furthermore, cell interactions within populations are difficult to detect since it is difficult to visualize and interpret cell motility through the embryo. In fact, the functions of the cells are usually studied on individual cells in culture at low density, while most of mass movements take place at high densities

of cells that are interacting with one another or with the extracellular matrix. Finally it has also to be noticed that in the case of a single cell, the generated forces have local effects on its movement in culture; for cells populations instead, these forces have both local effects and effects that are integrated through the population.

#### 1.2.5.2 Cell rearrangement or intercalation

In most of the cases, convergence-extension movements are triggered by the rearrangement of the cells; practically the cells intercalate between one another to produce a significant change in shape of the tissue and then to form a stiff array, which can distort and deform the surrounding passive tissues (Fig. 1.14).

The first who supposed this type of process was Waddington in 1940 (Waddington [1940]); by studies on amphibians, he observed that the convergence-extension occurred in absence of cell growth and the appropriate changes in shape, therefore he suggested that these movements must take place by cells rearrangement.

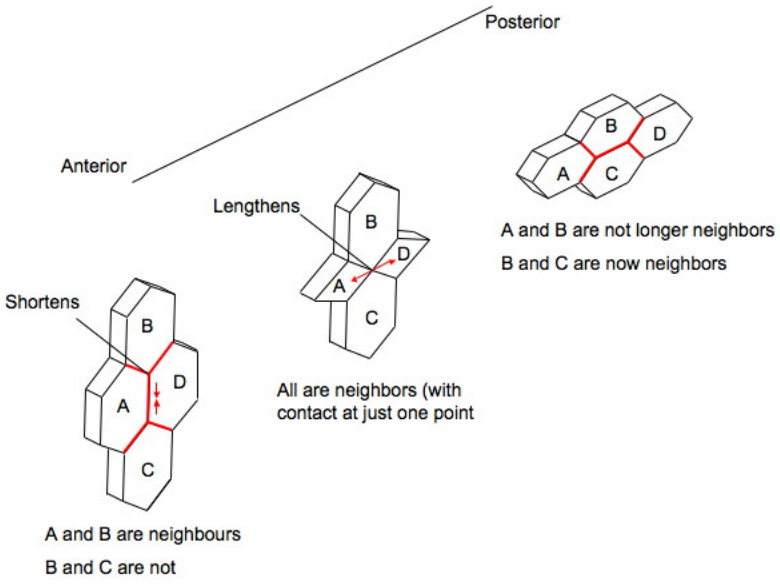


*Figure 1.14:* Cells rearrangement process during convergent-extension movement.

The regions involved in these "mass movements" are composed by a single layer of superficial epithelial cells and several layers of deep mesenchymal cells. Morphological studies have shown that tissues converge and extend by two main types of cells rearrangement. During the first half of gastrulation, mesenchymal cells and posterior neural tissues undergo radial intercalation (Keller [1980]); they intercalate

along the radius of the embryo, normal to its surface, to generate a thinner array that is also longer in the prospective anterior-posterior axis. Usually superficial epithelial cells do not participate to this phase of intercalation, but simply spread and divide to accommodate the larger area of the spreading deep cells. Just after radial intercalation, convergence-extension occurs by a mediolateral intercalation in which cells move between one another to form a narrower, longer and thicker array (Keller and Tibbetts [1989]). This time the superficial cells accommodate the narrowing and the extension of the deeper cells intercalating, dividing and spreading themselves too. Usually, mediolateral intercalation occurs at and beyond the blastoporal lip in the post-involution region, while radial intercalation is typical of the pre-involution region.

### 1.2.6 Cells rearrangement models

Modeling cells rearrangement within an epithelium is complicated by the need to follow individual cells. Weliky and Oster (Weliky and Oster [1990]) proposed a simulation for epithelial cells rearrangement taking into account the effects of changing intra and intercellular forces. In their model, each cell is represented by a two-dimensional polygon with a variable number of sides and nodes that can slide, appear and disappear (Fig. 1.15). The forces applied on the node determine its motion and, to maintain the compatibility, the geometry is updated. The plasma membrane of each cell contains actin/myosin filaments and encloses a filament-rich gel. The forces generated on the nodes may be caused by:

- positive osmotic pressure that expands the gel;
- negative elastic pressure due to intracellular filaments opposing gel swelling;
- tension in the sides due to microfilament bundle contraction;
- external loads.

Each node moves proportionally to the force acting on it and in the direction of the resultant force; therefore internal pressure triggers protrusions while tensile wall stress drives cellular contraction. The model was used to simulate epiboly (when an epithelium expands to enclose the interior of the early embryo) and it was observed that the number of cells at the margin decreases continually during the process even if its circumference increases.

The model was later modified by Weliky (Weliky et al. [1991]) with some new features to analyze tissue extension, cell rearrangement and the interactions of cells with boundaries. The conclusion was that several rules of cell behaviour operate simultaneously during frog neurulation.

Beloussov and Lakirev (Beloussov and Lakirev [1991]) used a very similar approach modeling the epithelium as a shell composed by movable elements. The

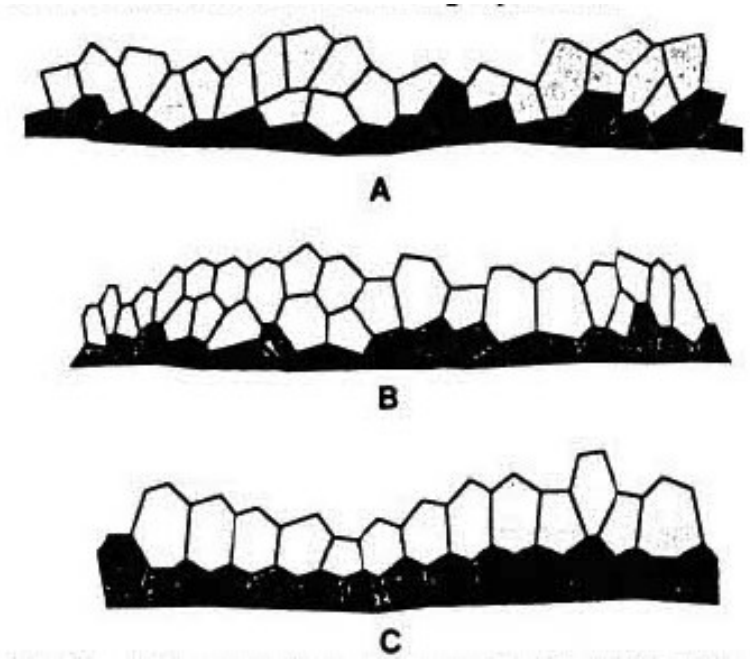


*Figure 1.15:* Cells rearrangement in the epiboly model (Weliky and Oster [1990]).

radial displacement of each element depends on the resultant force acting on that element. The authors obtained various morphogenetic shapes through a finite elements formulation.

Another interesting work was provided by Jacobson (Jacobson et al. [1986], Fig. 1.16) whose cortical contractor model has already been described in the previous section. According to this model, the key of cells rearrangement lies below the apical surface. The process is initiated by a basal protrusion that moves across a junction to a separated cell. Subsequently the extent of the protrusion is increased by the flow and it moves toward the apical surface together with the adhesion molecule. Once the protrusion has reached the apex, the cell can adhere to the new neighbour and rearrangement takes place without breaking the apical seal.

### 1.2.7 Germ band extension

As mentioned in Sec. 1.2.5, one of the most interesting examples of convergence-extension is given by the elongation of the germ band in *Drosophila* embryo. The germ band corresponds to the part of the embryo that will form the trunk and that shorten and lengthen to curl around the egg and lately bend back on itself (Davies [2005]). This movement occurs very rapidly during its initial phase and is quite slow during the following stages. It starts at stage eight and by the end

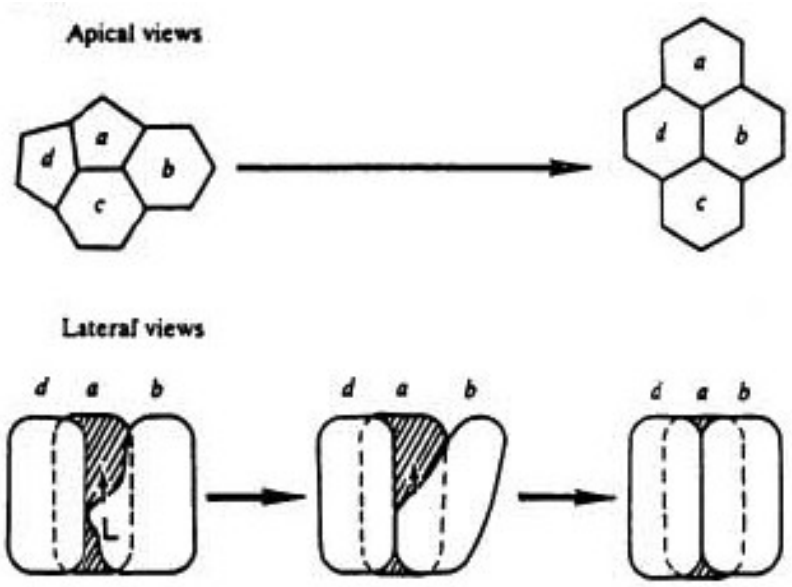


*Figure 1.16:* Cellular rearrangement mechanism (Jacobson et al. [1986]).

of stage ten the elongation has progressed to bring the posterior tip of the germ band to about 75% egg length. Meanwhile the cells converge from the dorsal to the ventral region of the embryo and intercalate between one another so that the tissues elongate along the midline. During the process, the cells never acquire free edges, therefore the integrity of the epithelium is retained. Particularly before the convergence-extension movement, the cells form an hexagonal array, while after the rearrangement the centers of the cells form ordered rows along the anterior-posterior axis. This means that one third of the cell-cell boundaries are at 90° with respect to the anterior-posterior axis, one third at 30° and the remaining at -30°.

The intercalation of the cells is highly directional since cells intercalate almost exclusively between dorsal and ventral neighbours and only rarely between anterior and posterior neighbours (Irvine and Wieschaus [1994]). Although evenly distributed, intercalation does not follow a precise pattern given that blastoderm neighbours may be separated by zero, one, two or three cells. Furthermore, cells only intercalate between their nearest neighbours and do not migrate widely; this can be observed following columns that extend from dorsal to ventral. These columns become shorter and wider as the germ band extends and when they collapse into irregular shape, the cells of a single column always remain together.

The cells first move slightly dorsally, then more rapidly ventrally and posteriorly and finally simoultaneously posteriorly and ventrally. The positioning of the cells may affect the trajectories; in fact more dorsal cells move further ventrally than

ventral cells do and more posterior cells move further posteriorly than anterior cells do. In addition cells that are near the cephalic furrow first move anteriorly pushing the furrow forward and then they start moving posteriorly (E. Wieschaus and Kluding [1984]). Intercalation is symmetrical since dorsal cells come between their ventral neighbours and ventral cells come between their dorsal neighbours. There is an increase in the number of cells along the anterior-posterior axis, which is more rapid ventrally than dorsally, and a decrease along the dorsal-ventral axis.

Even if it has not been possible so far to individuate mutations that are specifically defective of germ band extension, mutations in many of the genes involved in patterning along the anterior-posterior axis have shown reduction of the elongation. In particular the process is reduced by mutations in the maternal coordinate genes and in the zygotic gap and pair-rule segmentation genes; specifically *eve* seems to mostly reduce the extension of the germ band (Irvine and Wieschaus [1994]).

## 1.3 Conclusions

Embryogenesis is a very complex process where mechanics and biology are merged together, with strong interconnections at different phases of the development. If for a long time biologists have observed the influence of genetics on the mechanical forces within the embryo, as largely described in the previous paragraphs, only recently they have supposed the inverse phenomenon: the control exerted by mechanics on the expression of specific genes. It is still not so clear and understood how a mechanical force can be transformed into a chemical signal, but it is evident that a mechanotransduction pathway must be present all long the embryogenesis. Also, embryonic cells, as other types of cells in nature (endothelial cells, muscle cells...), must be mechanosensible and therefore able to deform and to adapt themselves when external loads are applied on them.

Each cell is characterized by the presence of internal elementary forces, the primary or active forces, that can occur during embryo development and would lead to a pure deformation if cells were not part of a system and in contact with one each other. Instead, boundary conditions at the interfaces must be respected, therefore, to avoid the incompatibility (i.e. superposition of volumes) potentially caused by the elementary forces, tissues are forced to deform again (secondary or passive forces) in order to maintain the continuity of the mesoderm. For the three morphogenetic movements we have decided to focus on (ventral furrow invagination, cephalic furrow formation and germ band extension), several elementary forces have been individuated by biologists, but so far it is still difficult to determine which ones among them can be considered a real primary force and which ones a simple passive response of the neighbour cells to the active ones. Mechanical modeling, and numerical one in particular, may help in detecting this peculiar aspect, as we are going to show later on, other than provide a useful tool in investigating more accurately the global

response of the embryo to mechanical forces.

That being said, treating with a biological system always represents a real challenge. Many are the parameters that may affect the global behaviour of the structure and most of the time they are very difficult to detect. Additionally, for our specific case, the embryo is composed by several elements not easy to model, therefore many approximations are made so that the final representation is often a macro-scale representation.

The different works we have found in literature and briefly described in this chapter prove the progresses that have been made in computer simulation in the last decades. The methods and approaches used are all very interesting and supply consistent results compared to the biological observations. Nevertheless we think that our model, which have been first presented at the Second International Conference on Mechanics of Biomaterials and Tissues (Hawaii, 9-13 December 2007), shows some innovative aspects with respect to the previous ones (Allena et al. [2008]).

Most of the former works have been conceived in a two dimensional space, while our description of the embryo is done in a three dimensional space, so that we have a more realistic representation of the biological reality. In despite of this it has to be noticed that the geometry of our model has not been obtained from MRI, but an ellipsoid has been used to represent the embryo, thus the different curvature between the anterior and the posterior pole is not considered here. We are aware that this characteristic may influence the final results, especially for the simulation of those movements that take place along the anterior-posterior axis (i.e. ventral furrow invagination and germ band extension). Also only mesoderm has been modelled assuming that the mechanical characteristics of the three embryonic layers, which form throughout the gastrulation phases, may not be so different so that we can consider that the mesoderm constitutes the most part of the blastoderm.

With a single model and without introducing any structural elements, we are able to individually simulate three morphogenetic movements: ventral furrow invagination (VFI), cephalic furrow (CF) formation (which, to the best of our knowledge, has never been simulated before) and germ band extension (GBE). This is possible by the parametrical description of the embryo which constitutes the outstanding advantage of the present work with respect to previous ones where the model allowed to simulate only one movement and most of the time ventral furrow invagination. Actually, we have precise active deformation gradients, according to the morphogenetic movement analyzed, that are analytically obtained and can easily be changed and elaborated. Furthermore,, the active forces we introduce are independent of the mesh applied on the geometry and thus of the discretization.

Finally we will present here not only the simulation of the three movements individually, but also and more importantly the concurrent simulation of two or three of them. This represents a very innovative feature because, to the best of our knowledge, it is the first time that the three movements are coupled together. The concurrent simulation provides a more complete view of a fragment of *Drosophila*

embryogenesis, the gastrulation, which is one of the most complex and interesting phase of the developmental process.

The main goal of the present work is therefore to confirm, through the finite elements model, the hypothesis made by the biologists. Most importantly we prove how mechanical modeling can be helpful not only in clarifying the whole biological problem but also and especially in pointing out some of its facets that have been so far ignored or rarely developed.

# Chapter 2

# The kinematic model

In this section of the work, we present the general kinematics of the active and passive deformations that will be described more in detail for each morphogenetic movement in the next chapter. As similarly as previous studies, a gradient decomposition method is applied (Sec. 2.1), so that both the active and the passive deformations undergone by the embryonic tissues are taken into account and, coupled together, provide the final deformation. Additionally, we show some interesting interpretations of the approach and we point out novel aspects of the problem that lead to further discussions. Specifically, in Sec. 2.4 we compare the gradient decomposition to an equivalent thermal deformation, while in Sec. 2.5 we analyze the potential effects of the local active forces on both the active and passive domains and in particular at the internal and external cellular interfaces.

The Virtual Power Principle is then used to write the equilibrium of the system (Sec. 2.2) for which, other than the internal forces of the structure, we must take into account the boundary conditions. We implement the contact between the epithelial layer and the external semi-rigid membrane (Sec. 2.7.1) and the yolk pressure exerted on the internal surface of the embryo (Sec. 2.7.2). The presence of these two components, even if not geometrically represented here, is necessary to obtain realistic final configurations. The model has been validated by testing it on simple geometries in two or three dimensions (Sec. 2.6).

In Sec. 2.3, we focus on the constitutive law used to describe the embryonic tissues. A Saint-Venant model is proposed for the present work which may not be the best representation compared to the Neo-Hookean material used by previous authors. A comparison between the two models is made; the results obtained for both cases show similar results (Chapter 3), so that our choice can be considered appropriate even if presenting some limitations.

## 2.1 Gradient decomposition method

The model we use for our simulations does not present any structural elements as other previous works (Chapter 1), but we impose the kinematics of the main observed active deformations in *Drosophila* embryo according to the morphogenetic movement considered. Onto this active part, a passive deformation takes place, which determines the integrity and the static equilibrium of the embryo. The active deformation can be identified with the biological impulse of each cell to change its shape when stimulated by a higher concentration of actin/myosin filaments. If the cells were not part of a system, therefore in contact with one another and constrained by the presence of the yolk and the vitelline membrane, we would obtain a free deformation, as if they were isolated, which means that only the active deformation would be observed. On the other hand, the boundary conditions, imposed by the structure of the embryo, lead to an auxiliary deformation, the passive one, that provides the final configuration observed. The method presented here has already been tested with success for the analysis of ventral furrow invagination in *Drosophila* embryo (Ramasubramanian and Taber [2006], Muñoz et al. [2007], Conte et al. [2008]). In our model, we do not take into account the causes for the implemented active deformations, but, contrarily, we consider them as an internal contribution, specifically chemo-mechanically transduced, that can produce different combinations of the deformations observed through the embryo, as proposed by Muñoz (Muñoz et al. [2007]). Furthermore only the contact between the embryonic tissues and the vitelline membrane and the yolk pressure have been introduced as boundary conditions. Later on we will discuss more in detail these two aspects that play an important role and may influence the global behaviour of the embryo; particularly, it has been demonstrated that the absence of one of these components provides results that do not match with experimental observations (Conte et al. [2008]).

We assume here that each point of the region where the mechanical transformations are introduced is able to produce the main modes of deformation. The initial configuration before any force applied is a stress-free configuration, even if at this point some internal stress may develop. From this initial configuration, the active and the passive deformations are obtained.

As previously mentioned and later on more specified, only the mesoderm has been represented and it has been considered as a regular assembling of cells that present the same geometry. At the reference configuration, in a curvilinear system of coordinates, by the position of each point $\mathbf{p}_0(\xi^1, \xi^2)$ on the middle surface of the mesoderm, we obtain all the points $\mathbf{p}(\xi^1, \xi^2, \xi^3)$ within the thickness of the tissue as follows

$$\mathbf{p} = \mathbf{p}_0 + \zeta\, \mathbf{n}_0 \tag{2.1}$$

where $\zeta$ is the distance between $\mathbf{p}$ and $\mathbf{p}_0$ calculated along the normal $\mathbf{n}_0$ to the

middle surface passing by $\mathbf{p}$. If we call $\mathbf{x}$ the current position of a generic point and $\bar{\mathbf{x}}$ its intermediate position once the active deformations applied (Fig. 2.1), we can write, as similarly as for the approach presented in Sec. B.2, that

$$\mathbf{F} = \mathbf{D}_{\mathbf{p}}\mathbf{x} = \mathbf{D}_{\bar{\mathbf{x}}}\mathbf{x}\,\mathbf{D}_{\mathbf{p}}\bar{\mathbf{x}} = \mathbf{F}_m\mathbf{F}_a \tag{2.2}$$

where

$$(\mathbf{D}_{\mathbf{b}}\mathbf{a})_{ij} = \frac{\partial a_i}{\partial b_j} \tag{2.3}$$

and

- $\mathbf{F}$ is the total deformation gradient;
- $\mathbf{F}_a$ is the active deformation gradient;
- $\mathbf{F}_m$ is the passive deformation gradient, which is a necessary response of the cells to assure the continuity of the mesoderm.

When analyzing the relation linking together the three deformations, different situations must be contemplated; although, it has to be noticed that the Second Piola-Kirchhoff tensor $\mathbf{S}_m$, with respect to the intermediate deformation, will still depend on $\mathbf{E}_m$, the Green-Lagrange strain tensor at the relative configuration (see Sec. 2.3), whatever the deformation will be.

**Free cell**

First of all, let us consider an isolated cell, without any boundary condition imposed, which implies the absence of constraints; thus $\mathbf{S}_m(\mathbf{E}_m) = 0$. We deduce, by the definition of $\mathbf{E}_m$ (see Appendix A), that $\mathbf{F}_m = \mathbf{I}$, $\mathbf{I}$ the identity tensor, therefore $\mathbf{F} = \mathbf{F}_a$: a free deformation, corresponding to the active one itself, is observed in this case.

**Constrained cell**

When the cell is totally constrained (Fig. 2.2), no deformation can occur, which provides $\mathbf{F} = \mathbf{I}$ and thus $\mathbf{F}_m = \mathbf{F}_a^{-1}$. This means that, while the active force tempts to deform the cell membrane, the passive deformation, because of the boundary conditions, limits such modification and it is therefore complementary to the former one. The internal stresses can then be measured on the fixed walls that constrain the cell.

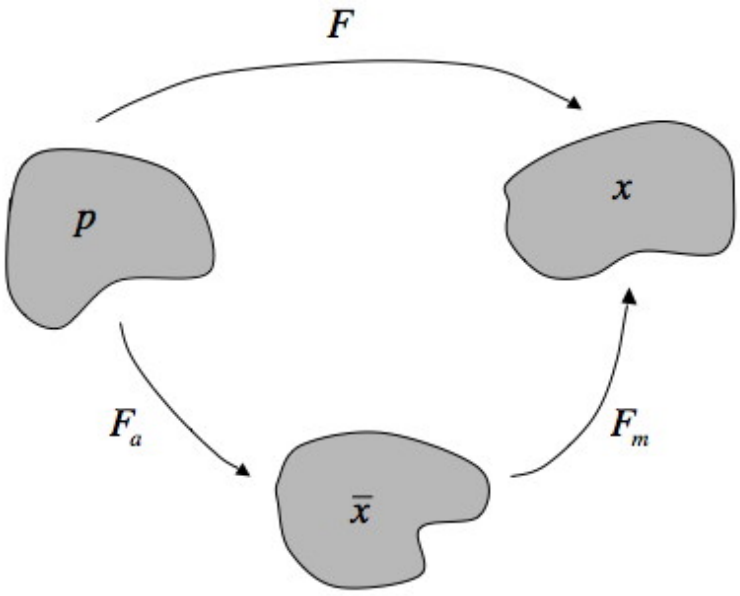


*Figure 2.1:* Initial, intermediate and final configuration for a cell of the embryo.

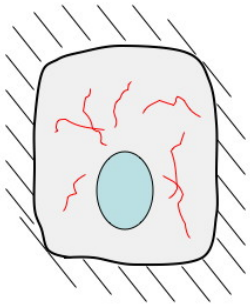

*Figure 2.2:* The case of a cell constrained along its boundaries.

### Neighbour cells

Finally, we consider the case of a cell whose displacements are limited by the presence along its boundaries of deformable structures (Fig. 2.3), as similarly as

for the embryo, where the cells are in contact with one another, with the yolk and the vitelline membrane and must maintain the integrity of the mesoderm. In this specific case, $\mathbf{F}_m$ is the actual response to the active deformation $\mathbf{F}_a$, so that the two deformations are composed together to provide the suitable final configuration.

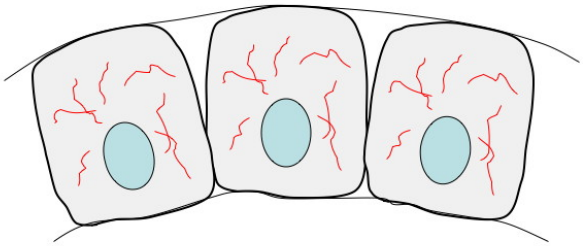

*Figure 2.3:* The case, as similarly as for the embryo, where the cells are in contact with one another and with some internal or external components.

$\mathbf{F}_a$ gives the elementary cell deformations according to the morphogenetic movement analyzed and it can be written as

$$\mathbf{F}_a = \frac{\partial \bar{\mathbf{x}}}{\partial \mathbf{p}} \tag{2.4}$$

It has to be said here that the active deformation involves the cell membrane and it has therefore to be considered as a micro-scale deformation; for the present study we have decided to model it as a uniform deformation of the cell. Also, not all the cells of the mesoderm are active at same time and at same regions; thus, according to the morphogenetic movement, the elementary deformations will be applied on restricted domains of the embryo, as it will be shown in Chapter 3, so that we will have $\mathbf{F}_a = \mathbf{I}$ elsewhere.

By the tensorial product, we can actually obtain an equivalent expression of Eq.[2.4], which is

$$\mathbf{F}_a = \sum_{m=1,3} \frac{\partial \bar{\mathbf{x}}}{\partial p_m} \otimes \mathbf{i}_m \tag{2.5}$$

Because of the curved geometry of the embryo, a special curvilinear coordinates system will be employed in Chapter 3, therefore we develop here the necessary abstract tools.

By the usual convention of the repeated dummy subscript, we know that

$$\frac{\partial \bar{\mathbf{x}}}{\partial p_m} = \frac{\partial \bar{\mathbf{x}}}{\partial \xi^n} \frac{\partial \xi^n}{\partial p_m} \tag{2.6}$$

thus we find the following formulation for $\mathbf{F}_a$

$$\mathbf{F}_a = \sum_{n=1,3} \frac{\partial \bar{\mathbf{x}}}{\partial \xi^n} \otimes \boldsymbol{\nabla}_{\mathbf{p}} \xi^n \tag{2.7}$$

For instance, $\frac{\partial \bar{\mathbf{x}}}{\partial \xi^1}$ is the tangent vector at the point $\left(\xi_0^1, \xi_0^2, \xi_0^3\right)$ to the curve $(\xi_1^1, \xi_0^2, \xi_0^3)$ and, together with $\frac{\partial \bar{\mathbf{x}}}{\partial \xi^2}$ and $\frac{\partial \bar{\mathbf{x}}}{\partial \xi^3}$, which are obtained by circular permutation, constitutes the *covariant basis* in $\bar{\mathbf{x}}$. On the other hand, the component $\nabla_{\mathbf{p}} \xi^1$ is the gradient to the surface $\xi^1 = \xi_0^1$ and forms, with $\nabla_{\mathbf{p}} \xi^2$ and $\nabla_{\mathbf{p}} \xi^2$, the *contravariant basis* in $\mathbf{p}$ (Smith [1993]). Afterwards we will indicate the former as $\mathbf{g}_{\bar{\mathbf{x}},n}$ and the latter as $\mathbf{g}_{\mathbf{p}}^n$. Then we can write

$$\mathbf{F}_a = \mathbf{g}_{\bar{\mathbf{x}},n} \otimes \mathbf{g}_{\mathbf{p}}^n \tag{2.8}$$

and if no active initial deformation is introduced into the system (Fig. 2.4), $\mathbf{p} = \bar{\mathbf{x}}$ and we have

$$\mathbf{g}_{\mathbf{p},n} \otimes \mathbf{g}_{\mathbf{p}}^n = \mathbf{I} \tag{2.9}$$

Without inverting the active configuration from the initial one, we would like to find the vectors $\mathbf{g}_{\mathbf{p}}^n$. The *covariant* and *contravariant basis* are related by the equation

$$(\mathbf{g}_{\mathbf{p}}^m, \mathbf{g}_{\mathbf{p},n}) = \delta_{mn} \tag{2.10}$$

and, in an orthogonal basis, for instance for $\xi_3$, we know that

$$\frac{\partial \xi^3}{\partial \xi^1} = \frac{\partial \xi^3}{\partial p_n} \frac{\partial p_n}{\partial \xi^1} = (\nabla_{\mathbf{p}} \xi^3)_n (\mathbf{g}_{\mathbf{p},1})_n = \left( \nabla_{\mathbf{p}} \xi^3, \frac{\partial \mathbf{p}}{\partial \xi_1} \right) = (\mathbf{g}_{\mathbf{p}}^3, \mathbf{g}_{\mathbf{p},1}) \tag{2.11}$$

so that $\mathbf{g}_{\mathbf{p}}^3$ is perpendicular to $\mathbf{g}_{\mathbf{p},1}$ and, similarly, to $\mathbf{g}_{\mathbf{p},2}$. Consequently, it can be expressed as

$$\mathbf{g}_{\mathbf{p}}^3 = \alpha (\mathbf{g}_{\mathbf{p},1} \wedge \mathbf{g}_{\mathbf{p},2}) \tag{2.12}$$

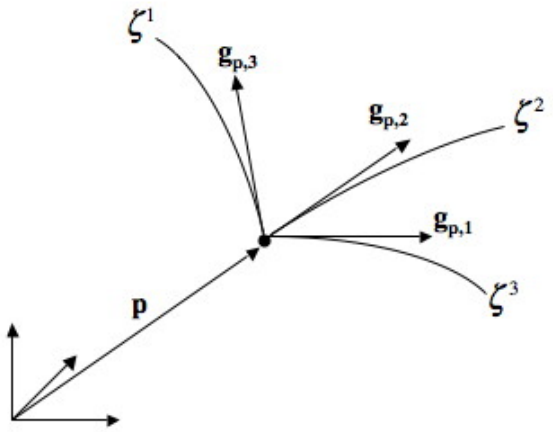


*Figure 2.4: Covariant basis* when no deformation is applied ($\mathbf{p} = \bar{\mathbf{x}}$).

When $m = n$ we have

$$(\mathbf{g}^m_{\mathbf{p}}, \mathbf{g}_{\mathbf{p},n}) = 1 \tag{2.13}$$

and in the specific case analyzed

$$(\mathbf{g}^3_{\mathbf{p}}, \mathbf{g}_{\mathbf{p},3}) = 1 \tag{2.14}$$

then Eq.[2.12] can be rewritten as follows

$$\alpha(\mathbf{g}_{\mathbf{p},1} \wedge \mathbf{g}_{\mathbf{p},2}, \mathbf{g}^3_{\mathbf{p}}) = 1 \tag{2.15}$$

If we indicate with $g$ the expression in the parenthesis, we can deduce that $\alpha = 1/g$. Therefore it is possible to deduce the expressions of all the vectors $\mathbf{g}^n_{\mathbf{p}}$

$$\begin{aligned} \mathbf{g}^1_{\mathbf{p}} &= \frac{\mathbf{g}_{\mathbf{p},3} \wedge \mathbf{g}_{\mathbf{p},2}}{g} \\ \mathbf{g}^2_{\mathbf{p}} &= \frac{\mathbf{g}_{\mathbf{p},1} \wedge \mathbf{g}_{\mathbf{p},3}}{g} \\ \mathbf{g}^3_{\mathbf{p}} &= \frac{\mathbf{g}_{\mathbf{p},1} \wedge \mathbf{g}_{\mathbf{p},2}}{g} \end{aligned} \tag{2.16}$$

Typically, $\mathbf{F}_a$ will be calculated in the special curvilinear coordinates system adapted to the geometry of the embryo, where active elementary deformations such as apical constriction, apico-basal elongation and convergent-extension will be introduced. In particular we will obtain different expressions of $\mathbf{F}_a$, proper to each morphogenetic movement considered, since the intermediate position $\bar{\mathbf{x}}$ changes according to the deformations applied to the continuum. We will analyze more in detail in the following chapter what happens for the specific cases of the ventral furrow invagination (Sec. 3.2), the cephalic furrow formation (Sec. 3.2) and the germ band extension (Sec. 3.3).

## 2.2 The Principle of the Virtual Power

The Principle of the Virtual Power that we use here is a variational principle with only one field of dependent variables, specifically the displacement vector $\mathbf{u}$. These type of principles are fundamental and essential in establishing finite elements formulations (Holzapfel [2000]). Mechanical systems, all the more so biological systems, are often constituted by heterogeneous materials, which implies the presence of a discontinuity of the mechanical properties. Particularly, it is necessary to impose some boundary conditions such as the continuity of the displacements and the reciprocity of the stress vectors; the Principle of the Virtual Power allows the user to automatically take into account the latter aspects.

If $\Omega_{m_x}$ indicates the mesoderm domain at the actual configuration, with $\partial\Omega_{m_{i_x}}$ and $\partial\Omega_{m_{e_x}}$ the internal and the external boundaries respectively (further on the subscript $x$ will indicate the deformed configuration), the equilibrium of the system can be written as

$$\mathbf{Div}_{\mathbf{x}}\boldsymbol{\sigma} + \rho_x \mathbf{f}_v = 0 \quad \text{in}\, \Omega_{m_x} \tag{2.17}$$

with $\boldsymbol{\sigma}$ the Cauchy stress tensor and $\mathbf{f}_v$ the body forces. When considering large deformations, we do not exactly know the deformed configuration and consequently where the boundary conditions are applied, therefore it is useful to rewrite the equilibrium with respect to the initial configuration. It has to be known that, by the principle of mass conservation, the mass density should satisfy the following relation

$$\rho_x = \frac{\rho}{J} \tag{2.18}$$

where $J = Det\,\mathbf{F}$ and $\rho$ is the mass density at the initial configuration.
Then, classically, the first term of Eq.[2.17] can be rewritten as

$$\mathbf{Div}_{\mathbf{x}}\boldsymbol{\sigma} = \frac{1}{J}\mathbf{Div}_{\mathbf{p}}(J\boldsymbol{\sigma}\mathbf{F}^{-T}) = \frac{1}{J}\mathbf{Div}_{\mathbf{p}}\boldsymbol{\pi} \tag{2.19}$$

with $\boldsymbol{\pi}$ the First Piola-Kirchhoff tensor. Thus Eq.[2.17] becomes

$$\mathbf{Div_p}\boldsymbol{\pi} + \rho\,\mathbf{f}_v = 0 \tag{2.20}$$

Here we neglect the volume forces such as gravity, therefore we obtain

$$\mathbf{Div_p}\boldsymbol{\pi} = 0 \tag{2.21}$$

For two vectors $(\mathbf{a}, \mathbf{b})$, we define the dot product as

$$(\mathbf{a}, \mathbf{b}) = \sum_{i=1,2} a_i b_i \tag{2.22}$$

In order to get the Principle of the Virtual Power, we multiply the equilibrium equation (Eq.[2.21]) for a virtual displacements field $\mathbf{w}$ so that, by the property of the divergence, we have

$$(\mathbf{Div_p}\boldsymbol{\pi}, \mathbf{w}) = div_{\mathbf{p}}\left(\boldsymbol{\pi}^T(\mathbf{w})\right) - Tr(\boldsymbol{\pi}\mathbf{D_p}\mathbf{w}^T) \tag{2.23}$$

and, by integrating over the mesoderm domain $\Omega_m$ at the reference configuration, we obtain

$$\int_{\Omega_m} (\mathbf{Div_p}\boldsymbol{\pi}, \mathbf{w}) = \int_{\Omega_m} div_{\mathbf{p}}\left(\boldsymbol{\pi}^T(\mathbf{w})\right) - \int_{\Omega_m} Tr(\boldsymbol{\pi}\mathbf{D_p}\mathbf{w}^T) = 0 \tag{2.24}$$

By the Stoke's formula we can write

$$\int_{\Omega_m} div_{\mathbf{p}}\left(\boldsymbol{\pi}^T(\mathbf{w})\right) = \int_{\Omega_m} (\boldsymbol{\pi}^T(\mathbf{w}), \mathbf{n}) = \int_{\partial\Omega_m} (\mathbf{w}, \boldsymbol{\pi}(\mathbf{n}))dS \tag{2.25}$$

therefore

$$\int_{\Omega_m} Tr(\boldsymbol{\pi}\mathbf{D_p}\mathbf{w}^T) = \int_{\partial\Omega_m} (\mathbf{w}, \boldsymbol{\pi}(\mathbf{n}))dS \tag{2.26}$$

We also know that (Holzapfel [2000], Smith [1993])

$$\boldsymbol{\pi}(\mathbf{n})dS = \boldsymbol{\sigma}(\mathbf{n}_x)dS_x = f_s(\mathbf{n}_x)dS_x \tag{2.27}$$

where $f_s$ is the modulus of the real surface forces that are supposed to be like normal pressures on the boundaries of the system. We know that $(\mathbf{n}_x)dS_x = J\,\mathbf{F}^{-T}(\mathbf{n})\,dS$, thus we can substitute in Eq.[2.27] and then in Eq.[2.26] to obtain

$$\int_{\Omega_m} Tr(\boldsymbol{\pi}\mathbf{D}_\mathbf{p}\mathbf{w}^T) = \int_{\partial\Omega_m} (\mathbf{w}, f_s J\,\mathbf{F}^{-T}(\mathbf{n}))dS \tag{2.28}$$

The term on the right hand side bunches all the external loads acting on the external ($\partial\Omega_{m_e}$) or internal ($\partial\Omega_{m_i}$) boundaries of the mesoderm; we will analyze later on in this chapter such loads (Sec. 2.7). On the left hand side instead, the internal forces of the mesodermal domain $\Omega_m$ are represented.

The First Piola-Kirchhoff tensor, appearing on the left hand side term of Eq.[2.28], can actually be written as

$$\boldsymbol{\pi} = \mathbf{F}\,\mathbf{S} \tag{2.29}$$

where $\mathbf{S}$ is the Second Piola-Kirchhoff tensor, which is equal to

$$\begin{aligned}\mathbf{S} &= J\,\mathbf{F}^{-1}\boldsymbol{\sigma}\mathbf{F}^{-T} \\ &= J_m J_a \mathbf{F}_m^{-1}\mathbf{F}_a^{-1}\boldsymbol{\sigma}\mathbf{F}_m^{-T}\mathbf{F}_a^{-T}\end{aligned} \tag{2.30}$$

where $J_m$ and $J_a$ are the determinants of the passive deformation of the mesoderm $\mathbf{F}_m$ and of the active deformation $\mathbf{F}_a$ respectively. Knowing that

$$\boldsymbol{\sigma} = J_m^{-1}\mathbf{F}_m\mathbf{S}_m\mathbf{F}_m^T \tag{2.31}$$

where $\mathbf{S}_m$ is the Second Piola-Kirchhoff tensor with reference to the intermediate configuration, which will define the constitutive law of the mesoderm (see Sec. 2.3) and is expressed as in Eq.[2.35], Eq.[2.30] becomes

$$\mathbf{S} = J_a\mathbf{F}_a^{-1}\mathbf{S}_m\mathbf{F}_a^{-T} = \mathbf{S}_a \tag{2.32}$$

From the previous equation, it has to be noticed that the Second Piola-Kirchhoff tensors are the same for the active and the final configurations, while we can not state the same for the First Piola-Kirchhoff tensors. In fact we write

$$\boldsymbol{\pi}_a = \mathbf{F}_a\mathbf{S}_a = J_a\mathbf{S}_m\mathbf{F}_a^{-T} \tag{2.33}$$

for the active deformation, which is different from the tensor for the final deformation that can be deduced substituting Eq.[2.32] in Eq.[2.29], so that we find

$$\boldsymbol{\pi} = J_a \mathbf{F}_m \mathbf{S}_m \mathbf{F}_a^{-T} = J_a \boldsymbol{\pi}_m \mathbf{F}_a^{-T} \tag{2.34}$$

We can conclude that $\boldsymbol{\pi}$ is directly function of the active deformation $\mathbf{F}_a$ and the passive deformation $\mathbf{F}_m$ through $\mathbf{S}_m$. As previously mentioned (Sec. 2.1) and later on described (Chapter 3), $\mathbf{F}_a$ depends on the elementary forces introduced and therefore changes according to the morphogenetic movement analyzed.

## 2.3 The constitutive law of the mesoderm

As described in Chapter 1, the structure of the *Drosophila* embryo is rather complex since, by the beginning of gastrulation, three different tissue layers start to form: an endoderm, an ectoderm and the mesoderm, which is located between these two. So far it has been very difficult to detect the mechanical characteristics of biological tissues (Davidson et al. [1999] and Forgacs et al. [1998]). It seems that embryonic tissues are more linear than mature tissues and they also appear to behave as visco-elastic materials during embryogenesis (Forgacs et al. [1998]). For the present work we have decided to not consider the visco-elastic effects, even if we are aware that they may highly influence the global response of the system. Furthermore, only the mesoderm has been modelled here, as similarly as many finite elements models described in Sec. 1.2.3.1 and 1.2.6. We assume in fact that the mechanical characteristics of the three embryonic tissues may not be so different and that the mesoderm takes up the most part of the embryo tissues.

We hypothesized that the mesoderm is made of a Saint-Venant material whose constitutive law is written as

$$\mathbf{S}_m = \lambda_L Tr\, \mathbf{E}_m \mathbf{I} + 2\,\mu_L \mathbf{E}_m \tag{2.35}$$

with $\mathbf{E}_m$ the Green-Lagrange elastic strain of the mesoderm defined as

$$\mathbf{E}_m = \frac{1}{2}\left(\mathbf{F}_m^T \mathbf{F}_m - \mathbf{I}\right) \tag{2.36}$$

and $\lambda_L$ and $\mu_L$ are the Lame's constants

$$\begin{aligned} \lambda_L &= \frac{E\,\nu}{(1+\nu)(1-2\,\nu)} \\ \mu_L &= \frac{E}{2\,(1+\nu)} \end{aligned} \tag{2.37}$$

where $E$ is the Young's modulus and $\nu$ the Poisson's coefficient. This approach may not be the best accurate for our specific case; additionally, previous authors

(Muñoz et al. [2007], Taber [2007], Conte et al. [2008]) used a Neo-Hookean material to reproduce the mesoderm. Such model is a particular case of the Mooney-Rivlin material whose constitutive law can be written as follows

$$\boldsymbol{\sigma} = \alpha_1 \mathbf{F}_m \mathbf{F}_m^T + \alpha_2 (\mathbf{F}_m \mathbf{F}_m^T)^{-1} \tag{2.38}$$

where

$$\begin{aligned} \alpha_1 &= \mu_{NH} \left( \beta_{NH} + \frac{1}{2} \right) \\ \alpha_2 &= \mu_{NH} \left( \beta_{NH} - \frac{1}{2} \right) \end{aligned} \tag{2.39}$$

with $\mu_{NH}$ and $\beta_{NH}$ proper constants of the material; specifically, for the case of a Neo-Hookean material, we have $\beta_{NH} = \frac{1}{2}$.

Let us briefly compare the two models. By the definition of the Second Piola-Kirchhoff tensor (see Appendix A), the Cauchy stress tensor $\boldsymbol{\sigma}$ can be replaced, so that Eq.[2.38] becomes

$$\mathbf{S}_m = J \left[ \alpha_1 \mathbf{F}_m^{-1} \mathbf{F}_m \mathbf{F}_m^T \mathbf{F}_m^{-T} + \alpha_2 \mathbf{F}_m^{-1} (\mathbf{F}_m \mathbf{F}_m^T)^{-1} \mathbf{F}_m^{-T} \right] \tag{2.40}$$

Thus, knowing that $\mathbf{C}_m^{-1} = \mathbf{F}_m^{-1} \mathbf{F}_m^{-T}$, we have

$$\mathbf{S}_m = J\, \alpha_1 \mathbf{I} + J\, \alpha_2 \mathbf{C}_m^{-2} \tag{2.41}$$

Now, by the Cayley-Hamilton equation (Holzapfel [2000]), we can write

$$-\mathbf{C}_m^3 + I_{1C} \mathbf{C}_m^2 - I_{2C} \mathbf{C}_m + I_{3C} \mathbf{I} = 0 \tag{2.42}$$

where $I_{1C}, I_{2C}, I_{3C}$ are the principal scalar invariants of $\mathbf{C}_m$ defined as

$$\begin{aligned} I_{1C}(\mathbf{C}_m) &= Tr\, \mathbf{C}_m \\ I_{2C}(\mathbf{C}_m) &= \frac{1}{2} [(Tr\, \mathbf{C}_m)^2 - Tr\, \mathbf{C}_m^2] \\ I_{3C}(\mathbf{C}_m) &= Det\, \mathbf{C}_m \end{aligned} \tag{2.43}$$

Therefore we can easily manipulate Eq.[2.41] and the final expression of $\mathbf{S}_m$ is

$$\begin{aligned}\mathbf{S}_m = &\left[J\,\alpha_1 + \frac{J\,\alpha_2}{I_{3C}^2}((I_{2C}+I_{3C})(1-I_{1C})+I_{2C}^2)\right]\mathbf{I}\\ &+\frac{2\,J\,\alpha_2}{I_{3C}^2}[I_{3C}+I_{2C}(2-I_{1C})]\,\mathbf{E}_m+\frac{4\,J\,\alpha_2 I_{2C}}{I_{3C}^2}\mathbf{E}_m^2\end{aligned} \tag{2.44}$$

We have finally demonstrated that the Neo-Hookean material can be expressed through a quadratic formulation of the Saint-Venant model; the coefficients appearing in Eq.[2.44] are function of the principal scalar invariants of $\mathbf{C}_m$ and of some suitable constants $\mu_{NH} > 0$ and $|\beta_{NH}| \leqslant \frac{1}{2}$ (Smith [1993]). In order to compare the two models, we do a power series expansion linearized to the first order of the Neo-Hookean constitutive law (Eq.[2.44]), knowing that $\mathbf{C}_m$ can also be written as a function of the Green-Lagrange strain tensor $\mathbf{E}_m$, so that $\mathbf{C}_m = 2\,\mathbf{E}_m + \mathbf{I}$. Thus the invariants can be reformulated as follows

$$\begin{aligned}I_{1C}(\mathbf{C}_m) &= Tr(2\,\mathbf{E}_m+\mathbf{I})\\ I_{2C}(\mathbf{C}_m) &= \frac{1}{2}[(Tr\,(2\,\mathbf{E}_m+\mathbf{I}))^2 - Tr\,(2\,\mathbf{E}_m+\mathbf{I})^2]\\ I_{3C}(\mathbf{C}_m) &= Det(\,2\,\mathbf{E}_m+\mathbf{I})\end{aligned} \tag{2.45}$$

and furthermore, $J_m = Det\,\mathbf{F}_m = \sqrt{I_{3C}}$. If we do here too a 1st order development of the invariants and $J_m$, we obtain

$$\begin{aligned}I_{1C}(\mathbf{C}_m) &= 3 + 2\,Tr\,\mathbf{E}_m\\ I_{2C}(\mathbf{C}_m) &= 3 + 4\,Tr\,\mathbf{E}_m\\ I_{3C}(\mathbf{C}_m) &= 1 + 2\,Tr\,\mathbf{E}_m\\ J_m &= 1 + Tr\,\mathbf{E}_m\end{aligned} \tag{2.46}$$

Finally, the 2nd Piola-Kirchhoff tensor $\mathbf{S}_m$ becomes

$$\mathbf{S}_m = [(\alpha_1+\alpha_2)(1+Tr\,\mathbf{E}_m)]\mathbf{I} - 4\,\alpha_2\mathbf{E}_m \tag{2.47}$$

Then, in order to have a vanishing initial stress, we must impose $\alpha_1 = -\alpha_2$ so that we obtain

$$\mathbf{S}_m = -4\alpha_2\mathbf{E}_m = 4\alpha_1\mathbf{E}_m \tag{2.48}$$

and from Eq.[2.35] we have then $\alpha_1 = \mu_L/2$ and $\alpha_2 = -\mu_L/2$.

We have tested the Neo-Hookean model for our simulations, in particular for the germ band extension, and we will discuss more in detail later on the results we have obtained (Sec. 3.3). We notice that they are not so different from the ones for the Saint-Venant material, which supports then our initial choice, especially with regards to some aspects:

- given the difficulty to detect the mechanical characteristics of the embryonic tissues, the Saint-Venant model allows us to have a simple but efficient representation of the material without concerning about specific parameters that would be very tangled to find;
- using a linear and a first order constitutive law for the Saint-Venant material, we skip out the issue about the initial stress that is not often well illustrated in literature.

On the other hand, we are aware that the Saint-Venant model presents some limitations principally because it does not take into account, as similarly as the Neo-Hookean model, the visco-elastic characteristics of the tissues we are studying. For this reason, we would like to improve our model from this point of view, also because so far, to our knowledge, this aspect has not been well developed.

## 2.4 Pseudo-thermal interpretation of the gradient decomposition method

The gradient decomposition method takes into account both the active and the passive deformations of the cells, so that the final deformation can be expressed as in Eq.[2.2]. In this section we propose an interpretation of the present method as an equivalent thermal deformation.

The Green-Lagrange tensor for the passive deformation $\mathbf{E}_m$, defined in Eq.[2.36], can be actually rewritten as follows

$$\begin{aligned}\mathbf{E}_m &= \frac{1}{2}\left(\mathbf{F}_a^{-T}\mathbf{F}^T\mathbf{F}\,\mathbf{F}_a^{-1} - \mathbf{I}\right) = \frac{1}{2}\,\mathbf{F}_a^{-T}\left(\mathbf{F}^T\mathbf{F} - \mathbf{F}_a^T\mathbf{F}_a\right)\,\mathbf{F}_a^{-1} \\ &= \mathbf{F}_a^{-T}\left(\mathbf{E} - \mathbf{E}_a\right)\,\mathbf{F}_a^{-1}\end{aligned} \tag{2.49}$$

where $\mathbf{E}$ and $\mathbf{E}_a$ are the Green-Lagrange tensor for the final and the active deformations respectively; the active deformation gradient $\mathbf{F}_a$ directly appears in the final formula.

Let us analyze the case where the cells are supposed regular in form and neatly distributed within the mesoderm that can then be considered as an isotropic material. By the definition of the Second Piola-Kirchhoff tensor $\mathbf{S}$ (Eq.[2.32]) and of the constituve law of the mesoderm (Eq.[2.35]), which provides $\mathbf{S}_m$, we obtain

$$\mathbf{S} = J_a \left[\lambda_L \, Tr(\mathbf{C}_a^{-1} \, (\mathbf{E} - \mathbf{E}_a) \, \mathbf{C}_a^{-1}) \, + 2 \, \mu_L \, \mathbf{C}_a^{-1} (\mathbf{E} - \mathbf{E}_a) \, \mathbf{C}_a^{-1}\right] \tag{2.50}$$

where $\mathbf{C}_a$ is the Right Cauchy tensor for the active deformation (Eq.[A.11]). The last equation shows two main consequences of the active deformation on the constitutive behaviour:

- $\mathbf{C}_a$ affects the isotropy of the material;
- $\mathbf{E}_a$ acts as a thermal deformation.

Actually, $\mathbf{S}_m$ can be reformulated through a compressed equation as follows

$$\mathbf{S}_m = \mathbf{C} \, : \mathbf{E}_m \tag{2.51}$$

where $\mathbf{E}_m$ can be replaced by Eq.[2.49]. This new expression can also be useful if we consider that the cells composing the embryonic tissue are not geometrically the same, which implies a non-perfect distribution of the elements and therefore the mesoderm must be described as an anisotropic material.

The formula of the Second Piola-Kirchhoff tensor $\mathbf{S}$ becomes then

$$\begin{aligned} \mathbf{S}_{in} &= J_a \left(\mathbf{F}_a^{-1}\right)_{ij} \mathbf{S}_{m_{jl}} \left(\mathbf{F}_a^{-T}\right)_{ln} \\ &= J_a \left(\mathbf{F}_a^{-1}\right)_{ij} \left[\mathbf{C}_{jlqr} \left(\mathbf{F}_a^{-T}\right)_{qt} (\mathbf{E} - \mathbf{E}_a)_{ts} \left(\mathbf{F}_a^{-1}\right)_{sr}\right] \left(\mathbf{F}_a^{-T}\right)_{ln} \end{aligned} \tag{2.52}$$

If we define

$$\mathbf{C}_{ints}^{F_a} = J_a \left(\mathbf{F}_a^{-1}\right)_{ij} \mathbf{C}_{jlqr} \left(\mathbf{F}_a^{-T}\right)_{qt} \left(\mathbf{F}_a^{-1}\right)_{sr} \left(\mathbf{F}_a^{-T}\right)_{ln} \tag{2.53}$$

we finally obtain

$$\mathbf{S} = \mathbf{C}^{F_a} : (\mathbf{E} - \mathbf{E}_a) \tag{2.54}$$

where $\mathbf{C}^{F_a}$ depends then on the applied active deformation. This expression shows again, and perhaps more strikingly, the two contributions of the elementary forces:

- one with respect to the modification of the thermo-elastic stiffness tensor $\mathbf{C}$;
- the other as an initial deformation $\mathbf{E}_a$.

This formulation is interesting as well with respect to the Principle of the Virtual Power. If we introduce Eq.[2.54] in Eq.[2.28], the expression of the mechanical equilibrium of the system, we get

$$\int_{\Omega_m} Tr\left(\left(\mathbf{C}^{F_a} : (\mathbf{E} - \mathbf{E}_a)\right)\left(\mathbf{D_p}\mathbf{w}^T\mathbf{F}\right)_{sym}\right) = \int_{\partial\Omega_m} (\mathbf{w}, f_s J\,\mathbf{F}^{-T}(\mathbf{n}))dS \qquad (2.55)$$

where the subscript $sym$ indicates the symmetric tensor defined as

$$\mathbf{A}_{sym} = \frac{1}{2}(\mathbf{A} + \mathbf{A}^T) \qquad (2.56)$$

If we recall now the expression of a thermal dilatation for small deformations, we can notice that the term $(\mathbf{E} - \mathbf{E}_a)$ is similar to the difference between the final and the initial deformations. In fact we write

$$\boldsymbol{\sigma} = \mathbf{C}(\boldsymbol{\epsilon} - \boldsymbol{\epsilon}^T) = \mathbf{C}(\boldsymbol{\epsilon} - \alpha_T \triangle T \mathbf{I}) \qquad (2.57)$$

where $\boldsymbol{\epsilon}$ and $\boldsymbol{\epsilon}^T$ are the final and the initial deformation, $\mathbf{C}$ is the thermo-elastic stiffness tensor depending on $\lambda_L$ and $\mu_L$ and $\alpha_T$ is the dilatation coefficient. $\triangle T$ is the temperature variation and can be compared here to the active deformation amplitude $\alpha^i(t)$ that will be later defined for each morphogenetic movement (Chapter 3).

## 2.5 Interpretation in the case of a non uniform active zone

We consider now a series of 2D cellular domains in contact with one another as shown in Fig. 2.5; $\Omega_a$ and $\Omega$ are respectively the active and the passive regions. At the left and right boundary we have $\mathbf{u} = 0$.

**Active and passive regions**

Let us analyze only the case of small active deformations, assuming that the elementary forces are limited to the region $\Omega_a$ and constant in it, while they vanish outside. Therefore we have $\boldsymbol{\epsilon}_a \neq 0$ in the $\Omega_a$ domain, while $\boldsymbol{\epsilon}_a = 0$ elsewhere. By the considerations made in the previous section, $\boldsymbol{\sigma}$ can be written as

$$\boldsymbol{\sigma} = \mathbf{C}(\boldsymbol{\epsilon}(\mathbf{u}) - \boldsymbol{\epsilon}_a) \qquad (2.58)$$

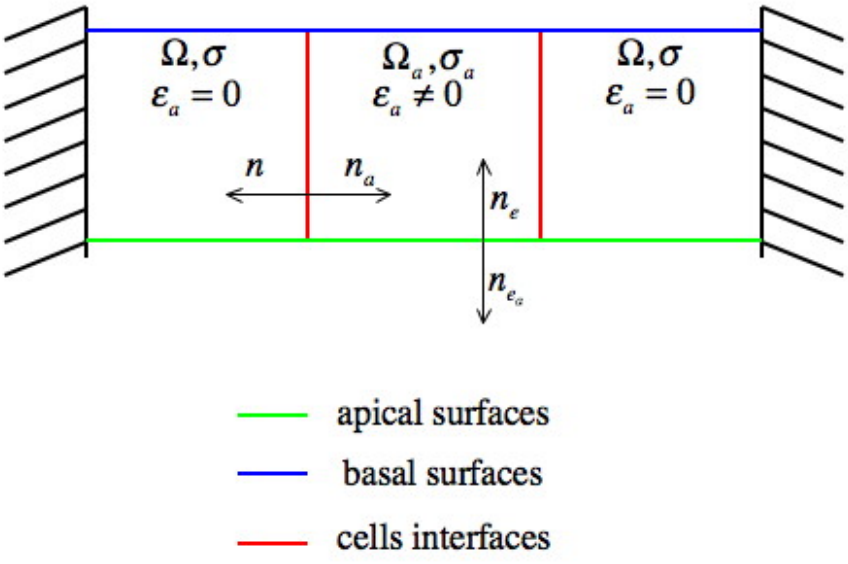


*Figure 2.5:* Series of 2D cellular domains.

**Equivalent volumic forces**

The equilibrium of the system (Eq.[2.17]) is

$$\mathbf{Div_x}\,\boldsymbol{\sigma} = \mathbf{Div_x}\,\mathbf{C}\,\boldsymbol{\epsilon}(\mathbf{u}) - \mathbf{Div_x}\,\mathbf{C}\,\boldsymbol{\epsilon}_a = 0 \tag{2.59}$$

and, for the passive and the active regions, we can actually write

$$\begin{aligned} \Omega: &\quad \boldsymbol{\sigma} = \mathbf{C}\,\boldsymbol{\epsilon}(\mathbf{u}) \\ \Omega_a: &\quad \boldsymbol{\sigma}_a = \mathbf{C}\,(\boldsymbol{\epsilon}(\mathbf{u}_a) - \boldsymbol{\epsilon}_a) \end{aligned} \tag{2.60}$$

For instance, we apply now separately the elementary forces that give rise to the formation of the ventral furrow (Chapter 3), specifically the apical constriction and the apico-basal elongation, and we introduce them in the 2D system. The former provides a deformation depending on both the coordinates along $\mathbf{i}_x$ and $\mathbf{i}_y$, so that we have

$$\boldsymbol{\epsilon}_a = \alpha(y\,\mathbf{i}_x \otimes \mathbf{i}_x + x(\mathbf{i}_x \otimes \mathbf{i}_y + \mathbf{i}_y \otimes \mathbf{i}_x)) \tag{2.61}$$

where $\alpha$ is the deformation amplitude. Thus $\mathbf{Div_x}\boldsymbol{\sigma}_a$ is not constant, contrary to the case of the uniform extension along the apico-basal axis, since we find

$$\boldsymbol{\epsilon}_a = \alpha\, \mathbf{i}_y \otimes \mathbf{i}_y \tag{2.62}$$

Therefore, in cartesian coordinates, even if cell interface forces are observed, we obtain volumic forces only when an apical constriction is applied. A more complex analysis would be required instead for the specific case of the curvilinear coordinates system adopted to describe the embryo geometry.

**Equivalent surface forces at cell interfaces**

We are interested now in evaluating the effects that the active forces have along the cell interfaces. The mechanical equilibrium imposes that:

$$\boldsymbol{\sigma}\,(\mathbf{n}) + \boldsymbol{\sigma}_a\,(\mathbf{n}_a) = 0 \tag{2.63}$$

where $\mathbf{n}$ and $\mathbf{n}_a$ are the outward positive normals for the passive and the active domains respectively (Fig. 2.5). If we introduce the relative expressions for $\boldsymbol{\sigma}$ and $\boldsymbol{\sigma}_a$, we obtain

$$[\mathbf{C}\,\boldsymbol{\epsilon}(\mathbf{u})]\,\mathbf{n} + [\mathbf{C}\,\boldsymbol{\epsilon}(\mathbf{u}_a) - \boldsymbol{\epsilon}_a]\,\mathbf{n}_a = 0 \tag{2.64}$$

so that

$$\mathbf{C}[\boldsymbol{\epsilon}(\mathbf{u}) - \boldsymbol{\epsilon}(\mathbf{u}_a)]\,\mathbf{n} = \mathbf{C}\,\boldsymbol{\epsilon}_a\,\mathbf{n}_a \neq 0 \tag{2.65}$$

Thus the active forces can be replaced by surface forces along the interfaces between the cells that will provide the main modes of deformation. For the specific case of the mesoderm, which is modelled here as a continuum, the only interfaces are the ones between the active region, where the elementary deformations are introduced, and the passive zone. From a mechanical point of view, this means that the transition between the two regions plays a major role and could be the crucial site where the tissues deformation is actually triggered. However we do not know exactly if it is spread out across several cells, one cell or the interface between two cells.

In our formulation, the active region is defined by a Heaviside function, a unit step function with a $C^1$ derivative without overshoot whose value is 0 for a negative argument and 1 for a positive one. The transition between these two values is smoothed within an interval which is user defined and could therefore represent the

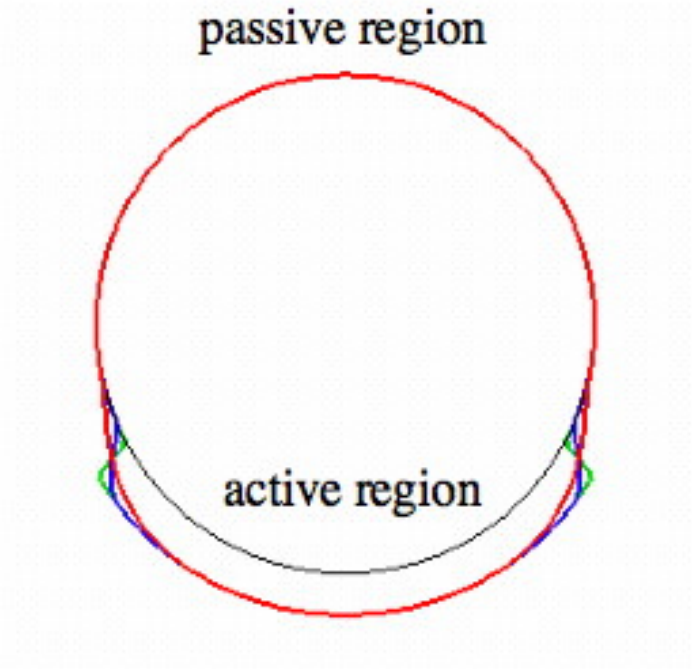


*Figure 2.6:* Example of Heaviside functions on a cercle where an active and a passive regions are defined. The transition between the two zones is determined by an interval which is user defined; the higher the interval, the greater the smoothing effect.

key aspect of the problem (Fig. 2.6).

**Equivalent surface forces at external cell boundaries**

As similarly as for the internal interfaces, we can write the equilibrium along the external surfaces of each cell, thus we have

$$\boldsymbol{\sigma}_a \left(\mathbf{n}_{e_a}\right) = f_s \left(\mathbf{n}_e\right) \tag{2.66}$$

where $\mathbf{n}_{e_a}$ and $\mathbf{n}_e$ are the outward positive normals to the active and the passive domains respectively (Fig. 2.5); $f_s$ corresponds to the surface forces that are assumed here equal to 0, while in the real *Drosophila* embryo they will be the yolk pressure on the internal surface of the mesoderm and the contact with the semi-rigid vitelline membrane. If we recall the expression for $\boldsymbol{\sigma}_a$, the previous equation becomes

$$\mathbf{C}\left(\boldsymbol{\epsilon}(\mathbf{u}_a)\right)\mathbf{n}_e = \mathbf{C}(\boldsymbol{\epsilon}_a)\,\mathbf{n}_{e_a} + f_s\mathbf{n}_e \tag{2.67}$$

Thus, depending on the type of elementary deformation applied in the active region $\Omega_a$, a further boundary force may develop or not on the external cell surfaces and it could also be interpreted as the membrane force of each cell.

**Conclusions**

The previous considerations have shown that the gradient decomposition method leads to interesting interpretations of the equivalent forces that may be generated either along the frontier between the active and the passive regions or at the external cell boundaries.

## 2.6 Validation of the model

In order to validate our formulation, we have decided to test it on simple cases either in cartesian or cylindrical coordinates and in two or three dimensions, where the active region where the elementary forces are applied coincides with the entire domain. The external boundary conditions such as the contact with the vitelline membrane and the pressure exerted by the yolk on the mesoderm are not introduced here. The structures we have decided to analyze present very simple geometries so that, when elementary forces are applied on them, the analytical solution can be easily detected. In addition the dimensions and the mechanical characteristics of the systems are very similar to the ones employed later on for the *Drosophila* embryo; therefore the results obtained are reasonably pertinent and support the approach we have chosen for the present work.

### 2.6.1 Deformation of a 2D beam

First of all we have considered a two dimensional beam in a cartesian system of coordinates $(\mathbf{i}_x, \mathbf{i}_y)$. The beam is $100\mu m$ in length and $20\mu m$ in width.

#### 2.6.1.1 Governing equations

**Kinematics**

Any material point of the beam can be defined by its initial position (before any force applied on the system), which is expressed as follows

$$\mathbf{p} = x\,\mathbf{i}_x + y\,\mathbf{i}_y \tag{2.68}$$

Let us introduce a longitudinal extension, which can be considered as an active elementary force on the system. Therefore each particle of the domain deforms to reach the intermediate position $\bar{\mathbf{x}}$ equal to

$$\bar{\mathbf{x}} = (x + \bar{u})\,\mathbf{i}_x + (y + \bar{v})\,\mathbf{i}_y \tag{2.69}$$

with $\bar{u} = \alpha(t)\,x$ and $\bar{v} = 0$. The deformation amplitude $\alpha(t) = \alpha \cdot t$, with $\alpha = 0.05$, depends on an incremental parameter $t$, which runs from 0 to 1, so that the final maximal deformation of the beam is obtained when $\alpha(t) = \alpha$.

**Constitutive relations**

We use a Saint-Venant material to describe the beam, as already presented in Sec. 2.3, whose constitutive law is defined in Eq.[2.35]. The Young's modulus $E$ is fixed at $100Pa$ (as the one adopted for the embryo (Wiebe and Brodland [2005])) and the Poisson's coefficient $\nu$ is equal to 0.45; thus the Lame's coefficients are obtained from Eq.[2.37]. The values exploited for this specific case are the same employed for the following examples presented in the next sections.

**Equilibrium**

No external forces are considered here, therefore the equilibrium equation takes into account only the internal loads of the system and Eq.[2.28] becomes

$$\int_{\Omega_m} Tr(\boldsymbol{\pi}\mathbf{D}_\mathbf{p}\mathbf{w}^T) = 0 \tag{2.70}$$

**Boundary conditions**

The boundary conditions play here an important role and highly affect the global response of the structure, as already analyzed in Sec. 2.1 for the case of a single cell. We have considered three different cases:

1. a simply supported beam on the lower boundary where $v = 0$ (Fig. 2.7a);
2. a cantilver beam on the left side where $u = v = 0$ and simply supported at the bottom (Fig. 2.7b);
3. a cantilever beam on both sides, $u = v = 0$, and simply supported again at the bottom (Fig. 2.7c).

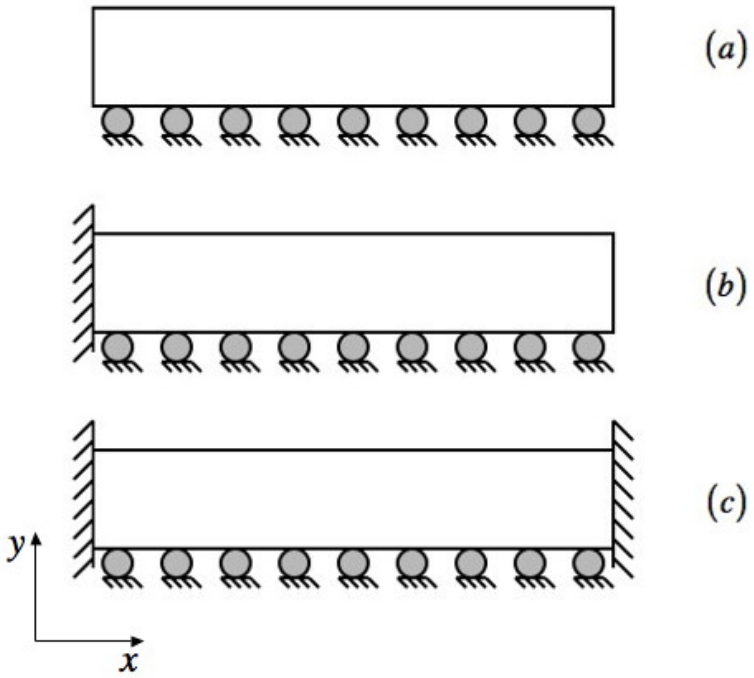


*Figure 2.7:* (a) Free beam (b) One side cantilever beam (c) Two sides cantilever beam.

#### 2.6.1.2 Solution

The active deformation gradient $\mathbf{F}_a$ can be deduced by Eq.[2.4] and we find

$$\mathbf{F}_a = \mathbf{D}_{\mathbf{p}}\bar{\mathbf{x}} = [1 + \alpha(t)]\,\mathbf{i}_x \otimes \mathbf{i}_x + \mathbf{i}_y \otimes \mathbf{i}_y \tag{2.71}$$

The first case corresponds to a free dilatation; each element of the domain undergoes the elementary active deformation applied and changes its shape: therefore the elastic passive deformation $\mathbf{F}_m$ (Eq. [2.2]) is equal to $\mathbf{I}$ so that $\mathbf{F} = \mathbf{F}_a$. The extension is symmetric with respect to the vertical axis of the beam; the maximal horizontal displacement for the left and right boundaries has been analytically found, by the expression of the intermediate position $\bar{\mathbf{x}}$, at $\alpha(t) = \alpha$ and is equal to $\cong \pm 2.5\mu m$ (Fig. 2.8a). The second and the third cases instead represent an example of impeded dilatation; when deformed by $\mathbf{F}_a$, the individual cells are not free to move because of the boundary conditions, therefore $\mathbf{F}_m \neq \mathbf{I}$; thus the maximal displacements are the composition of the active and the passive contributions (Figs.

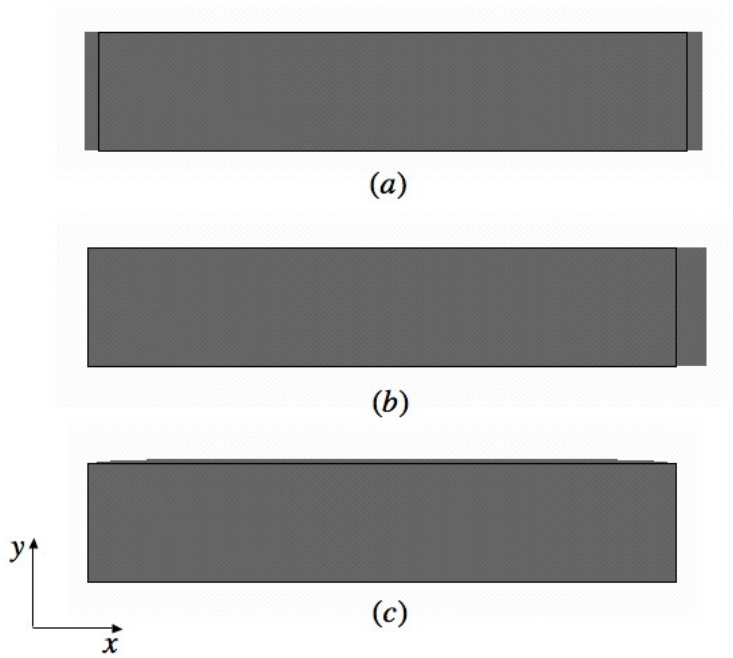


*Figure 2.8:* Longitudinal deformation for a 2D beam. From the top to the bottom: free dilatation (a), impeded dilatation for a one side (b) and both sides (c) cantilever beam.

2.8b, 2.8c). The values of such displacements can not be analytically calculated anymore, but we can deduce them from the numerical simulations. Thus we find: for the second case, at the right boundary of the beam, a maximal extension of about $\cong 5\mu m$, while for the third case the horizontal displacement is much smaller and approximatively equal to $\cong 7 \cdot 10^{-5}\mu m$ at the the centre of the upper boundary. Given the symmetry of this last problem, we were expected to find a horizontal displacement equal to 0, which is not the case here probably due to the very small and therefore negligible errors of the numerical solution.

### 2.6.2 Deformation of a 3D beam

We consider now a three dimensional beam, with same length and width as before and thickness equal to $3\mu m$.

#### 2.6.2.1 Governing equations

**Kinematics**

As similarly as for the two dimensional case, in a three dimensional space $(\mathbf{i}_x, \mathbf{i}_y, \mathbf{i}_z)$, the reference position for a generic point $\mathbf{p}$ of the beam is expressed as

$$\mathbf{p} = x\,\mathbf{i}_x + y\,\mathbf{i}_y + z\,\mathbf{i}_z \tag{2.72}$$

If we apply again an extension in the $\mathbf{i}_x$ direction, the intermediate position $\bar{\mathbf{x}}$ can be written as

$$\bar{\mathbf{x}} = (x + \bar{u})\,\mathbf{i}_x + (y + \bar{v})\,\mathbf{i}_y + (z + \bar{w})\,\mathbf{i}_z \tag{2.73}$$

where $\bar{u} = \alpha(t)\,x$, $\bar{v} = \bar{w} = 0$ and $\alpha(t)$ represents again the amplitude for the longitudinal extension and $t$ the incremental parameter, which runs from 0 to 1; the maximal dilatations for each case, whose values are the same as in the previous section, have been found at $\alpha(t) = \alpha$, $\alpha$ equal to 0.05. The mechanical characteristics of the three dimensional beam are the same as for the two dimensional one; as similarly as for the equation of the final equilibrium of the system.

#### 2.6.2.2 Solution

The active deformation gradient $\mathbf{F}_a$ is equal to

$$\mathbf{F}_a = \mathbf{D}_{\mathbf{p}}\bar{\mathbf{x}} = [1 + \alpha(t)]\mathbf{i}_x \otimes \mathbf{i}_x + \mathbf{i}_y \otimes \mathbf{i}_y + \mathbf{i}_z \otimes \mathbf{i}_z \tag{2.74}$$

We have observed the influence of the boundary conditions on the final results and thus three different cases have been considered as for the two dimensional case (Fig. 2.9). For what concerns the contributions of the active and the passive deformation, the considerations made in the previous section are still valid, therefore the values of the maximal displacements are the same found above (Sec. 2.6.1).

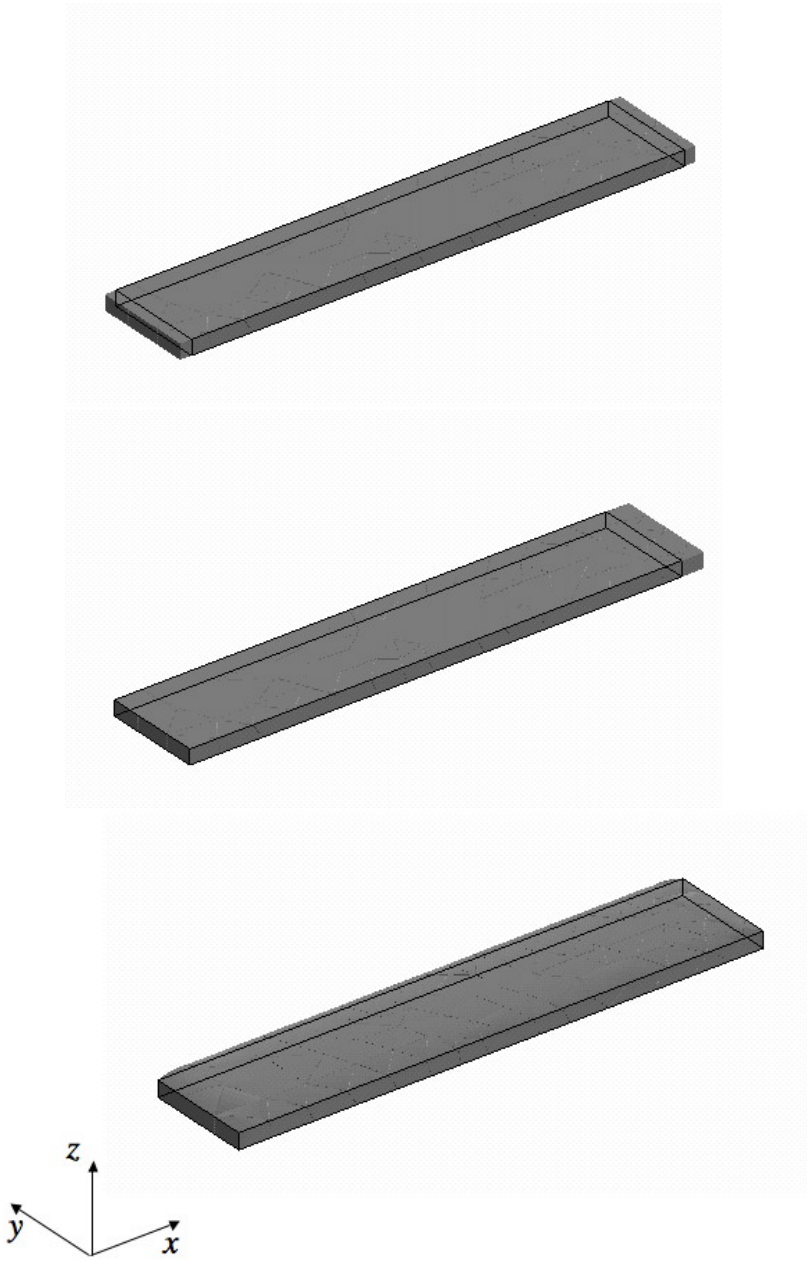


*Figure 2.9:* Longitudinal deformation for a 3D beam. From the top to the bottom: free dilatation, impeded dilatation for a one side and both sides cantilever beam.

### 2.6.3 Radial and circular deformation of a circular cylinder section

Consider now a cross-section of a hollow circular cylinder in a cylindrical polar system of coordinates $(r, \theta, z)$, with radius $r = \sqrt{x^2 + y^2}$. The external and the internal radius are respectively $r_e = 50\mu m$ and $r_i = 45\mu m$ (Fig. 2.10).

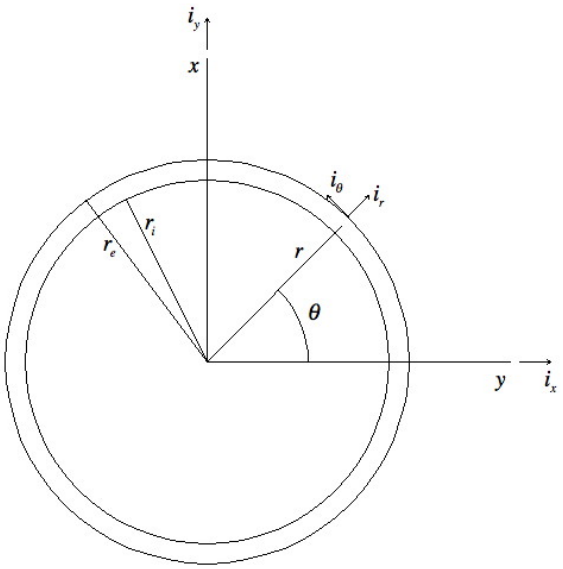


*Figure 2.10:* Cross section of a hollow cylinder.

#### 2.6.3.1 Governing equations

**Kinematics**

A generic point **p** can be located at its initial position by

$$\mathbf{p} = r\,\mathbf{i}_r(\theta) \tag{2.75}$$

where $\theta = arctg\left(\frac{y}{x}\right)$. We have introduced two different elementary forces: a radial dilatation and a circular deformation. For the first case, the intermediate position $\bar{\mathbf{x}}$ can be written as follows

$$\bar{\mathbf{x}}_{rad} = [1 + \alpha(t)]\, r\,\mathbf{i}_r(\theta) \tag{2.76}$$

where $\alpha(t)$ is the amplitude and here again depends on the incremental parameter $t$ varying from 0 to 1. If otherwise we apply a circular deformation, $\bar{\mathbf{x}}$ becomes

$$\bar{\mathbf{x}}_{circ} = r\,\mathbf{i}_r[(1+\alpha(t))\theta] = r\,\mathbf{i}_r(\theta+\theta^*) \tag{2.77}$$

where $\theta^* = \alpha(t)\,\theta$ is the deformation angle and $\alpha(t)$ again determines the deformation amplitude.

**Boundary conditions**

Given the radial symmetry of the problem, we have decided to analyze only a quarter of the structure; thus the relative boundary conditions are imposed. From Fig. 2.10 we deduce that on the left boundary we must impose $u = 0$, while on the lower boundary it is necessary $v = 0$.

#### 2.6.3.2 Solution

The active deformation gradient $\mathbf{F}_a$ in cylindrical polar coordinates is defined as

$$\mathbf{F}_a = \frac{\partial \bar{\mathbf{x}}}{\partial r} \otimes \mathbf{i}_r(\theta) + \frac{\partial \bar{\mathbf{x}}}{\partial \theta} \otimes \frac{\mathbf{i}_\theta(\theta)}{r} \tag{2.78}$$

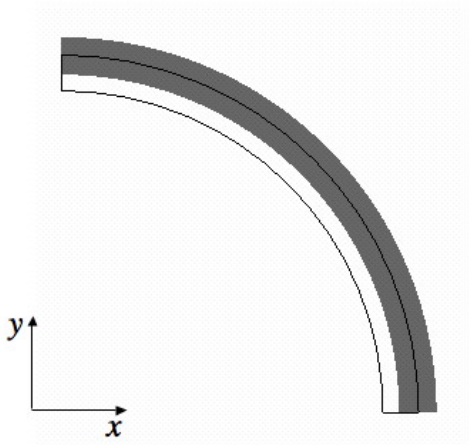


*Figure 2.11:* Radial dilatation for a quarter of a cylindrical section. The scale of the displacements field has been adjusted of a factor $10^2$ in order to better show the dilatation.

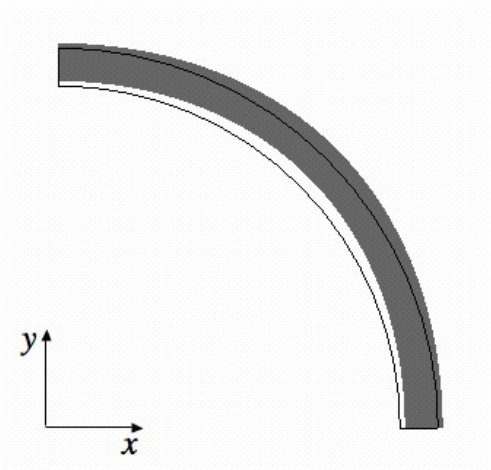


*Figure 2.12:* Circular dilatation for a quarter of a cylindrical section. The scale of the displacements field has been adjusted again of a factor $10^2$.

Therefore for the case of radial dilatation we find

$$\mathbf{F}_{a,rad} = [1 + \alpha(t)]\mathbf{i}_r(\theta) \otimes \mathbf{i}_r(\theta) + [1 + \alpha(t)]\mathbf{i}_\theta(\theta) \otimes \mathbf{i}_\theta(\theta) \tag{2.79}$$

while for the circular deformation, $\mathbf{F}_a$ becomes

$$\mathbf{F}_{a,circ} = \mathbf{i}_r(\theta + \theta^*) \otimes \mathbf{i}_r(\theta) + [1 + \alpha(t)]\, \mathbf{i}_\theta(\theta + \theta^*) \otimes \mathbf{i}_\theta(\theta) \tag{2.80}$$

The equilibrium of the system is obtained, here again, from Eq.[2.28], taking into account the fact that no external forces are introduced. The constitutive law corresponds to the Saint-Venant model previously presented (Eq.[2.35]). The results for both the simulations are shown in Figs. 2.11, 2.12. As for the first case of the two and the three dimensional beam, we observe here a free dilatation of the circular section. Therefore we have again $\mathbf{F}_m = \mathbf{I}$ and then $\mathbf{F} = \mathbf{F}_a$; the maximal displacements for both the radial and the circular deformations can be analytically deduced from the expression of the intermediate position $\bar{\mathbf{x}}$. We find respectively, at $\alpha(t) = 5 \cdot 10^{-4}$, a maximal radial displacement of $\cong 2.5 \cdot 10^{-2} \mu m$ and, for the case of the circular dilatation, a maximal displacement at the left and the bottom boundaries in the order of a few $10^{-3} \mu m$.

### 2.6.4 Radial and circular deformation of a sphere

Among the 3D cases, it is interesting to analyze a sphere whose geometry is simple and regular but more similar to the embryo than the previous examples studied; due to the symmetry of the problem, we only considered a eight of the sphere. The sphere is defined in a spherical system of coordinates $(r, \theta, \varphi)$. The radius is equal to $r = \sqrt{x^2 + y^2 + z^2}$ with $r_e = 100\mu m$ and $r_i = 95\mu m$ (Fig. 2.13).

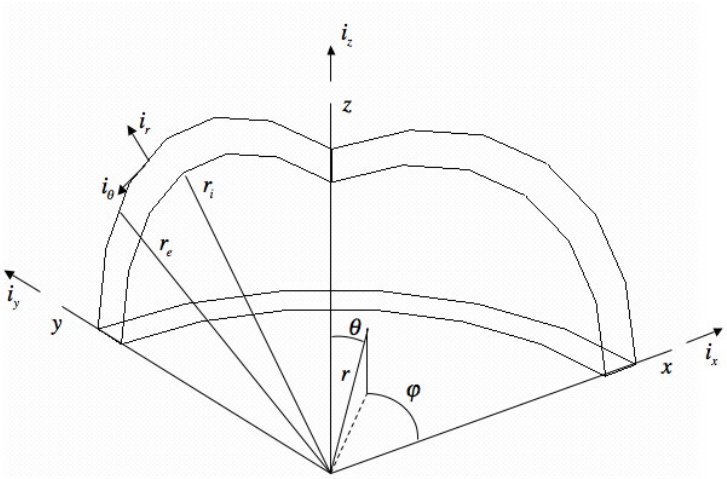


*Figure 2.13:* Geometry of a sphere.

#### 2.6.4.1 Governing equations

**Kinematics**

If we consider a material point of the sphere, its reference configuration is determined by

$$\mathbf{p} = r\,\mathbf{i}_r(\theta, \varphi) \tag{2.81}$$

where here again $\theta = arctg\left(\frac{z}{x}\right)$. As for the circular cylinder, we impose first a radial dilatation and then a circular deformation. Therefore the intermediate position $\bar{\mathbf{x}}$ is, for the first case, expressed as

$$\bar{\mathbf{x}}_{rad} = [1 + \alpha(t)]r\,\mathbf{i}_r(\theta, \varphi) \tag{2.82}$$

In the second case we find instead

$$\bar{\mathbf{x}}_{circ} = r\,\mathbf{i}_r[(1+\alpha(t))\theta, \varphi] \tag{2.83}$$

**Boundary conditions**

Since only a quarter of a sphere has been taken into account, the symmetry conditions have been introduced. Therefore, if we observe the geometry presented in Fig. 2.13, we have

- on the left boundary $u = 0$
- on the right boundary $v = 0$
- on the bottom boundary $w = 0$

#### 2.6.4.2 Solution

The active deformation gradient $\mathbf{F}_a$ can be easily deduced from Eq.[2.78], so that we obtain for the radial dilatation

$$\begin{aligned}\mathbf{F}_{a,rad} =& [1+\alpha(t)]\,\mathbf{i}_r(\theta,\varphi)\otimes\mathbf{i}_r(\theta,\varphi) + [1+\alpha(t)]\,\mathbf{i}_\theta(\theta,\varphi)\otimes\mathbf{i}_\theta(\theta,\varphi) \\ &+ [1+\alpha(t)]\,\mathbf{i}_\varphi(\theta,\varphi)\otimes\mathbf{i}_\varphi(\theta,\varphi)\end{aligned} \tag{2.84}$$

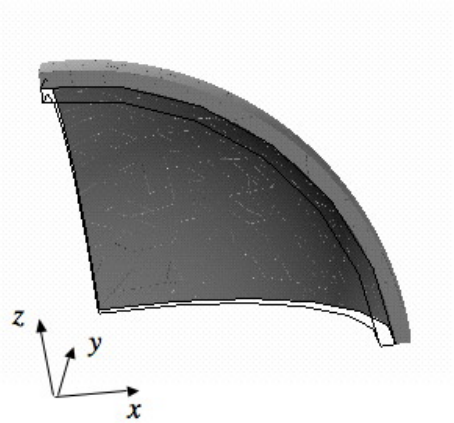


*Figure 2.14:* Radial dilatation for a sphere.

while for the circular deformation we have

$$\begin{aligned}\mathbf{F}_{a,circ} =& \mathbf{i}_r(\theta+\theta^*,\varphi)\otimes\mathbf{i}_r(\theta,\varphi) + [1+\alpha(t)]\,\mathbf{i}_\theta(\theta+\theta^*,\varphi) \\ &+ \mathbf{i}_\varphi(\theta+\theta^*,\varphi)\otimes\mathbf{i}_\varphi(\theta,\varphi)\end{aligned} \tag{2.85}$$

with $\theta^* = \alpha(t)\,\theta$ the deformation angle and $\alpha(t)$ the amplitude for both the deformations. Here again a free deformation is observed. For the first case, the maximal radial displacement obtained, by the intermediate position $\bar{\mathbf{x}}$, at $\alpha(t) = 0.01$ is equal to $5\mu m$ (Fig. 2.14), while for the circular dilatation the displacement is in the order of a few $10^{-3}\mu m$ (Fig. 2.15).

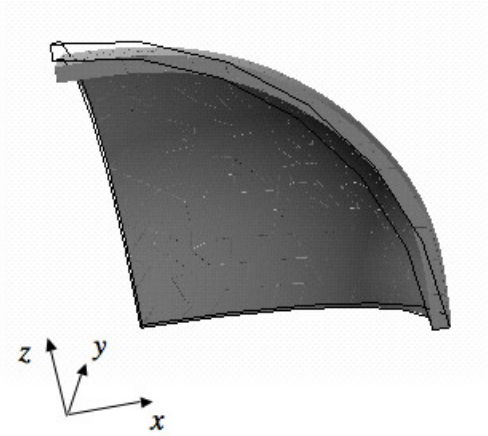


*Figure 2.15:* Circular dilatation for a sphere; for a better representation, the final displacement field has been multiplied by a factor 5.

## 2.7 Required boundary conditions

The weak formula of the mechanical equilibrium of the system found in Eq.[2.28] presents on the left a term representing the internal forces, while the term on the right corresponds to the equilibrium of the surface forces acting on the mesoderm. The fact that we model the mesoderm as a continuum allows us to skip the forces exerted between the cells to maintain the contact with one another. Also we do not take into account the interaction forces external to the mesoderm, but only the contact with the vitelline membrane and the pressure of the yolk on the internal boundary of the mesoderm, that are essential structural elements. We will analyze these aspects in the next two sections (Sec. 2.7.1, 2.7.2); the presence or not of these boundary conditions highly affects the global behaviour of the system, as already observed by previous authors (Conte et al. [2008]), consequently for the present

study we have decided to implement both of them, the external contact with the vitelline membrane and the yolk pressure.

### 2.7.1 Contact with the vitelline membrane

The vitelline membrane is a structure directly adjacent to the mesoderm which surrounds the embryo all along its contour. It is considered to be semi-rigid and it plays a relevant role in the global response of the embryo to mechanical constraints; particularly, it is essential to take into account the contact force existing between the membrane and the mesoderm. We are aware, as already mentioned in Sec. 2.2, that some adhesion forces between the cells membrane and the vitelline membrane may occur, but so far we have not analyzed this aspect from a theoretical point of view. Most of the finite elements models presented in Sec. 1.2.3.1 and Sec. 1.2.6 do not consider the vitelline membrane, even if it represents a key component of the embryo. Very few of them modelled this structural element taking into account its influence on mesoderm invagination.

Muñoz (Muñoz et al. [2007]) and Conte (Conte et al. [2008]) have both demonstrated in their works that the presence of the vitelline membrane is necessary in providing consistent results that agree with experimental observations. Muñoz developed a 2D finite elements model of the ventral furrow invagination (Sec. 1.2.3.1) and he used the same approach as Conte in his 3D model. They represented the vitelline membrane as a rigid external shell and they imposed a sliding condition between the apical surfaces of the cells and the membrane. A master-slave method was adopted (Muñoz and Jelenic [2004]), which allows skipping penalty methods and uses the minimum set of degree of freedom. In order to prevent the discontinuity of the tangents, that may produce an intermittent in the activation of the constraints, they also introduced a $C^1$ continuous B-Spline interpolation smoothing technique on the contact surfaces. *In vivo* studies (Leptin and Grunewald [1990]) proved that the removal of the vitelline membrane caused the opening of the furrow during gastrulation and this is also pointed out by numerical simulations for both the models of Muñoz and Conte (Fig. 1.12). Therefore the vitelline membrane clearly constrains the active deformations of the mesoderm in both the intermediate and final invagination stages.

Pouille (Pouille and Farge [2008]) implemented a reaction pressure of the vitelline membrane normal to the outer boundary of the mesoderm. Such pressure acts when any local increase of the embryo size is detected. By his fluid-dynamic model, he found that the vitelline membrane actually affects the bending of the mesoderm, especially in the ventral domain where the invagination takes place.

For the present work we do not model the vitelline membrane but we use an adaptive penalty method (Belytschko et al. [2000]), which consents to evaluate the contact between the mesoderm and the outer shell. By observing the embryo throughout the developmental phases, two situations must be contemplated: when the meso-

derm invaginates the yolk and when it evaginates exceeding the external boundary (Fig. 2.16). This last situation is forbidden by the assumption of the rigidity of the vitelline membrane.

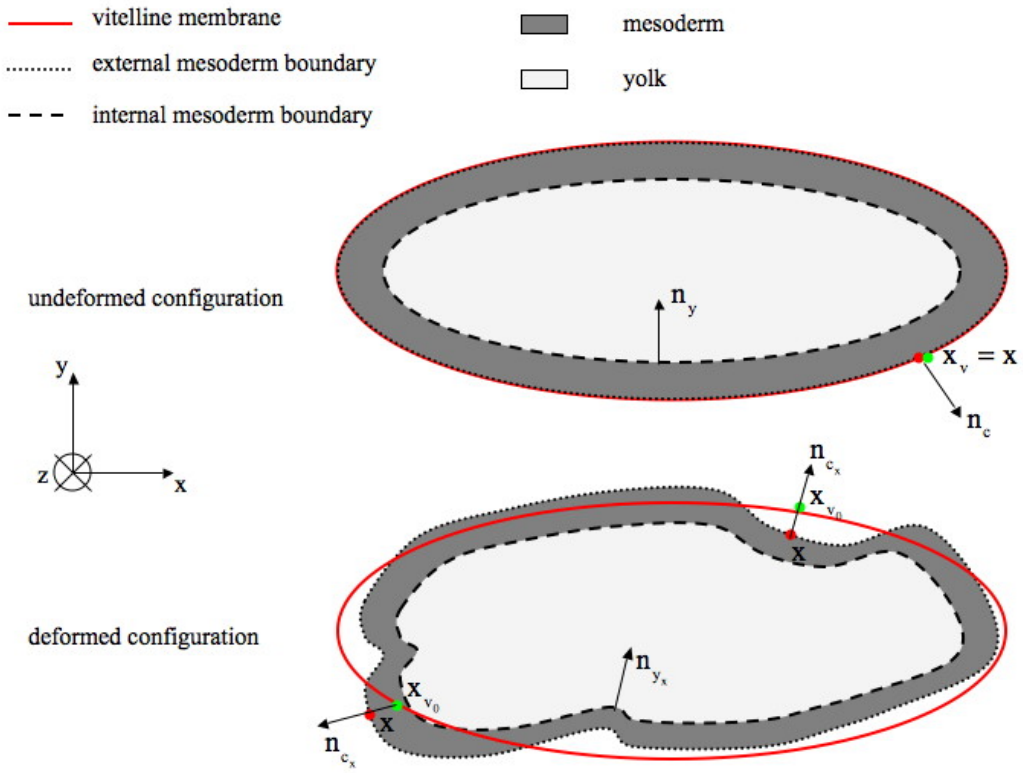


*Figure 2.16:* Geometrical description of invagination and evagination of the mesoderm.

To deal with these cases, we want to check the contact constraint with the vitelline membrane $\partial\Omega_e$, which is defined by the equation

$$f_c(\mathbf{x}_v) = 0 \qquad \forall \mathbf{x}_v \tag{2.86}$$

where $\mathbf{x}_v$ are the points on the vitelline membrane.

We evaluate the distance, at the deformed configuration, between a point $\mathbf{x}$ on the external surface of the mesoderm $\partial\Omega_{m_{ex}}$ and its projection $\mathbf{x}_{v_0}$ on the vitelline membrane. The distance is calculated along the outward positive normal $\mathbf{n}_{c_x}$ to the external boundary of the mesoderm. Therefore we can write

$$f_c(\mathbf{x}_{v_0}) \simeq f_c(\mathbf{x}) + (\nabla f_c(\mathbf{x}), \mathbf{x}_{v_0} - \mathbf{x}) + \cdots = 0 \tag{2.87}$$

from which, in order to evaluate the repulsive forces, we deduce, at first order, the projection $\mathbf{x}_{v_0}$ on the vitelline membrane of the point $\mathbf{x}$

$$\mathbf{x}_{v_0} - \mathbf{x} = s_c \nabla f_c(\mathbf{x}) \tag{2.88}$$

Thus $s_c$ represents the distance we are interested in and can be expressed as

$$s_c(\mathbf{u}) = \frac{-f_c(\mathbf{p}+\mathbf{u})}{|\nabla f_c(\mathbf{p}+\mathbf{u})|^2} \tag{2.89}$$

where the gradient of $f_c$ is evaluated as follows

$$\nabla f_c \div \mathbf{n}_{c_x} = \frac{\mathbf{F}^{-T}(\mathbf{n}_c)}{\|\mathbf{F}^{-T}(\mathbf{n}_c)\|} \tag{2.90}$$

$f_c$ acts as level set function (Osher and Fedkiw [2003], Sethian [1996]), so that

$$\begin{cases} f_c(\mathbf{x}) > 0 & s_c < 0 \\ f_c(\mathbf{x}) < 0 & s_c > 0 \end{cases} \tag{2.91}$$

When writing the Principle of the Virtual Power, we need to know the expression of the boundary force at the reference configuration. By Eq.[2.28] the right hand side term for the specific case of the external contact with the vitelline membrane becomes

$$\int_{\partial\Omega_m} (\mathbf{w}, f_s J\, \mathbf{F}^{-T}(\mathbf{n}))dS = \int_{\partial\Omega_{m_e}} (\mathbf{w}, p_c(s_c) J\, \mathbf{F}^{-T}(\mathbf{n}_c))dS \tag{2.92}$$

where $p_c(s_c)$ is the real pressure applied.

As already said, the major issue comes when $s_c < 0$ and the mesoderm evaginates beyond its boundary. It is necessary in that case to apply a pushing-back force, while, when invagination occurs, we can easily control it by introducing a small constant force. Thus we can write

$$\begin{cases} s_c < 0 & p_c = -t_c\, e^{(k_c s_c)/(t_c)} \\ s_c > 0 & p_c = t_c \end{cases} \tag{2.93}$$

where $t_c$ and $k_c$ are constants whose values will be discussed in the next section.

#### 2.7.1.1 Circular dilation of a sphere when the external contact is introduced

To show the important role played by the vitelline membrane, we take back now the case of the sphere previously analyzed (Sec. 2.6.4) and we apply on the external boundary of the domain the contact force. The values of the constant force $t_c$ and of $k_c$ have been chosen for this particular example and they will be the same for the next simulations. $t_c$ is interpreted here as the adhesion force between the apical surface of a single cell and the vitelline membrane. It has been set at $1Pa$ and can be compared to the traction force exerted by the cytoskeleton on the substrate to which the cells naturally attach. Such force is concentrated at the focal adhesions and it has been estimated between 10 and $30\mu N$ (Nicolas et al. [2004]): the larger the adhesion zone, the higher the traction force. For our case, we assume that the contact force involves the entire apical surface; this justifies the greater value of $t_c$ with respect to the experimental data. The value of $k_c$ has been fixed at $1 \cdot 10^8$ in order to have a maximal mesoderm evagination equal to $0.01\mu m$.

If we recall the example of the circular deformation of a sphere (Fig. 2.15), we notice an inhibition of the displacements compared to the cases where the external contact is not taken into account. Such reduction in deformation is due to the fact that, when the elements dilate, they are pushed back by the repulsive force imposed at the contour.

### 2.7.2 Internal yolk pressure

The yolk is a viscous fluid filling the internal region of the embryo and exerting a pressure on the internal surface of the mesoderm. The presence of the yolk can actually inhibit the invagination of the mesoderm as it has been noticed through several numerical simulations (Ramasubramanian and Taber [2006], Conte et al. [2008]). Therefore in the latest models in the literature it has been taken into account as a required component in order to have consistent results. There is still an open question whether the fluid is incompressible or presents a residual pressure at the onset of ventral furrow invagination. Conte (Conte et al. [2008]) implemented both the constancy of the volume and the initial pressure of the yolk using a penalty method where the total elastic potential of the epithelium is coupled with an extra potential depending on the initial and the final volumes of the fluid. This approach allows not to consider the yolk as a fluid, but it ensures at the same time the minimal variations in volume. The only drawback of the method lies in the choice of the penalty parameter, which is function of the stiffness of the embryo; in their study Conte and co-authors found volume variations less than 3.5%.

Taber modelled the yolk for the analysis of shell problems (Ramasubramanian and Taber [2006], Taber [2007]); he introduced hydrostatic incompressible fluid elements and, by an auxiliary weak constraint condition, the embryo cavity was main-

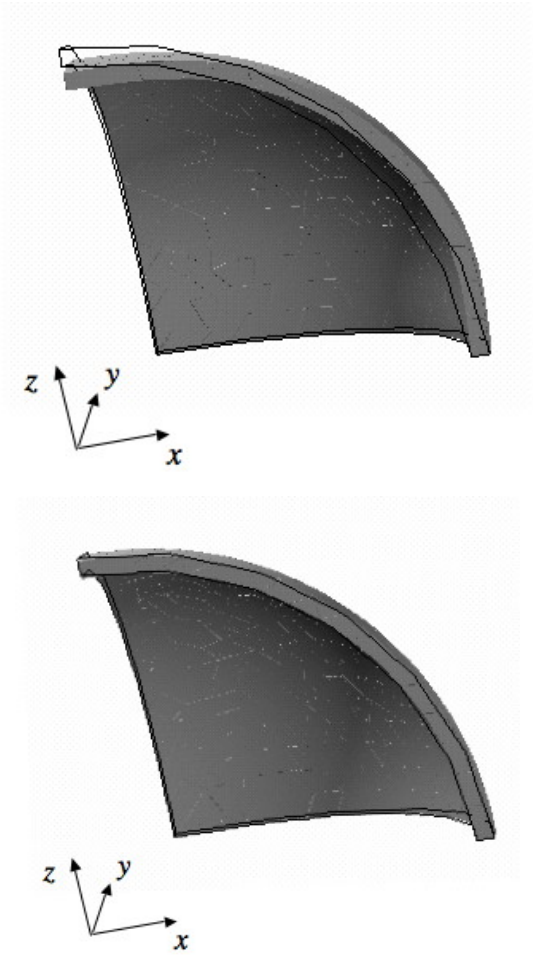


*Figure 2.17:* At the top the circular dilatation of the sphere without surface forces, at the bottom the same example when the external contact is taken into account (for both the images the displacements field has been adjusted of a factor 5).

tained at constant volume. He observed that the presence of the yolk dramatically reduced the amount of invagination in the shell with a cylindrical shape, while for the spheric ones a marginal decrease was detected. The deformation of the fluid-filled shell is lasted by the stretching of the shell elsewhere, which demands more force than bending and restrains the quantity of fluid that can be displaced by the invaginating cells.

The yolk is considered here as a compressible fluid, therefore we introduce a

uniform pressure $p_y$ coupled with the global change of its volume. This method is computationally efficient since we skip out the meshing of the yolk, thus we have a drastic decreasing of the number of degree of freedom.

We define the actual inner volume $V_y$, enclosed by the yolk, as

$$V_{y_x} = \int_{\Omega_{m_{i_x}}} dV \tag{2.94}$$

Because of the Stoke's formula, the previous equation can be rewritten as follows

$$V_{y_x} = \int_{\Omega_{m_{i_x}}} \frac{div\,\mathbf{x}}{3} dV_x = \frac{1}{3}\int_{\Omega_{m_{i_x}}} (\mathbf{x}, \mathbf{n}_{y_x}) dS_x = \frac{1}{3}\int_{\partial\Omega_{m_i}} [\mathbf{x}, J\,\mathbf{F}^{-T}(\mathbf{n}_y)]\, dS \tag{2.95}$$

where $\mathbf{n}_{y_x}$ and $\mathbf{n}_y$ are the positive inward normals to the internal boundary of the mesoderm at the deformed and undeformed configuration respectively.

Given the assumption of a fluid at rest, the applied pressure $p_y(V_y)$, with $V_y$ the initial volume of the yolk, should satisfy the following pressure-volume law

$$p_y = p_{y_0} - k_y \frac{V_{y_x} - V_y}{V_y} = p_{y_0} - \frac{k_y}{V_y}\int_{\partial\Omega_m} (J\,\mathbf{F}^{-1}(\mathbf{p}+\mathbf{u}) - \mathbf{p}, \mathbf{n}_y) dS \tag{2.96}$$

where $p_{y_0}$ and $k_y$ are respectively the initial pressure and the compressibility coefficient of the yolk; in Sec. 3.4 we will discuss more in detail the choice of these two constants. From the formulation of the Principle of the Virtual Power (Eq. [2.28]), we can write the second right hand side term as follows

$$\begin{aligned}
&\int_{\partial\Omega_{m_i}} [\boldsymbol{\pi}(\mathbf{n}_y), \mathbf{w}]\, dS = \int_{\partial\Omega_{m_i}} [p_y(V_y)(\mathbf{n}_y), \mathbf{w}]\, dS \\
&= \int_{\partial\Omega_{m_i}} p_y(V_y)[J\,\mathbf{F}^{-T}(\mathbf{n}_y), \mathbf{w}] dS \\
&= \int_{\partial\Omega_{m_i}} p_y \left(\frac{1}{3}\int_{\partial\Omega_{m_i}} [\mathbf{x}_a, J\,\mathbf{F}^{-T}(\mathbf{n}_{y_a})] dS\right) [J\,\mathbf{F}^{-T}(\mathbf{n}_{y_b}), \mathbf{w}] dS
\end{aligned} \tag{2.97}$$

Thus there is a double integration: the first one to get the correct yolk pressure (indicated here by the subscript $a$) and the second one to get the virtual work on the internal boundary of the mesoderm (indicated here by the subscript $b$). The numerical issue related to this peculiar term will be discussed in the following section.

## 2.8 Iterative scheme and finite elements approximation

We recall here the weak formula of the mechanical equilibrium of the system, obtained in Sec. 2.2, which can be rewritten as follows

$$\begin{aligned}\int_{\Omega_m} Tr\left(\boldsymbol{\pi}(\mathbf{u},\alpha^i(t)),\mathbf{D_p}\mathbf{w}^T\right) = &\int_{\partial\Omega_{m_e}} \left(p_c J\mathbf{F}^{-T}(\mathbf{n}_c),\mathbf{w}\right) dS \\ &+ \int_{\partial\Omega_{m_i}} \left(p_y J\mathbf{F}^{-T}(\mathbf{n}_y),\mathbf{w}\right) dS\end{aligned} \tag{2.98}$$

where the left hand side term represents the internal forces expressed by the First Piola-Kirchhoff tensor $\boldsymbol{\pi}$, which is function of the displacement $\mathbf{u}$ and of the deformation amplitude $\alpha^i(t)$ that will be later on defined and change according to the morphogenetic movement considered. The right hand terms instead represent respectively the contact force between the mesoderm and the vitelline membrane and the pressure force exerted by the yolk on the internal boundary of the mesoderm. Such expression is proposed here to describe the numerical method employed for the present work, which consists of an incremental implicit scheme through the evolution parameter $t$, together with a Newton technique to solve the corresponding non linear problem at each time step.

The time interval $]0,T[$ is decomposed into $t_n$ steps, $n=1,N$, and, starting from usual vanishing initial values, the displacement $\mathbf{u}^{n+1}$ is computed, so that we obtain

$$\begin{aligned}\int_{\Omega_m} Tr\left(\boldsymbol{\pi}(\mathbf{u}^{n+1},(\alpha^i(t))^{n+1}),\mathbf{D_p}\mathbf{w}^T\right) = &\int_{\partial\Omega_{m_e}} \left[\left(p_c J\mathbf{F}^{-T}(\mathbf{n}_c)\right)^{n+1},\mathbf{w}\right] dS \\ &+ \int_{\partial\Omega_{m_i}} \left[\left(p_y J\mathbf{F}^{-T}(\mathbf{n}_y)\right)^{n+1},\mathbf{w}\right] dS\end{aligned} \tag{2.99}$$

With respect to the space variable, the displacement vector is decomposed on the classical finite element basis function with Lagrangian polynomial of degree two on a thetrahedral mesh. The convergence criterion is based on the $L^2$ norm of the displacement with a tolerance $10^{-2}$ on the relative error. The derivation of the Newton scheme is done in the following way: at iteration $k+1$ and time step $n+1$, the previous equilibrium equation is expanded with respect to $\mathbf{u}^{n+1,k}$, thus we have

$$\int_{\Omega_m} Tr\left[\boldsymbol{\pi}\left(\mathbf{u}^{n+1,k},(\alpha^i(t))^{n+1}\right),\mathbf{D_p}\mathbf{w}^T\right]-\int_{\partial\Omega_{m_e}}\left[\left(p_cJ\mathbf{F}^{-T}\right)^{n+1,k}(\mathbf{n}_c),\mathbf{w}\right]dS$$
$$-\int_{\partial\Omega_{m_i}}\left[\left(p_yJ\mathbf{F}^{-T}\right)^{n+1,k}(\mathbf{n}_y),\mathbf{w}\right]dS$$
$$+\int_{\Omega_m} Tr\left[\mathbf{D_u}\boldsymbol{\pi}\left(\left(\mathbf{u}^{n+1,k}\right)\delta\mathbf{u}^{n+1,k+1},\left(\alpha^i(t)\right)^{n+1}\right),\mathbf{D_p}\mathbf{w}^T\right]$$
$$-\int_{\partial\Omega_{m_e}}\left[\mathbf{D_u}\left(p_cJ\mathbf{F}^{-T}\right)^{n+1,k}\delta\mathbf{u}^{n+1,k+1}(\mathbf{n}_c),\mathbf{w}\right]dS$$
$$-\int_{\partial\Omega_{m_i}}\left[\mathbf{D_u}\left(p_yJ\mathbf{F}^{-T}\right)^{n+1,k}\delta\mathbf{u}^{n+1,k+1}(\mathbf{n}_y),\mathbf{w}\right]dS=0 \tag{2.100}$$

so that the displacement increment $\delta\mathbf{u}^{n+1,k+1}$ can be computed by the solution of a linear system.

### Yolk pressure and contact with the vitelline membrane

The yolk boundary condition presents a special issue because it is non local. This is mostly due to the fact that the yolk is assumed here to be a fluid at rest and there is a relation between its global volume change and the uniform pressure applied on the mesoderm, as shown in Eq.[2.96]. Therefore, as described in Eq.[2.97], we get a double integral: one provides the correct yolk pressure, the other the virtual work on the internal boundary $\partial\Omega_{m_i}$ of the mesoderm. This leads to a Jacobian matrix $\mathbf{D_u}\left(p_yJ\mathbf{F}^{-T}\right)^{n+1,k}$ where all the nodes at the boundary are coupled. Given several difficulties related to the large computer memory required, we have decided to compute the Jacobian one iteration behind in order to annihilate such complex coupling between the nodes of the inner boundary. The computational cost is very much reduced with no noticeable degradation in the number of Newton iterations until convergence. The different examples that have been treated never showed any pathological difficulty inherited from this simplified choice. This is certainly due to the fact that only average volume occurs in the expression of the pressure, which is consequently not significantly oscillating.

For what concerns the contact with the external vitelline membrane, we still have to consider it as a non linear boundary condition, but, contrary to the yolk, it is locally defined.

## 2.9 Hints for a future stability analysis

The convergence of the previous Newton scheme crucially depends on the Jacobian of the First Piola-Kirchhoff tensor with respect to the displacement. In this paragraph, we try to evaluate this quantity through an incremental analysis.

The derivative term $\mathbf{D_u}\boldsymbol{\pi}\left(\mathbf{u}, \alpha^i(t)\right)$, as similarly as $\left(\mathbf{D_u}\, p_c J\, \mathbf{F}^{-T}\right)$ for the contact force and $\left(\mathbf{D_u}\, p_y J\, \mathbf{F}^{-T}\right)$ for the yolk pressure, can be obtained from the following rate type equation

$$\frac{d\boldsymbol{\pi}}{dt} = \mathbf{D_u}\boldsymbol{\pi}\,\frac{d\mathbf{u}}{dt} + \mathbf{D}_{\alpha^i}\boldsymbol{\pi}\frac{d\alpha^i(t)}{dt} \tag{2.101}$$

where $t$ is the incremental parameter, which determines the amplitude $\alpha^i(t)$ (see Chapter 3), and $\mathbf{u}$ is the displacement. Since $\boldsymbol{\pi} = \mathbf{F}\,\mathbf{S}$, the term on the left hand can actually be expressed as

$$\frac{d\boldsymbol{\pi}}{dt} = \frac{d\mathbf{F}}{dt}\,\mathbf{S} + \mathbf{F}\,\frac{d\mathbf{S}}{dt} \tag{2.102}$$

with $\mathbf{F}$, the final deformation gradient, equal to $\mathbf{F} = \mathbf{I} + \mathbf{D_p}\mathbf{u}$, so that its derivative becomes

$$\frac{d\mathbf{F}}{dt} = \mathbf{D_p}\left(\frac{d\mathbf{u}}{dt}\right) \tag{2.103}$$

The Second Piola-Kirchhoff tensor $\mathbf{S}$ can be formulated here as in Eq.[2.54], thus we obtain

$$\frac{d\mathbf{S}}{dt} = \frac{d\mathbf{C}^{F_a}}{dt} : (\mathbf{E} - \mathbf{E}_a) + \mathbf{C}^{F_a} : \left(\frac{d\mathbf{E}}{dt} - \frac{d\mathbf{E}_a}{dt}\right) \tag{2.104}$$

Then Eq.[2.102] can be rewritten as

$$\begin{aligned}\frac{d\boldsymbol{\pi}}{dt} = {} & \mathbf{D_p}\left(\frac{d\mathbf{u}}{dt}\right)\left[\mathbf{C}^{F_a} : (\mathbf{E} - \mathbf{E}_a)\right] + \mathbf{C}^{F_a} : \mathbf{F}^T\mathbf{D_p}\left(\frac{d\mathbf{u}}{dt}\right) \\ & + \mathbf{F}\left[\frac{d\mathbf{C}^{F_a}}{dt} : (\mathbf{E} - \mathbf{E}_a) - \mathbf{C}^{F_a} : \frac{d\mathbf{E}_a}{dt}\right]\end{aligned} \tag{2.105}$$

This last equation expresses the dependency of $\boldsymbol{\pi}$ on both the gradient of the velocity $\frac{d\mathbf{u}}{dt}$ and the increment of the active deformations. The analysis of the tangent stiffness appearing in the first and the second terms of the equation would give the path to evaluate the stability of the highly non linear problem. Such aspect is not further elaborated for the present work, but it may be the object of future studies.

## 2.10 Conclusions

This section of the work has provided a general overview of the approach used for the analysis of the specific morphogenetic movements that will be described in details in the next chapter.

A single cell naturally tends to deform because of chemical signals developing through the cytoskeleton. Such free deformation is not completely possible when the cell, with other cells, is part of a system and therefore constrained not only by its neighbours but also by external boundary conditions. This is the case of the embryo where the cells are in contact with one another and with the yolk and the vitelline membrane on their basal and apical surfaces respectively. Therefore when the elementary forces occur, the cells modify their shape, but a geometrical incompatibility (i.e. superposition of the volumes) is observed which does not guarantee the continuity of the system; therefore the mesoderm reacts and the passive deformation takes place.

The gradient decomposition method is very useful since it allows to take into account both the active and the passive deformations that are strongly interconnected and have to be composed to obtain the final and correct tissues deformation. The necessary abstract tools have been amply described in this chapter. In particular we have focused on the computation of the active deformation gradient, which, in the curvilinear coordinates system later on introduced, changes according to each morphogenetic movement considered and therefore to the elementary forces introduced. Also we have shown how, by the Principle of the Virtual Power, we express the mechanical equilibrium of the system that includes both the forces at the interior of the domain and the boundary conditions, such as the yolk pressure and the vitelline membrane. Actually these two components, even if not explicitly modelled here, are essential structural elements and the absence of one or both of them may lead to final configurations that do not correspond to experimental observations.

If from a mechanical point of view the gradient decomposition method is natural and logic and often used for large deformations problems, biologists may be perplex in finding the physical meaning of such approach. Thus we have proposed some interesting interpretations of the method that have pointed out novel aspects so far unexplored and further hints of discussion. Specifically, we have presented the similarities between our formulation and the stress analysis in thermodynamics problems. This analysis better clarifies the composition of the active and the passive deformations, which is here compared to the initial and final contributions in thermal dilatation. Additionally, we have shown the local effects of the active forces introduced in our formulation. First of all, we have concluded that they could be replaced by surface forces along the cells interfaces that would provide the main deformation modes. For our specific case, it seems to us that the transition between the active and the passive regions constitutes the crucial site where the deformation is actually triggered and it has therefore to be taken into account very carefully.

Secondly, we have noticed that, when introducing the active forces in the active domain, we also collect a consequent strain at the internal and external boundaries, to include with the already present yolk pressure and the contact with the vitelline membrane.

Another point on which biologists may not fully agree concerns the choice of the constitutive law of the mesoderm. For the present work we have opted for a linear Saint-Venant model that does not consider instead the non-linearities of the material provided by its visco-elastic traits and, additionally, it is in contrast with the previous works where a Hyperelastic material has often been used. The main reason for this choice is the lack in information about the mechanical characteristics of the mesoderm that are usually very difficult to detect. Although we have compared the two models and we will show later that the results for both cases are not so different, which is also probably due to the very small deformations occurring to the mesoderm. However we are aware that the Saint-Venant material presents some limitations and therefore we are working on those aspects so far put aside. On the other hand it is evident that the analysis of a biological system is not always easy for the many parameters that take part to the processes, thus the hypothesis made, even if simplistic at first sight, may still be useful for a qualitative analysis of the problem.

Finally we have briefly presented the numerical method used to solve the non linear problem; it consists of an incremental implicit scheme together with a Newton technique. Special caution has to be made for the implementation of the yolk pressure which is not local therefore treated here at a fixed point to avoid large computer memory. Additionally we have analyzed the stability of the solution in order to evaluate the critical values of the incremental parameter at which bifurcation effects may occur and thus affect the right properties of convergence.

In the next chapter we are going to focus on each morphogenetic movement. Specifically we will show how, from the analytical expression of the intermediate position of a generic point, which changes according to the elementary forces applied, we obtain the equation corresponding to the active deformation gradients.

# Chapter 3

# Morphogenetic movements in Drosophila embryo

This section of the work is dedicated to the detailed description of the relative formulations for the three morphogenetic movements: the two furrows (ventral and cephalic) are presented together in Sec. 3.2, while the germ band extension in Sec. 3.3. In particular, we show how we obtain, by the parametrical description of the embryo in a curvilinear system of coordinates (Sec. 3.1), the reference configuration of a material point and its intermediate position when the primary forces are introduced. The active deformation gradients change according to the active deformations and they are therefore user defined and proper to each morphogenetic movement considered.

In the second part of the chapter we present the results obtained (Sec. 3.4), evaluating them for each simulation. For the ventral furrow, a parametric analysis has been conducted, pointing out the variables that may influence the final configuration, such as the size of the active region (Sec. 3.5.1), the dimensions of the material cells (Sec. 3.5.2) and the presence of the apico-basal elongation (Sec. 3.5.3). In Sec. 3.9 and 3.10 we propose an estimation of the induced pressures and shear stress that are engendered elsewhere than the active regions when the elementary deformations are applied on the cells. This analysis in particular allows us to confirm not only qualitatively, but also from a quantitative point of view, some hypotheses put forward by biologists.

As said in Sec. 1.3 and 2.1, we use an ellipsoid to model the embryo, which has to be considered as an approximation of the real biological system. Actually in this way we do not consider the different curvature between the anterior and the posterior pole, which may influence those movements occurring along the anterior-posterior axis such as ventral furrow invagination and germ band extension. Therefore we have performed an interesting collateral study, in collaboration with Anne-Sophie Mouronval of the MSSMat Laboratory, that consents to compare different geometries

more and more similar to the structure of the embryo. The results are shown in Sec. 3.11.

Finally, we discuss here the simulation of the germ band extension when a Hyperelastic material is introduced to represent the mesoderm (Sec. 3.8); the comparison between this model and the Saint-Venant model, adopted for our study, has been extensively argued in Sec. 2.3.

## 3.1 Parametrical description of the embryo

Our model is not obtained by MRI (Magnetic Resonance Imaging) scans that allow to have a precise description of one embryo but make difficult to analyze the influence of several parameters that take part to each morphogenetic movement. Only the mesoderm has been modelled, as mentioned in Sec. 2.3, and it is represented as an ellipsoid in a cylindrical polar basis $(r, \theta, z)$ (see Appendix C), where

$$\begin{aligned} \mathbf{i}_r &= (\cos\theta, \sin\theta, 0) \\ \mathbf{i}_\theta &= (-\sin\theta, \cos\theta, 0) \\ \mathbf{i}_z &= (0, 0, 1) \end{aligned} \tag{3.1}$$

Variations on this peculiar geometry will be discussed at the end of this chapter.

Each point $\mathbf{p}_0$ of the middle surface $\Omega_{m_0}$ of the mesoderm (where $\zeta = 0$), at the initial configuration, is then expressed in this curvilinear coordinates system as follows

$$\mathbf{p}_0(\theta, z) = \rho(z)\mathbf{i}_r(\theta) + z\mathbf{i}_z \tag{3.2}$$

where $\rho(z)$ parametrically describes the geometry and is equal to

$$\rho(z) = b\sqrt{1 - \left(\frac{z}{a}\right)^2} \tag{3.3}$$

with $\theta = \arctan\left(\frac{z}{y}\right)$, $a$ and $b$ the semi axes of the ellipsoid.

Since some deformations will be described with respect to the middle surface of the mesoderm, it is important to define the reference position of any point through the thickness of the mesoderm as

$$\mathbf{p}(\theta, z, \zeta) = \mathbf{p}_0(\theta, z) + \zeta\mathbf{n}_0(\theta, z) \tag{3.4}$$

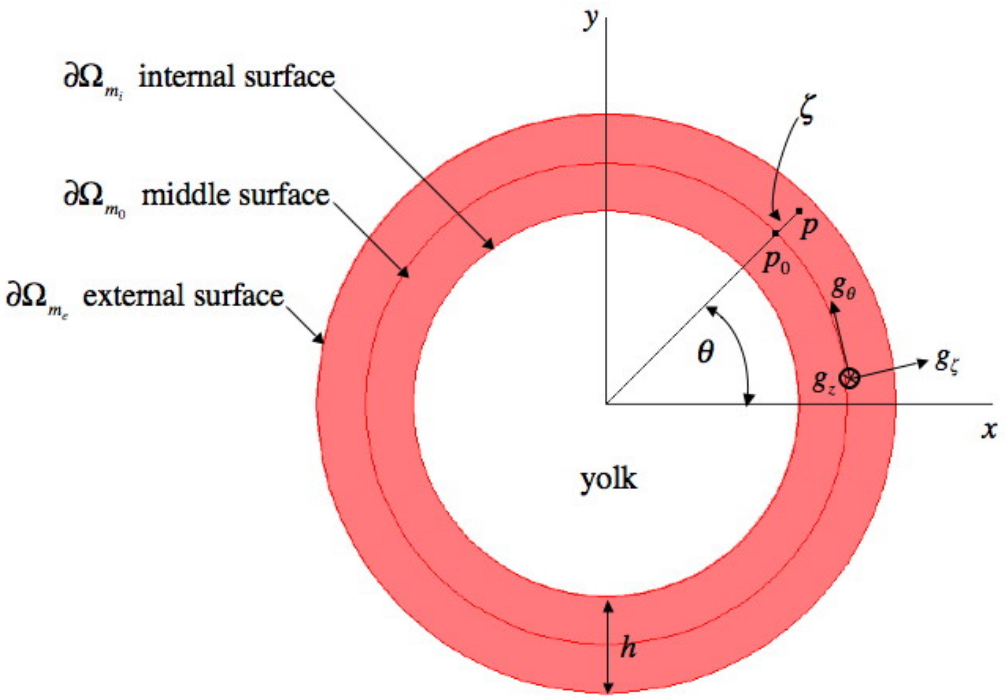


*Figure 3.1:* Cross-sectional view of the ellipsoid representing the embryo at $z = 0$.

where $\zeta$ is the distance between $\mathbf{p}$ and its projection $\mathbf{p}_0$ on the middle surface of the mesoderm (Fig. 3.1). The normal $\mathbf{n}_0(\theta, z)$ to the middle surface can be written as

$$\mathbf{n}_0(\theta, z) = \frac{\frac{\partial \mathbf{p}_0}{\partial \theta} \wedge \frac{\partial \mathbf{p}_0}{\partial z}}{|\frac{\partial \mathbf{p}_0}{\partial \theta} \wedge \frac{\partial \mathbf{p}_0}{\partial z}|} = \frac{-\rho'(z)\mathbf{i}_z + \mathbf{i}_r(\theta)}{\sqrt{1+\rho'^2}} \tag{3.5}$$

When the elementary deformations take place, any point $\mathbf{p}$ deforms to an intermediate position $\bar{\mathbf{x}}$. For each morphogenetic movement, we are interested in analytically finding this intermediate position that consents to obtain the expression of the active deformation gradient $\mathbf{F}_a$, which is classically defined as presented in Chapter 2 and here specifically expressed for the case of this curvilinear system as

$$\mathbf{F}_a = \frac{\partial \bar{\mathbf{x}}}{\partial \theta} \otimes \boldsymbol{\nabla}_{\mathbf{p}}\theta + \frac{\partial \bar{\mathbf{x}}}{\partial z} \otimes \boldsymbol{\nabla}_{\mathbf{p}} z + \frac{\partial \bar{\mathbf{x}}}{\partial \zeta} \otimes \boldsymbol{\nabla}_{\mathbf{p}}\zeta \tag{3.6}$$

where

$$\begin{aligned}\boldsymbol{\nabla}_{\mathbf{p}}\theta &= \frac{\mathbf{g}_z \wedge \mathbf{g}_\zeta}{g} \\ \boldsymbol{\nabla}_{\mathbf{p}} z &= \frac{\mathbf{g}_\zeta \wedge \mathbf{g}_\theta}{g} \\ \boldsymbol{\nabla}_{\mathbf{p}}\zeta &= \frac{\mathbf{g}_\theta \wedge \mathbf{g}_z}{g}\end{aligned} \tag{3.7}$$

form the *contravariant* basis in $\mathbf{p}$ (see Sec. 2.1) and $g$ is defined as in Eq.[2.15].

$\mathbf{g}_\theta, \mathbf{g}_z, \mathbf{g}_\zeta$ are instead the tangent vectors to the curve when $\zeta \neq 0$ and they can be calculated from Eq.[3.4] as

$$\begin{aligned}\mathbf{g}_\theta &= \frac{\partial \mathbf{p}}{\partial \theta} = \frac{\partial \mathbf{p}_0}{\partial \theta} + \zeta \frac{\partial \mathbf{n}_0}{\partial \theta} \\ \mathbf{g}_z &= \frac{\partial \mathbf{p}}{\partial z} = \frac{\partial \mathbf{p}_0}{\partial z} + \zeta \frac{\partial \mathbf{n}_0}{\partial z} \\ \mathbf{g}_\zeta &= \frac{\partial \mathbf{p}}{\partial \zeta} = \mathbf{n}_0(\theta, z)\end{aligned} \tag{3.8}$$

If we develop Eq.[3.8], we find

$$\mathbf{g}_\theta = \varphi_\theta \mathbf{i}_\theta(\theta) \tag{3.9}$$

$$\mathbf{g}_z = \varphi_z(\rho'(z)\mathbf{i}_r(\theta) + \mathbf{i}_z) \tag{3.10}$$

$$\mathbf{g}_\zeta = \frac{-\rho'(z)\mathbf{i}_z + \mathbf{i}_r(\theta)}{\sqrt{1 + \rho'^2(z)}} \tag{3.11}$$

where

$$\begin{aligned}\varphi_\theta &= \left(\rho(z) + \frac{\zeta}{\sqrt{1 + \rho'^2(z)}}\right) \\ \varphi_z &= \left(1 - \frac{\zeta \rho''(z)}{(1 + \rho'^2(z))^{3/2}}\right)\end{aligned} \tag{3.12}$$

Therefore $g$ can be calculated as

$$g = \varphi_\theta \varphi_z \sqrt{1 + \rho'^2(z)} \tag{3.13}$$

If we substitute the expressions of the tangent vectors (Eq.[3.9, 3.10, 3.11]) in the relative gradients (Eq.[3.7]), we obtain

$$\begin{aligned}\boldsymbol{\nabla}_{\mathbf{p}}\theta &= \frac{\mathbf{i}_\theta(\theta)}{\varphi_\theta}\\ \boldsymbol{\nabla}_{\mathbf{p}}z &= \frac{\rho'(z)\mathbf{i}_r(\theta)+\mathbf{i}_z}{\varphi_z(1+\rho'^2(z))}\\ \boldsymbol{\nabla}_{\mathbf{p}}\zeta &= \mathbf{n}_0(\theta,z)\end{aligned} \tag{3.14}$$

The parametrical description of the geometry of the embryo is one of the major advantage of our model, since it allows having the precise analytical expressions of the intermediate position $\bar{\mathbf{x}}$, which are therefore proper to each event and user defined, given the dependence on the elementary forces introduced. The influence of the geometry will be discussed later on in this chapter; we are now going to analyze the different morphogenetic movements.

## 3.2 Ventral furrow invagination and cephalic furrow formation

Ventral furrow invagination and cephalic furrow formation take place simultaneously during embryogenesis and are very similar since triggered by almost the same mechanical constraints. Both the morphogenetic movements can be considered as orthogonal invaginations of the mesoderm (Sec. 1.2.2); in fact invagination occurs along a line rather than at a single point. A trough forms (Fig. 1.2), the axis of which is parallel to the original surface, thus at right angles with respect to the direction of invagination (Davies [2005]).

*Figure 3.2:* Cross sections of the embryo showing the successive phases of ventral furrow invagination (Leptin [1999]). The different colours mark the regions or the cells where invagination occurs.

Ventral furrow invagination proceeds by infolding of a line of epithelium into the yolk, forming a cavity, the lips of which then fuse and separate from their parent epithelium. The cells in the ventral region of the embryo show a strong expression of actin/myosin filaments and contraction of such filaments leads to the constriction from the apical to the basal end of each cell and therefore to the bending of the basal surface inward. This curving is localized at specific hinge points and can generate convex or concave curvature depending on where it takes place (Fig. 1.3). A particular aspect of the hinge points is that cells within them become wedged: at the median hinge point they are apically constricted while basally at the dorso-lateral hinge point Davies [2005].

The apical constriction and the apico-basal elongation have been individuated as active processes responsible of the invagination of the embryonic tissues (Sec. 1.2.3), thus both of them have been implemented for our simulation.

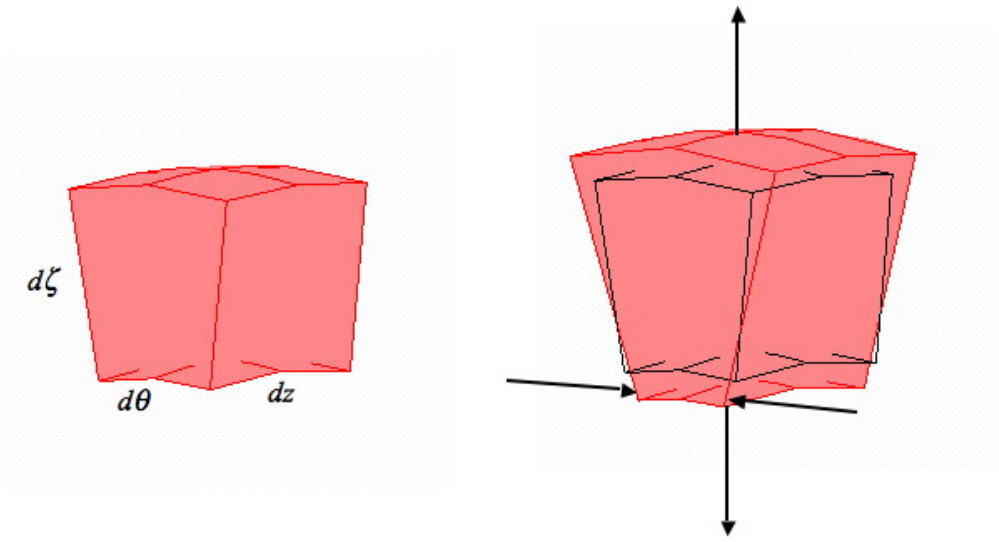


*Figure 3.3:* On the left, a cell of the mesoderm at the reference configuration. On the right, the new shape once the apical constriction and the apico-basal elongation have been applied.

The two active forces are applied on a restricted area of the ventral region of the embryo; this region covers about 70% of the total length of the embryo along the anterior-posterior axis and about 15% of the transverse section. The intermediate position $\bar{\mathbf{x}}(\theta, z, \zeta)$ corresponding to these two deformations combined (Fig. 3.3), can

be written as follows

$$\bar{\mathbf{x}}(\theta, z, \zeta) = \mathbf{p}_0(\tilde{\theta}, z) + \left(1 + \alpha^{abe}(t)\right) \zeta \mathbf{n}_0(\tilde{\theta}, z) \tag{3.15}$$

where $\alpha^{abe}(t)$ is the amplitude of the apico-basal elongation and

$$\tilde{\theta} = \theta + \alpha^{ac}(t) \frac{2\zeta}{h} m(\theta) \tag{3.16}$$

is the deformation angle depending on $\alpha^{ac}(t)$, the amplitude of the apical constriction; $h$ is the thickness of the mesoderm (Fig. 3.1). $m(\theta)$ is a periodic function, normalized between $-1$ and 1, that mimics the material cells themselves by which the deformation region is subdivided (Fig. 3.4).

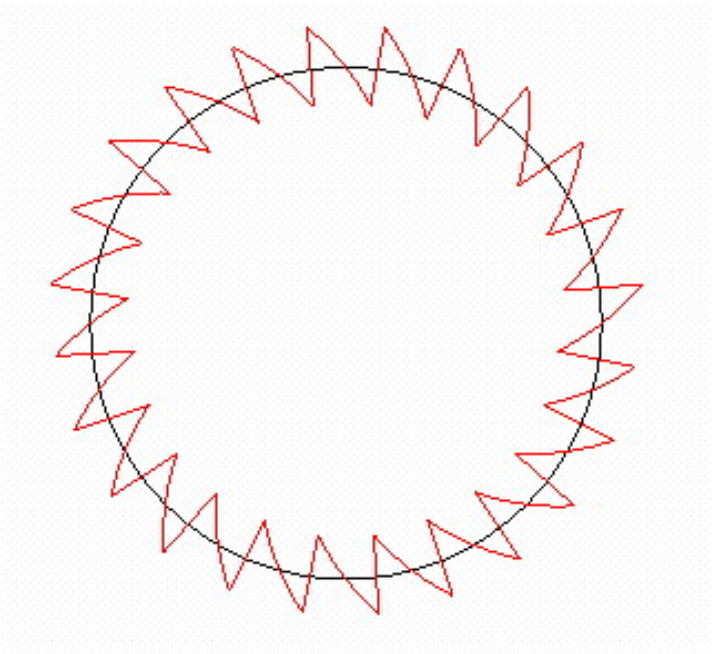

*Figure 3.4:* The trend of the periodic function $m(\theta)$ along a circular section. It allows to have the same deformation along the section of the active region where ventral furrow invagination takes place. For this specific image and for sake of simplicity in the representation, the active region covers all the circular section, while for the case of the embryo it is restrained to a smaller domain. The same function is used for the cephalic furrow simulation ($m(z)$).

Such function is expressed as

$$m(\theta) = 2\left(\frac{\theta}{\theta_{cell}} - \frac{1}{2} - round\left(\frac{\theta}{\theta_{cell}} - \frac{1}{2}\right)\right) \tag{3.17}$$

with $\theta_{cell}$ corresponding to the dimensions of a material cell along the section of the embryo and *round* being the classical step function, which gives the integer number of $\frac{\theta}{\theta_{cell}}$. The introduction of this periodic function has been necessary in order to have the same deformation around the mesoderm cross section where $\theta$ increases.

The deformation amplitudes $\alpha^{abe}(t)$ and $\alpha^{ac}(t)$ are defined as

$$\begin{aligned} \alpha^{abe}(t) &= \alpha_{abe} \cdot t \\ \alpha^{ac}(t) &= \alpha_{ac} \cdot t \end{aligned} \tag{3.18}$$

with $\alpha_{abe}$ and $\alpha_{ac}$ constants that are adjusted in order to assure at the same time the right properties of convergence and consistent final configurations. $t$ is the evolution parameter, which varies between $t^i_{min}$ and $t^i_{MAX}$; here the superscript $i$ indicates the movement considered, since the minimal and the maximal values of $t$ vary according to the simulated event.

Similar equations can be derived for the cephalic furrow, shaped by two parallel strips of cells undergoing an inward flexion movement. Given the different axis with respect to which the invagination takes place, this time the active deformation occurs along the $z$ direction (Fig. 3.5), therefore the intermediate position $\bar{\mathbf{x}}(\theta, z, \zeta)$ of a generic point can be written as follows

$$\bar{\mathbf{x}}(\theta, z, \zeta) = \mathbf{p}_0(\theta, \tilde{z}) + \zeta\ \mathbf{n}_0(\theta, \tilde{z}) \tag{3.19}$$

with

$$\tilde{z} = z + \alpha^{ceph}(t)\frac{2\zeta}{h}m(z) \tag{3.20}$$

where $\alpha^{ceph}(t)$ is the amplitude of the deformation (here only apical constriction has been introduced), defined as $\alpha^{ceph}(t) = \alpha_{ceph} \cdot t$, with $\alpha_{ceph}$ a suitable constant. $m(z)$ is again a periodic function as defined in Eq.[3.17], depending this time on $z$ et $z_{cell}$ , which represents the cell dimensions in the $z$ direction.

Finally, $\mathbf{F}^i_a$ can be computed for both cases from Eq.[3.6] in the curvilinear coordinates system fitted here for the ellipsoidal idealized geometry of the embryo.

Thus we obtain respectively for the ventral furrow

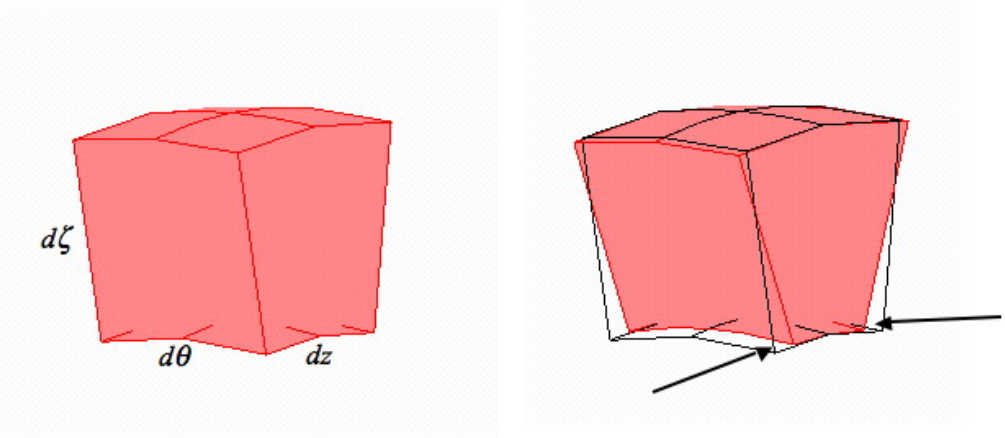


*Figure 3.5:* Apical constriction along the anterior-posterior axis for a cell during the cephalic furrow formation.

$$\begin{aligned}\mathbf{F}_a^{VFI} =& \frac{\left[1+\alpha^{ac}(t)\frac{2\zeta}{h}m'(\theta)\right]\tilde{\varphi}_\theta^{VFI}}{\varphi_\theta}\mathbf{i}_\theta(\tilde{\theta})\otimes\mathbf{i}_\theta(\theta)\\ &+\frac{(\rho'(z)\mathbf{i}_r(\tilde{\theta})+\mathbf{i}_z)\tilde{\varphi}_z^{VFI}}{(1+\rho'^2(z))\varphi_z}\otimes(\rho'(z)\mathbf{i}_r(\theta)+\mathbf{i}_z)\\ &+\left[\frac{2\alpha^{ac}(t)}{h}m(\theta)\tilde{\varphi}_\theta^{VFI}\mathbf{i}_\theta(\tilde{\theta})+(1+\alpha^{abe}(t))\mathbf{n}_0(\tilde{\theta},z)\right]\otimes\mathbf{n}_0(\theta,z)\end{aligned} \tag{3.21}$$

where $\varphi_\theta$ and $\varphi_z$ are the same as defined in Eq.[3.12], while

$$\begin{aligned}\tilde{\varphi_\theta}^{VFI} &= \left[\rho(z)+\frac{(1+\alpha^{abe}(t))\zeta}{\sqrt{1+\rho'^2(z)}}\right]\\ \tilde{\varphi_z}^{VFI} &= \left[1-\frac{(1+\alpha^{abe}(t))\zeta\,\rho''(z)}{(1+\rho'^2(z))^{3/2}}\right]\end{aligned} \tag{3.22}$$

If we analyze the previous expressions we can notice that the term $(1+\rho'^2(z))$ gives the curvilinear abscissa along the embryo. At the dorsal and ventral regions we have $\rho'(z)=0$, while at the anterior and posterior poles $\rho'(z)=\infty$, therefore the deformation determined by $\alpha^i(t)$ is whether inhibited or sharpened. On the other hand $\rho''(z)$ provides the curvature of the embryo which highly affects the apical

constriction. Actually the greater the curvature, the more evident the effects of the constriction. Therefore it would be interesting to perform a sensibility analysis in order to evaluate the influence of the curvature on the final configuration. This aspect has been partly argued by testing different embryo geometries that take into account some peculiar characteristics, as amply described in Sec. 3.11.

For the cephalic furrow the active deformation gradient $\mathbf{F}_a^{CF}$ is

$$\begin{aligned}\mathbf{F}_a^{CF} =& \frac{\tilde{\varphi}_\theta^{CF}}{\varphi_\theta}\mathbf{i}_\theta(\theta)\otimes\mathbf{i}_\theta(\theta) \\ &+ \frac{\left[1+\alpha^{ceph}(t)\frac{2\zeta}{h}m'(z)\right]\tilde{\varphi}_z^{CF}}{\varphi_z(1+\rho'^2(z))}(\rho'(\tilde{z})\mathbf{i}_r(\theta)+\mathbf{i}_z)\otimes(\rho'(z)\mathbf{i}_r(\theta)+\mathbf{i}_z) \\ &+ \left\{\left[\frac{2\alpha^{ceph}(t)}{h}m(z)\tilde{\varphi}_z^{CF}(\rho'(\tilde{z})\mathbf{i}_r(\theta)+\mathbf{i}_z)\right]+\mathbf{n}_0(\theta,\tilde{z})\right\}\otimes\mathbf{n}_0(\theta,z)\end{aligned} \tag{3.23}$$

where

$$\begin{aligned}\tilde{\varphi}_\theta^{CF} &= \rho(\tilde{z}) + \frac{\zeta}{\sqrt{1+\rho'^2(\tilde{z})}} \\ \tilde{\varphi}_z^{CF} &= 1 - \frac{\zeta\rho''(\tilde{z})}{(1+\rho'^2)^{3/2}}\end{aligned} \tag{3.24}$$

As mentioned before, each normalized function $\mathbf{F}_a^i$ is applied on a restricted region of the embryo according to the morphogenetic movement considered; this is possible using a regularized Heaviside function (see Sec. 2.5) that allows having $\mathbf{F}_a^i$ as computed above where the deformation takes place and $\mathbf{F}_a^i = \mathbf{I}$ elsewhere. The transition between the two domains, the active and the passive one, is smoothed within an interval equal to the dimensions of one single cell.

## 3.3 Germ band extension

Germ band extension is triggered by a convergent-extension movement of the cells. This movement, as well as related mass tissue movements, may be a passive response to some forces generated elsewhere in the embryo or it may be active, force-producing process (Keller et al. [2000]). Actually during GBE tissues change their morphology due to interactions occurring between cells rather than interactions with external boundaries. Since the convergent-extension movement takes place without cell growth and the appropriate changes in cells shape, probably rearrangement and intercalation of cells have to be considered (Fig. 1.14) (Waddington [1940]). Hartenstein and Campos-Ortega (Campos-Ortega and Hartenstein [1985]) have examined embryos undergoing GBE and they have observed that in the ventral ectoderm much

of the increase in length of the germ band occurs in absence of cell division or change in cell shape, instead the number of cells increases along the anterior-posterior axis and decreases along the dorsal-ventral axis. Thus they deduced that germ band extension has to be coupled with cells intercalation or cells rearrangement. Intercalation seems to be extremely directional since cells intercalate for most of the time between dorsal and ventral neighbours and only rarely with anterior and posterior neighbours (Irvine and Wieschaus [1994]).

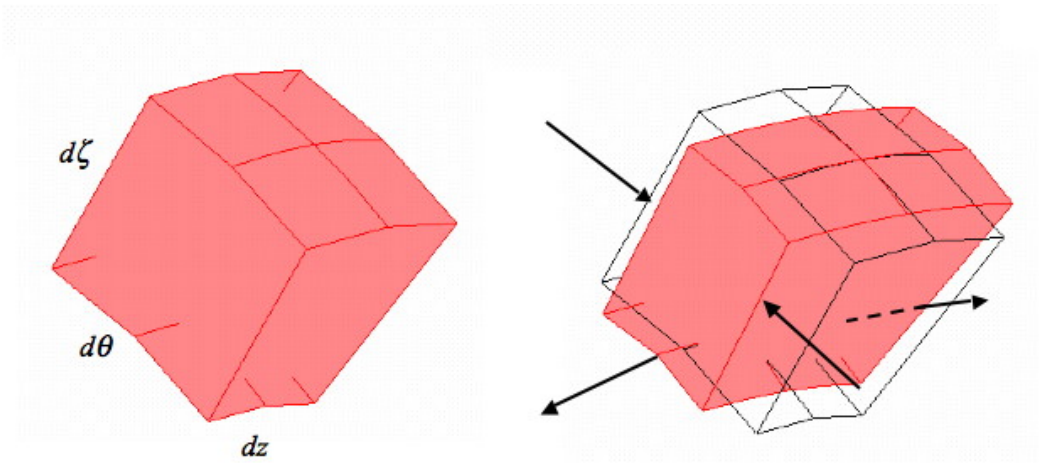


*Figure 3.6:* Convergent-extension movement of a cell during the extension of the germ band.

Let $\mathbf{p}_0(\theta, z)$ be the initial position of a point on the middle surface of the mesoderm as defined in Eq.[3.2] and $\mathbf{p}(\theta, z, \zeta)$ the position of a generic point through the thickness of the mesoderm (Eq.[3.4]). Since the cells are not modelled here, the intercalation phenomenon can not be exactly reproduced, therefore we propose a membrane convergent-extension movement applied in the region of the germ band, so that the intermediate position $\bar{\mathbf{x}}(\theta, z, \zeta)$ after deformation comes to be

$$\bar{\mathbf{x}}(\theta, z, \zeta) = \mathbf{p}_0(\tilde{\theta}, \tilde{z}) + \zeta \mathbf{n}_0(\tilde{\theta}, \tilde{z}) \tag{3.25}$$

where this time $\tilde{\theta}$ and $\tilde{z}$ are equal to

$$\begin{aligned} \tilde{\theta} &= (1 + \alpha_\theta^{GBE}(t))\theta \\ \tilde{z} &= (1 + \alpha_z^{GBE}(t))z \end{aligned} \tag{3.26}$$

with $\alpha_\theta^{GBE}(t)$ and $\alpha_z^{GBE}(t)$ the amplitudes respectively of the shortening from the dorsal to the ventral region of the embryo and of the lengthening along the anterior-posterior axis. They are expressed, as similarly as in Eq.[3.18], as

$$\begin{aligned} \alpha_\theta^{GBE}(t) &= \alpha_\theta \cdot t \\ \alpha_z^{GBE}(t) &= \alpha_z \cdot t \end{aligned} \tag{3.27}$$

with $\alpha_\theta$ and $\alpha_z$ specific constants. It has to be noticed here that for the formulation of the germ band extension we do not introduce the periodic function neither for the deformation of $\tilde{\theta}$ nor for the one of $\tilde{z}$. Actually, for the ventral and the cephalic furrows, the modification of the active region is obtained through the precise description of the change in shape of each single cell, therefore the need of having for each element the same amplitude of deformation. In this specific case of cells intercalation instead, the strain of the active region, which exactly corresponds to the germ band, is macroscopically obtained without reference to the individual cells.

$\mathbf{F}_a^i$ is here again computed from Eq.[3.6] and it is applied on the associated area of deformation; its final expression is

$$\begin{aligned} \mathbf{F}_a^{GBE} =& \frac{(1+\alpha_\theta^{GBE}(t))\tilde{\varphi_\theta}^{GBE}}{\varphi_\theta} \mathbf{i}_\theta(\tilde{\theta}) \otimes \mathbf{i}_\theta(\theta) \\ &+ \frac{(1+\alpha_z^{GBE}(t))\tilde{\varphi}_z^{GBE}}{(1+\rho'^2(z))\varphi_z} (\rho'(\tilde{z})\mathbf{i}_r(\tilde{\theta}) + \mathbf{i}_z)) \otimes (\rho'(z)\mathbf{i}_r(\theta) + \mathbf{i}_z) \\ &+ \mathbf{n}_0(\tilde{\theta}, \tilde{z}) \otimes \mathbf{n}_0(\theta, z) \end{aligned} \tag{3.28}$$

with

$$\begin{aligned} \tilde{\varphi}_\theta^{GBE} &= \rho(\tilde{z}) + \frac{\zeta}{\sqrt{1+\rho'^2(\tilde{z})}} \\ \tilde{\varphi}_z^{GBE} &= 1 - \frac{\zeta\rho''(\tilde{z})}{(1+\rho'^2(z))^{3/2}} \end{aligned} \tag{3.29}$$

## 3.4 Results

With the present work, we have been able to reproduce three morphogenetic movements: the ventral furrow invagination, the cephalic furrow formation and the germ band extension. In this section we show the results for each individual simulation; the key aspects are presented together with the limits of the model and the improvements to be made, with particular emphasis on some parameters that may affect the final configurations and have to be taken into account. The results are interesting

because in good agreement with the experimental observations, and innovative since never before, to our knowledge, a single FE model has allowed to reproduce more than one morphogenetic movement (see Chapter 1). Furthermore, the analytical description of the active forces on the cells consents to have different expressions for the active deformation gradients $\mathbf{F}_a^i$ that are therefore easy to modify and can be coupled together in order to have a concurrent simulation of two or three movements at the time (see Chapter 4).

In this study, for sake of simplicity and because of the lack in information regarding the mechanical characteristics of the vitelline membrane and the yolk, only the mesoderm is modelled. It is represented as an ellipsoid with the dimensions of a real *Drosophila* embryo: $500\mu m$ in length, a cross-section diameter of $150\mu m$ and a thickness of $15\mu m$ (Fig. 3.7). When observing the real embryo, it is possible to notice that the curvature is not the same all long the contour and there is not a perfect symmetry with respect to the vertical axis; actually the posterior pole is more rounded than the anterior pole. Therefore the ellipsoid might not be the best geometrical representation; conscious of this drawback, we have also tested other sophisticated and accurate parametrical descriptions that allow us to take into account such aspects (Sec. 3.11). As mentioned in Sec. 2.3, a Saint-Venant model is used to describe the mesoderm, thus only two parameters have to be chosen. The Young's modulus $E$ is set at $100Pa$ according to literature (Wiebe and Brodland [2005]). The Poisson's coefficient $\nu$ is fixed at 0.45 which gives a coefficient of compressibility for the mesoderm $k_m = \frac{E}{3(1-2\nu)} = 333Pa$. If the choice of the mechanical characteristics of the mesoderm may appear here approximative, we want to remark that, for a biological system, and a fortiori for a micro-structure like the embryo, it is not always evident to detect all the parameters.

For the simulations, we have developed our own weak form and we have opted for a standard FE discretization, usually Lagrange elements of order two. The COMSOL Multiphysics software (v 3.4; Comsol, Inc.) is used, a code that permits to manipulate the governing equations. All the amplitudes $\alpha^i(t)$ depend on an incremental parameter $t$, which varies between a minimal value $t^i_{min}$, usually equal to 0, and a maximal value $t^i_{MAX}$, which changes according to the morphogenetic movement analyzed. Furthermore, the elementary forces are applied on the relative active deformation region. Such region has almost the same dimensions of the active region observed in reality, where each event takes place, and is obtained by a regularized Heaviside function. It consists of a $C^1$ differentiable function whose value is 0 for a negative argument and 1 for a positive argument and it varies between these two values over a length fixed by us equal to one single cell ($\cong 15\mu m$). This means that, for our specific case, we are going to have $\mathbf{F}_a^i$ as computed earlier for each movement where the deformation occurs, while elsewhere we will find $\mathbf{F}_a^i = \mathbf{I}$.

Although the vitelline membrane and the yolk have not been physically represented and therefore not meshed here, both the boundary conditions have been implemented since the absence of one or both of them leads to final configurations

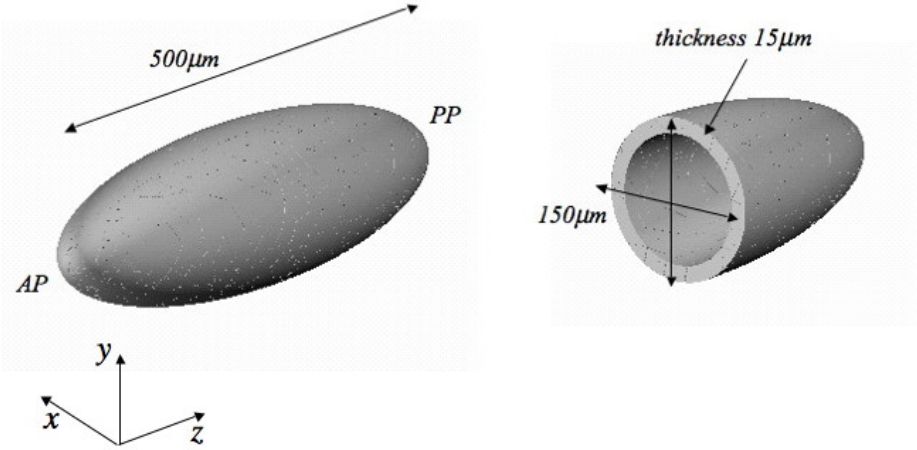


*Figure 3.7:* The geometry of the embryo (AP: anterior pole, PP: posterior pole).

that do not correspond to what has been experimentally observed (Sec. 2.7). As presented in Sec. 2.7.1.1, for the external contact with the vitelline membrane, the values of $t_c$ and $k_c$ have been fixed at $1Pa$ and $1 \cdot 10^8$ respectively. For what concerns instead the yolk pressure exerted on the internal surface of the mesoderm, we have chosen the initial pressure $p_{y_0} = 1 \cdot 10^{-6} Pa$ and the coefficient of compressibility $k_y = 1Pa$, which is much smaller than the coefficient of compressibility $k_m$ previously found for the mesoderm. We assume here in fact a significant compressibility of the yolk to consent the complete internalization of the cells that otherwise would not be possible, unless part of the fluid overflows during the invagination.

As mentioned in Sec. 2.8, the finite elements modelling is used for our simulations. The mesh employed for the ellipsoid representing the embryo is constituted by 4947 tetrahedral elements (Fig. 3.8) which implies 28314 degrees of freedom.

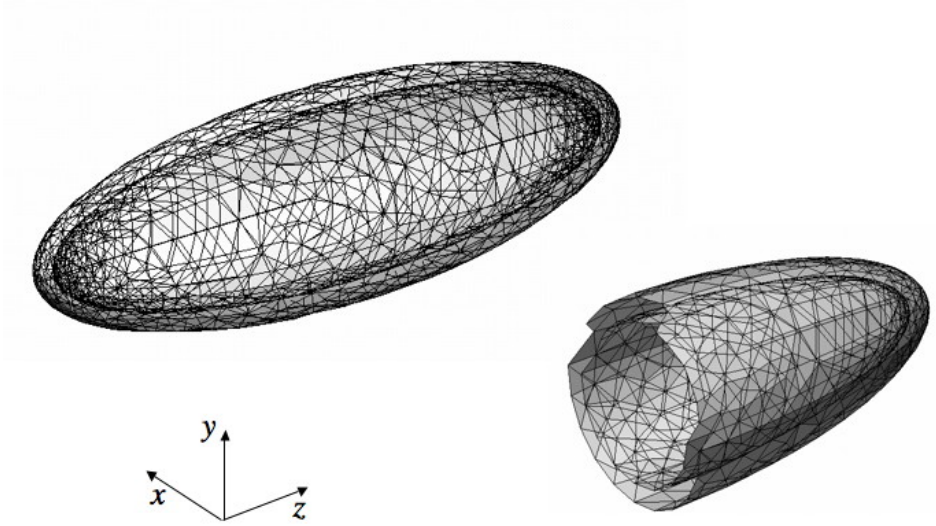


*Figure 3.8:* The mesh employed for the geometry of the embryo. On the left a perspective view and on the right a cross sectional view.

## 3.5 Ventral furrow invagination

For the ventral furrow invagination we start by implementing only apical constriction so that $\alpha^{abe}(t) = 0$ and Eq. [3.15] becomes

$$\bar{\mathbf{x}}(\theta, z, \zeta) = \mathbf{p}_0(\tilde{\theta}, z) + \zeta \mathbf{n}_0(\tilde{\theta}, z) \tag{3.30}$$

The active deformation gradient $\mathbf{F}_a^{VFI}$ is then

$$\begin{aligned} \mathbf{F}_a^{VFI} = & \left[1 + \alpha^{ac}(t)\frac{2\zeta}{h}m'(\theta)\right]\mathbf{i}_\theta(\tilde{\theta}) \otimes \mathbf{i}_\theta(\theta) \\ & + \frac{\left[\rho'(z)\mathbf{i}_r(\tilde{\theta}) + \mathbf{i}_z\right]}{(1+\rho'^2(z))} \otimes \left[\rho'(z)\mathbf{i}_r(\theta) + \mathbf{i}_z\right] \\ & + \left[\frac{2\alpha^{ac}(t)}{h}m(\theta)\varphi_\theta \mathbf{i}_\theta(\tilde{\theta}) + \mathbf{n}_0(\tilde{\theta}, z)\right] \otimes \mathbf{n}_0(\theta, z) \end{aligned} \tag{3.31}$$

As we can deduce from Eq.[3.31], the final result for this simulation may be affected by several parameters such as the dimensions of the material cells and the amplitude of the active deformation region. In the next sections, we will focus on

the analysis of their influence on the final configuration, but for a first series of tests we have decided to fix them in order to have some preliminary results. Therefore in addition to $\alpha^{abe}(t) = 0$, we set the amplitude of a single cell $\theta_{cell} = \pi/12$.

The deformation region where the ventral furrow invagination takes place is characterized by:

- the length along the anterior-posterior axis, which remains constant and covers about 70% (about $350\mu m$) of the entire length of the embryo;
- the amplitude $\theta$ along the cross section of the embryo, that is chosen for this first specific case equal to $50°$, which means about $60\mu m$ of the total circumference of the embryo (Fig. 3.9).

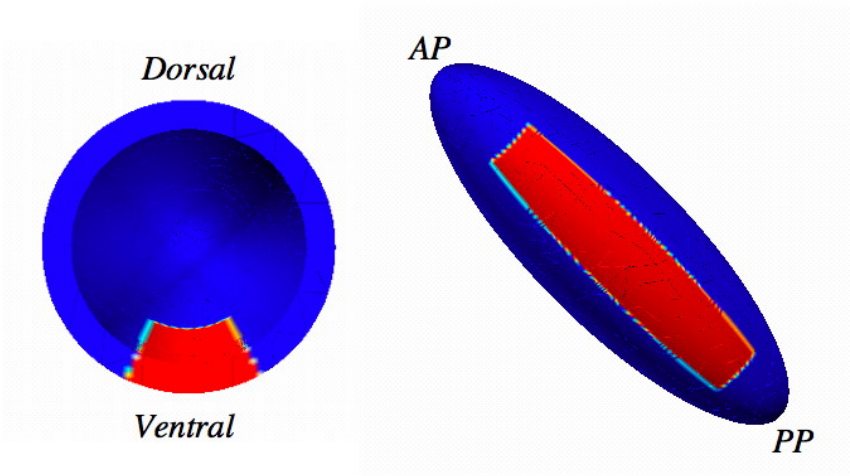


*Figure 3.9:* In red the active deformation region for the ventral furrow invagination (AP: anterior pole, PP: posterior pole). On the left a cross section of the embryo, on the right a ventral view.

If we assume that the dimensions of an embryonic cell are approximatively $15\mu m$ along the apico-basal axis (equal to the thickness of the mesoderm since there is a single layer of cells) and about $10\mu m$ along the anterior-posterior axis and the cross-section, we can deduce that the active region involves about 210 cells. Once the ventral furrow has formed, we have almost 560 cells that have completely internalized into the yolk, which is not so different from what it has been experimentally observed (Sec. 1.2.3). It has to be said that the qualitative dimensions chosen here for a single cell have been deduced from images of real embryos and have to be considered then as a reasonable average of multiple cases. One may notice a slight disagreement

with respect to some parameters implemented for our simulations. For instance, the value of $\theta_{cell}$ provides a cross sectional length of a single cell approximatively equal to $15\mu m$, which does not match with the dimension hypothezised above. This is due to the fact that often the choice of the numerical variables have been made to simultaneously assure the right properties of convergence and final consistent results.

For this specific simulation $t$ goes from $t_{min}^{VFI} = 0$ to $t_{MAX}^{VFI} = 0.003$. If we consider the cell dimensions assumed above, the maximal value of $\alpha^{ac}(t) = \alpha_{ac} \cdot t_{MAX}^{VFI}$, where $\alpha_{ac}$ is a constant, provides a maximal apical constriction for a single cell of $\cong 7\mu m$ and therefore an almost equal basal elongation, according to the embryo curvature. Such maximal constriction corresponds to the maximal active deformation, calculated by the analytical expression of the intermediate position $\bar{\mathbf{x}}$ of any point of the mesoderm (Eq.[3.15]), and it would be observable if the cells were totally free (see Sec. 2.1). Here instead, it does not coincide with the final deformation which is the composition of the active and the passive contributions and thus larger or smaller according to the initial position of a cell.

In Fig. 3.10 we see the successive phases of ventral furrow invagination for our simulation. If we compare our results to the real invagination (Fig. 1.4), we notice that in our case the mesoderm narrows much more than in reality, which leads to a greater self-contact between the two strips of the mesoderm. So far we did not analyzed this phenomenon from a theoretical point of view, even if this type of contact could engender repulsive forces and affects the global behaviour of the system. Nevertheless, the vertical symmetry of the embryo is not broken so that the self-contact is naturally taken into account. Additionally, throughout the simulations, we have observed how some parameters may favor or inhibit such phenomenon.

The last image (Fig. 3.10d, cross section) represents the material cells that are obtained here by a cell marker (Heaviside function) transported by the deformation movement. Each white sector defines a single cell that undergoes the elementary deformations, while the black zones correspond to the transition between the two values of the smooth step function; the more the mesoderm invaginates, the more the apical constriction is evident, particularly at the peak of the furrow, where the apical surfaces are almost completely shrink. Additionally the constriction switches from apical to basal according to the mesoderm wedging; specifically, as already mentioned in Sec. 3.2, they are apically constricted at the medio-lateral hinge point, while basally at the dorso-lateral hinge points. It has to be noticed that, if at the medio-lateral hinge point, which is included in the active region, the deformation is triggered by $\mathbf{F}_a$, at the dorso-lateral hinge points the basal constriction is due to the passive reaction of the tissues $\mathbf{F}_m$.

These preliminary results confirm what has been pointed out by biologists (see Sec. 1.2.3). In fact we find that, introducing only the apical constriction as active elementary deformation on the cells, the ventral furrow invagination still takes place. This means that apical constriction is effectively an active force acting on the cells,

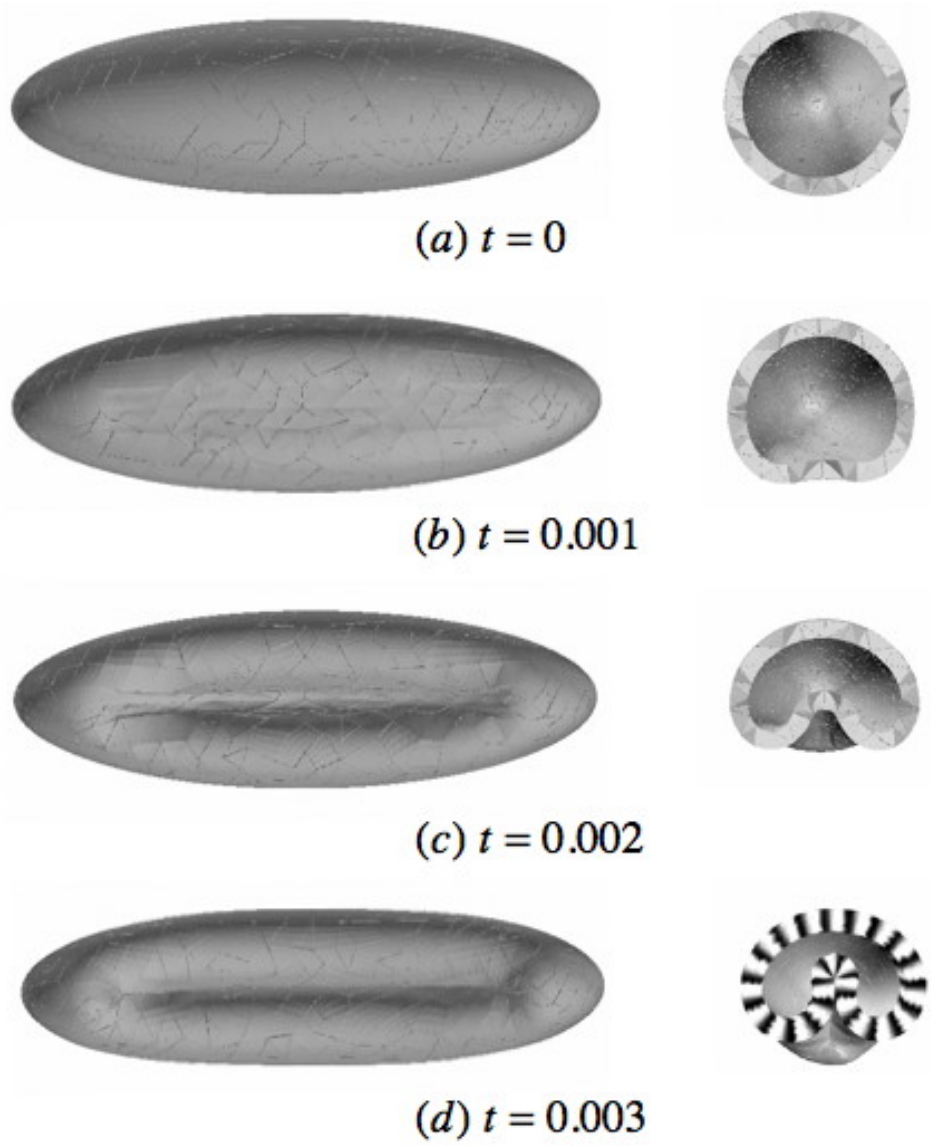


*Figure 3.10:* (a:d) Successive phases of ventral furrow invagination. On the left ventral views, on the right cross sections of the embryo. The cross section at $t_{MAX}^{VFI} = 0.003$ shows the shape changes undergone by the material cells. Each white domain represents a single cell, while the black ones are triggered by the smoothing effect of the classical Heaviside function by which the material cells are obtained.

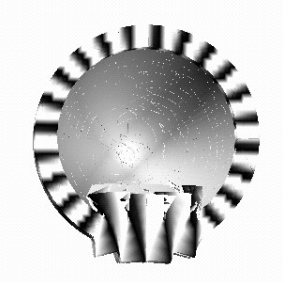

*Figure 3.11:* Intermediary cross sectional view of the embryo. When apical constriction takes place, the cells change their shape, but the deformation does not guarantee the integrity and the continuity of the system; therefore a superposition of the volumes occurs.

but furthermore we could affirm that it is also the principal deformation determining the narrowing of the mesoderm into the yolk as already observed by Pouille (Pouille and Farge [2008]) in his numerical simulations. This conclusion is very important from a mechanical point of view since it allows to consider any other deformation as a passive response of the cells to the apical constriction. Actually when apical constriction takes place, the cells change their shape, but such modification may not be compatible with the fact that they are in contact with one another; specifically there might be a superposition of the volumes. This is evident from Fig. 3.11 where we can notice the constriction at the apical surface and the widening of the basal end, which induce a dilatation of the cells with a consequent material overlapping. The cells are then lead up to find a new configuration assuring the continuity and the integrity of the system, thus the successive passive deformation occurs.

### 3.5.1 Influence of the size of the active deformation region

As previously described, the active deformation region where the ventral furrow invagination takes place, is determined by its length along the anterior-posterior axis and the amplitude $\theta$ along the cross section. We have decided to not change the size in the horizontal direction, but only to let vary the angle $\theta$; we chose therefore three different values, $\theta = 50°, 60°$and $90°$ (Fig. 3.12). When changing the amplitude of the active zone, the quantity of cells involved changes too; therefore we have a number of cells comprised between 210 and 350 at the initial configuration, which implies that, once the furrow has formed, the total final number of cells that have internalized is comprised between 560 and 700.

In Fig. 3.13 we show the results for two series of simulations

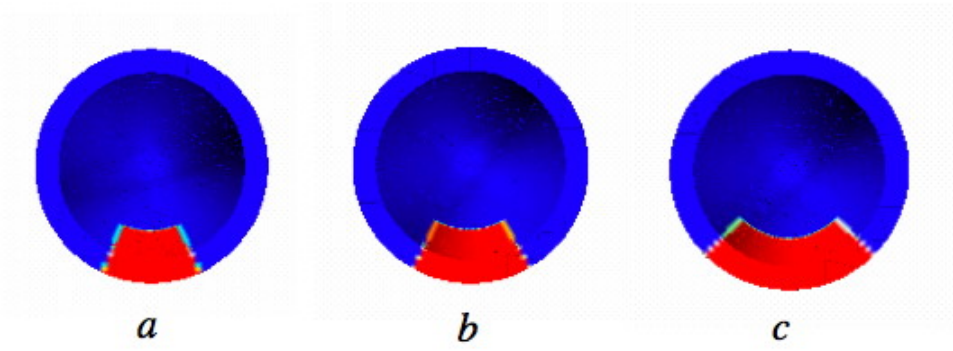


*Figure 3.12:* Variation of the active deformation region for VFI. (a) $\theta = 50°$ (b) $\theta = 60°$ (c) $\theta = 90°$.

- images (a:c) represent the invagination with $\theta_{cell} = \pi/10$ and $\theta = 50°(a)$, $60°(b)$ and $90°(c)$
- for images (d:f), $\theta_{cell}$ is set to $\pi/12$ and again $\theta$ varies from $50°(a)$, $60°(e)$ and $90°(f)$

When modifying the dimensions of the active region of deformation, we expected that the greater $\theta$, the higher the invagination of the mesoderm into the yolk, but actually this is really evident only for the case of $\theta = 90°$ (Fig. 3.13c) and even more for the case with $\theta_{cell} = \pi/12$ (Fig. 3.13f). On the other hand, we observe that the self-contact decreases when the active region increases, leading to a wider invagination.

### 3.5.2 Influence of the dimensions of the material cells

The next parameter we are going to analyze is $\theta_{cell}$, which determines the dimensions of a single cell by which the mesoderm is divided along the cross section. It has to be said that, for the simulation of the ventral furrow invagination, we have supposed that the cells do not deform along the anterior-posterior axis, which means that their size in the $z$ direction remains constant. Therefore we have only changed the dimensions along $\theta$; specifically, we have tested $\theta_{cell} = \pi/8, \pi/10$ and $\pi/12$. The lesser the value of $\theta_{cell}$, the higher the number of the cells in the domain. Such values for $\theta_{cell}$ may not be very accurate since, observing a real embryo, we can count up to 80 cells along the cross-section at $z = 0$. According to the hypothesis made in Sec. 3.5 concerning the dimensions of a single cell and given the dimensions of the embryo, we find about 42 cells along the section. This theoretical number of cells is still too big compared to the maximal one obtained for our simulations

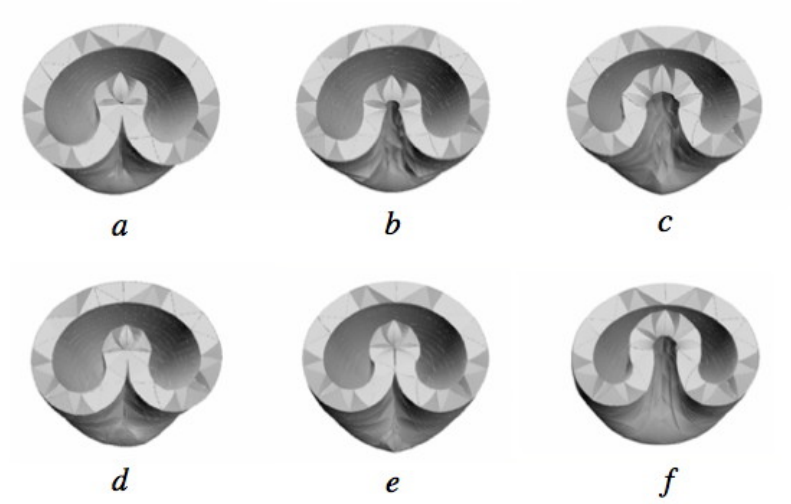


*Figure 3.13:* Influence of the size of the active deformation region on the ventral furrow invagination; cross sections of the embryo at $t^{VFI}_{MAX} = 0.003$. (a:c) Simulations with $\theta_{cell} = \pi/10$ and the amplitude $\theta$ of the region equal to $50°(a)$, $60°(b)$ and $90°(c)$. (d:f) Simulations with $\theta_{cell} = \pi/12$ and again $\theta = 50°(d)$, $60°(e)$ and $90°(f)$.

when $\theta_{cell} = \pi/12$, which provides 24 cells. If we consider that $\theta_{cell}$ corresponds to a group of 3 cells on which the active forces are applied, we obtain a total number of cells along the section equal to 72 which is therefore reasonable compared to reality. This hypothesis allows to optimize the quality of the convergence properties assuring coherent final results.

Fig. 3.14 shows the results obtained for this specific analysis, for which the size of the active deformation region is the same as for the first study, with $\theta = 50°$ (Sec. 3.5). We remark that the more the material cells composing the mesoderm, the more evident and accentuated the self-contact between the mesodermal strips and additionally there is a better continuity at the medio-lateral hinge point.

### 3.5.3 Influence of the apico-basal elongation

The previous tests not only provide a parametric study for the simulation of the ventral furrow invagination, but they also allow us to define the best set of parameters giving the most consistent and similar final configuration compared to reality. Therefore for the next simulations we have fixed the dimensions of the material cells $\theta_{cell} = \pi/12$ and the amplitude of the active region $\theta = 50°$.

When introducing the apico-basal elongation, the intermediate position $\bar{\mathbf{x}}$ is again

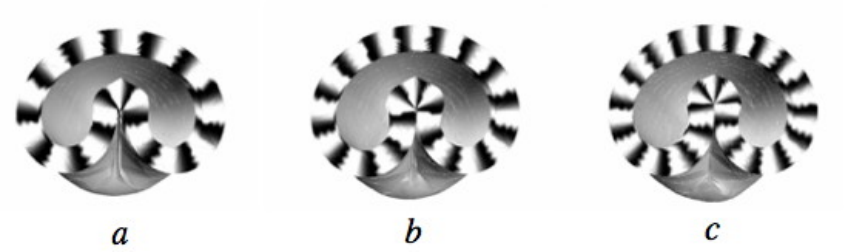


*Figure 3.14:* Influence of the dimensions of the cells. Cross sections of the embryo at $t_{MAX}^{VFI} = 0.003$; the white spots represent a single cell, while the black ones are triggered by the smoothing effect of the classical Heaviside function by which the cells are obtained. The size of the deformation region is still the same ($\theta = 50°$), while $\theta_{cell} = \pi/8\,(a), \pi/10\,(b)$ and $\pi/12\,(c)$.

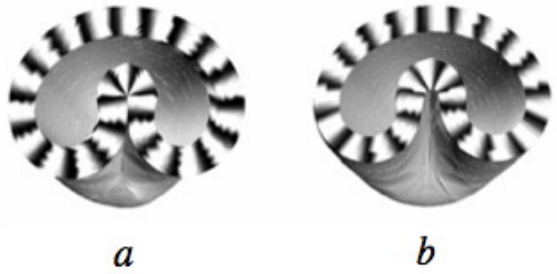


*Figure 3.15:* Influence of the apico-basal elongation on the ventral furrow invagination; cross sections of the embryo at $t_{MAX}^{VFI} = 0.003$. (a) Simulation with only apical constriction implemented (b) Simulation with both the elementary cell deformations taken into account.

the one expressed in Eq.[3.15], so that the parameter $\alpha^{abe}(t)$ defines the elongation of the cells along their apico-basal axis. Considering the $t_{min}^{VFI}$ and $t_{MAX}^{VFI}$ previously indicated (Sec. 3.5), the maximal value for $\alpha^{abe}(t) = \alpha_{abe} \cdot t_{MAX}^{VFI}$, where $\alpha_{abe}$ is a constant, provides a maximal apico-basal elongation equal to $\cong 2 \cdot 10^{-2} \mu m$. As we see in Fig. 3.15b, the presence of this additional elementary deformation does not play a significant role for what concerns the size of the invagination, which is almost the same compared to the simulation where only apical constriction is considered; nevertheless it highly inhibits the self-contact.

## 3.6 Cephalic furrow formation

The formation of the cephalic furrow is induced by a narrowing of the mesoderm along the horizontal axis over the entire cross section of the embryo; this means that the apical constriction, which, given the considerations made in Sec. 3.5, is again the only elementary force introduced, involves a deformation along the $z$ direction (Eq.[3.19]). Compared to the ventral furrow, the simulation of the cephalic furrow would have been more complex if some simplifications would have not been done. Actually the ventral furrow, throughout its formation, maintains a position parallel to the anterior-posterior axis. On the other hand the cephalic furrow starts to form vertically but then, probably triggered by the extension of the germ band, which starts to take place at that moment of gastrulation, it is pushed forward towards the anterior pole and its final position results to be inclined at about 30° with respect to the dorsal-ventral axis of the embryo. Therefore the cells constrict apically in the $z$ direction and additionally they skew, so that their $\theta$ (Eq.[3.19]) changes as the process goes along. Technically this issue could have been handled either by implementing a deformed $\theta$ in the equation of the intermediate position $\bar{\mathbf{x}}$ or by using a Eulerian formulation instead of a Lagrangian one. For the present work we have decided to leave aside the analysis of this peculiar aspect, which is however in progress and probably presented for further studies. To sum up, we have modelled the active deformation region for the cephalic furrow as showed in Fig. 3.16: parallel to the vertical axis of the embryo, at about one third of the total horizontal length, and fixed throughout the simulation.

The simulation starts at $t^{CF}_{min} = 0$ and stops at $t^{CF}_{MAX} = 0.001$; the maximal apical constriction for a single cell in the $z$ direction is obtained when $\alpha^{ceph}(t) = \alpha_{ceph} \cdot t^{CF}_{MAX}$, $\alpha_{ceph}$ being a constant, and is equal to $\cong 5\mu m$. Here again it has to be noticed that the maximal active constriction has been obtained from the intermediate position $\bar{\mathbf{x}}$ (Eq.[3.19]) and therefore does not represent the final observed deformation, which is however the result of the active and the passive contributions. The results are presented in Fig. 3.17. The maximal active deformation leading to the formation of the cephalic furrow is much smaller than the one found for the ventral furrow invagination; this is probably due to the fact that the active region for this specific simulation is thinner, thus a slighter number of cells is involved and also that the amplitude of the invagination is smaller in this case.

Finally we want to point out once more that here again only apical constriction is introduced as elementary deformation of the cells and we still obtain the invagination of the mesoderm giving the formation of the cephalic furrow; our previous conclusion is then reconfirmed.

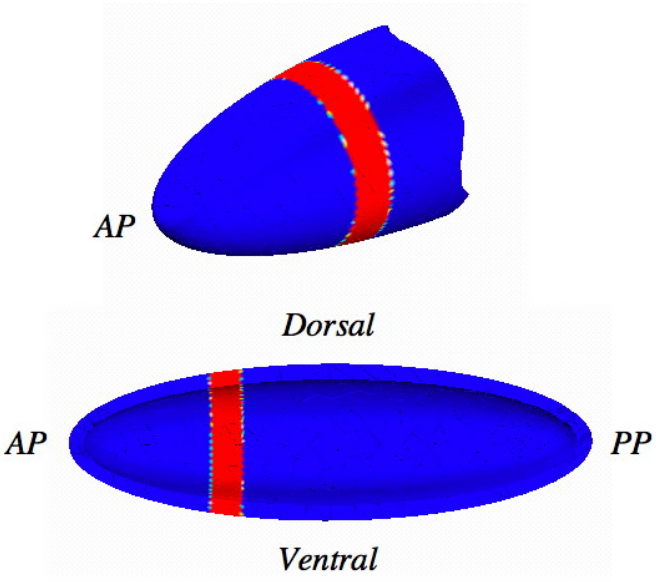


*Figure 3.16:* Perspective (top) and cross sectional (bottom) views of the embryo. In red the active deformation region for cephalic furrow (AP: anterior pole, PP: posterior pole).

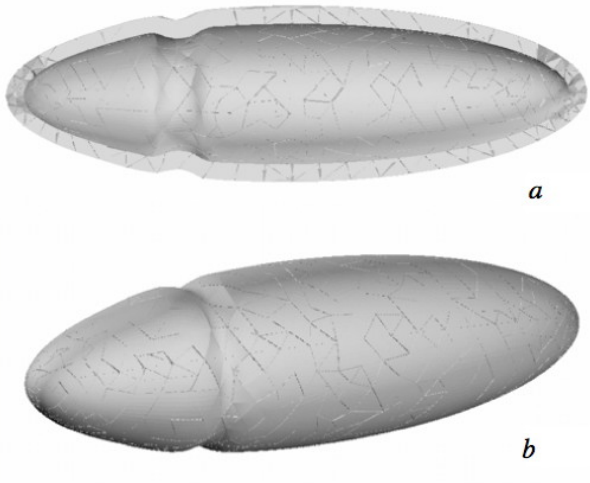


*Figure 3.17:* (a) Cross sectional view of the embryo at the final configuration ($t^{CF}_{MAX} = 0.001$) for the simulation of the cephalic furrow (b) Global view of the embryo.

## 3.7 Germ band extension

The germ band extension has been the first morphogenetic event we have tried to reproduce since the main objective was to compare the numerical results with the experimental ones obtained by Farge and co-workers (Supatto et al. [2005]). They detected the velocity field of an intact embryo during the convergent-extension movement of the cells and they also observed that the extension of the germ band leads to a compression at the anterior pole of the embryo. Such compression induces the expression of the gene *twist*, which normally is only expressed at the ventral region (Brouzés and Farge [2004], Farge [2003]). Biologists have therefore supposed that, if the genes control the mechanical movements of the embryo (see Chapter 1), also the other way round may be possible, which means that morphogenetic events influence and regulate the expression of certain genes within the embryo. This phenomenon is known as mechanotransduction and refers thus to the many mechanisms by which cells convert a mechanical stimulus into chemical activity. We have been able to estimate the induced forces through the embryo when the convergent-extension movement takes place (Sec. 3.9, 3.10); the results are coherent with what has been found by biologists and therefore constitute an important support for further analysis.

In Fig. 3.18 the active deformation region defined for the present simulation is represented in red; it covers approximatively 40% of the entire length of the embryo along the anterior-dorsal axis ($\cong 200\mu m$) and it has an amplitude of about 90° ($\cong 100\mu m$). Therefore, according to the hypothesis made for the dimensions of a single cell (Sec. 3.5), about 200 cells are involved in the convergent-extension movement.

In Eq.[3.25], which supplies the intermediate position $\bar{\mathbf{x}}$ during germ band extension, we indicate with $\alpha_\theta^{GBE}(t)$ and $\alpha_z^{GBE}(t)$ the amplitudes of the convergence and the extension of the cells respectively; their values have been chosen assuming a regular intercalation of the cells. This means that, given the fact that the cells do not divide nor bind together, the initial number of cells involved is the same at the end of the simulation. Therefore, if at the initial configuration ($t_{min}^{GBE} = 0$) we have approximatively 20 cells along the anterior-posterior axis and 10 cells along the dorsal-ventral axis in the active region, at the final configuration ($t_{MAX}^{GBE} = 0.02$), since the germ band has undergone an elongation of about $50\mu m$ and a shortening of $20\mu m$, we find 25 and 8 cells respectively along the anterior-posterior and dorsal-ventral axes. The amplitude of the elongation does not correspond here to the experimental data (Sec. 1.2.7), according to which the germ band almost doubles its length; this is due to the fact that our simulation reproduces only part of the convergent-extension process, so that the mass movement is not fully completed.

The results are shown in Fig. 3.19. It is possible to outline a confined area of the dorso-lateral region of the embryo where the cells converge and shorten; on the side boundary of the area instead, the cells start to elongate and they are involved in whirlpool movements, in particular at the posterior pole.

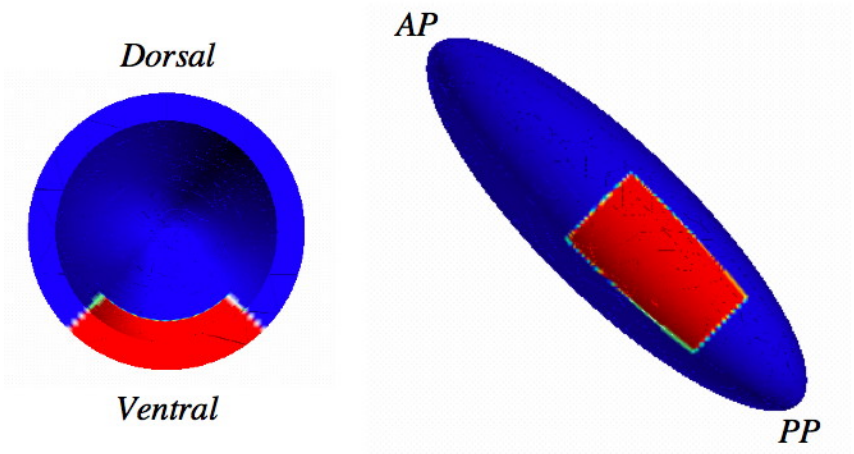


*Figure 3.18:* In red the active deformation region for the germ band extension; cross section (left) and ventral (right) views (AP: anterior pole, PP: posterior pole).

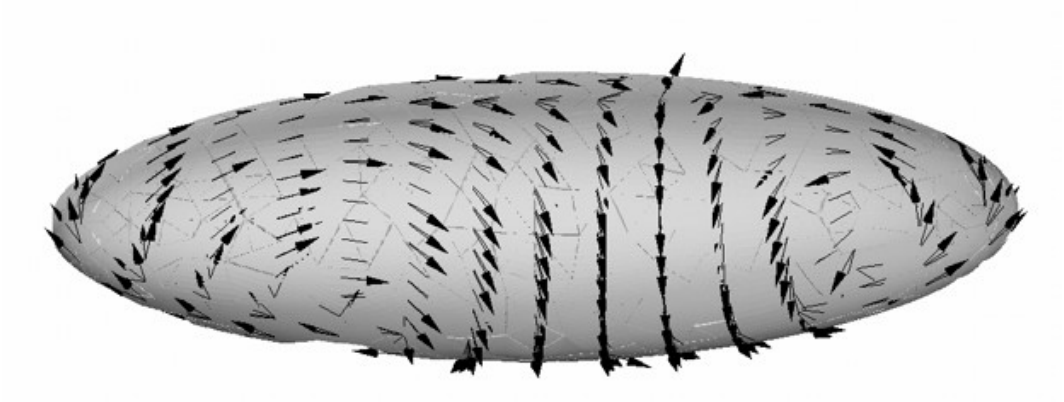

*Figure 3.19:* Frontal view of the embryo for the simulation of the germ band extension ($t^{GBE}_{MAX} = 0.02$). The black arrows represent the displacements.

The constitutive law adopted for the present work does not depend on time, but we have tried, through a calibration, to estimate the velocity by which the tissues deform and we have compared it with experimental data. The germ band extension of a real *Drosophila* embryo takes approximatively $2h$ to complete, with a final elongation of about 2.5 times the initial length. In our simulation, at the initial configuration, the active region covers $200\mu m$, which means that theoretically it

would stretch to $500\mu m$. However, as mentioned before, we observe a total elongation of $50\mu m$, therefore only part of the morphogenetic process is reproduced; thus we can deduce that $t^{GBE}_{MAX} = 0.02$ corresponds to $20mn$ of the real convergent-extension movement. If we indicate for our incremental parameter $t$ that $\triangle t = 0.02$ and for the real period of time that $\triangle t_{physics} = 20mn$ and we calculate the velocity rate vectors $\partial u_{max}/\partial t$ at the final configuration, the maximal velocity $v_{max}$ can be qualitatively computed from

$$v_{max} = \frac{\partial u_{max}}{\partial t} \frac{\triangle t}{\triangle t_{physics}} \cong 0.25\mu m/mn \tag{3.32}$$

In Fig. 3.20 we show the velocity field for our simulation together with the experimental one obtained by Supatto (Supatto et al. [2005]). He has detected, by microscopy observations on wild-type embryos, the velocity field at $t_{physics} = 29mn$ and he has found a maximal velocity in the order of a few $\mu m/mn$, which is larger than our previous result. In despite of this, in both cases, the trend of the velocity field is very similar; in particular we remark an acceleration toward the posterior pole and the vortex movement at the dorso-lateral region.

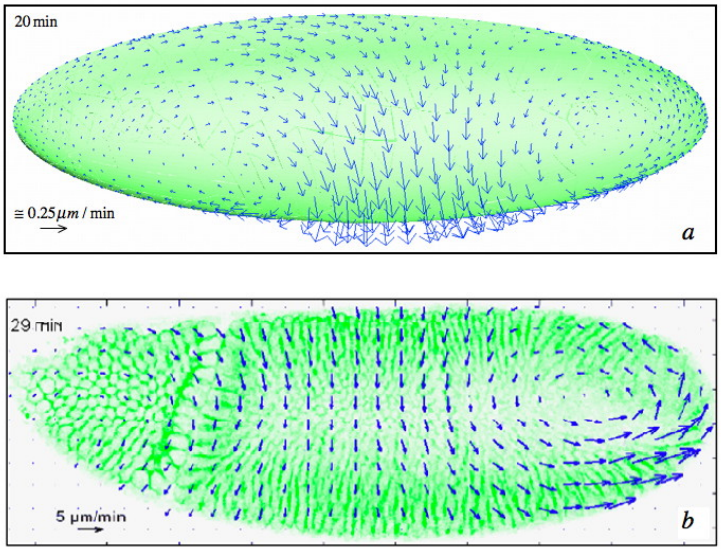


*Figure 3.20:* (a) Frontal view of the embryo at the end of the GBE simulation ($t^{GBE}_{MAX} = 0.02$). The blue arrows show the velocity field (black scale arrow, $\cong 0.25\mu m/mn$) (b) Velocity field for real wild-type embryo experimentally obtained (black scale arrow, $5\mu m/mn$) (Supatto et al. [2005]).

## 3.8 Hyperelastic model tested for GBE

As described in Sec. 2.3, we have chosen to model the mesoderm as a Saint-Venant material, which is probably not the best approach for our problem for two principal reasons. First of all, in previous works we often found a hyperelastic analysis of the mechanical characteristics of the embryo. Secondly, we are aware that the embryonic tissues show visco-elastic properties that are therefore not taken into account here, but may strongly affect the global behaviour of the system.

In order to catch up with these drawbacks, we have decided first to make a comparison between our model, which is simple and linear, and the hyperelastic models proposed in literature. In Sec. 2.3 we have pointed out the fact that the equation describing the Neo-Hookean material, which is a particular case of a Mooney-Rivlin material, corresponds to a quadratic form of the Saint-Venant model (Eq.[2.47]). By a power extension linearized to the first order of the Neo-Hookean constitutive law and imposing a vanishing initial stress, we are able, from Eq.[2.48], to deduce the values for $\alpha_1$ and $\alpha_2$, which are defined for the hyperlastic model considered. Therefore we obtain for our specific case that $\alpha_1 = \mu_L/2 \simeq 17$ and $\alpha_2 = \mu_L/2 \simeq -17$ ($\mu_L$ is the classical Lamé's coefficient defined in Eq.[2.37]).

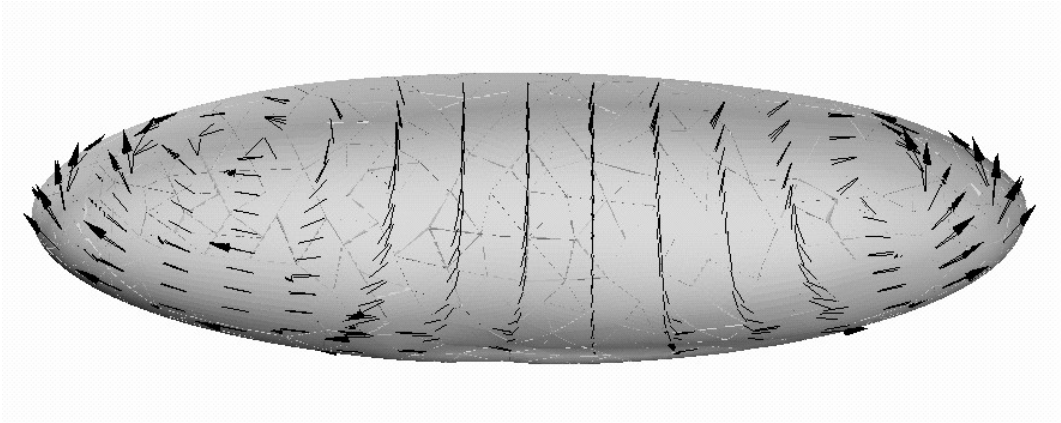

*Figure 3.21:* Simulation of the GBE with a hyperelastic model; the arrows represent the displacements field. The results show a high similarity with the ones with a Saint-Venant model.

We have tested the hyperelastic model for the GBE simulation. The new parameters previously found have been implemented and we have replaced the expression of the Second Piola-Kirchhoff tensor (Eq.[2.44]) with the new one in the PVP formulation. The results are very similar to the ones obtained in Sec. 3.7. It is possible to see a beginning of the vortex movement at the posterior pole of the embryo even tough the convergence from the dorsal to the ventral region is less worsen. At the

maximal values $\alpha_\theta^{GBE}(t) = \alpha_\theta \cdot t_{MAX}^{GBE}$ and $\alpha_z^{GBE}(t) = \alpha_z \cdot t_{MAX}^{GBE}$, $t$ varying between 0 and 0.023, we find a maximal elongation and shortening of the germ band respectively of about $56\mu m$ and $23\mu m$. Such values are not so different from the ones found with a Saint-Venant model (Sec. 3.7); we can then conclude that our first choice can be considered appropriate for the analysis of our problem.

## 3.9 Estimation of the induced forces through the embryo

In the present study, the gradient decomposition method allows us to take into account the active and the passive forces that provide the final configuration for each morphogenetic movement that we simulate. The passive forces are considered as a consequent response to the active ones that have been individuated by biologists through experimental observations. It is still difficult to detect which ones among the elementary deformations acting on the cells have to be hold as active and which ones as passive forces. In particular this is evident for the ventral furrow invagination (Sec. 1.2.3) where five movements have been observed and only two of them are considered as active. Contrarily our simulations have pointed out that even when only one of these elementary forces, specifically apical constriction, is implemented we still obtain the invagination of the mesoderm into the yolk (Sec. 3.5).

So far the active forces are directly introduced into our formulation but they are actually engendered by chemical signals developing within the embryo that are not taken into account here. Similarly, we are aware that the passive forces produced at the active regions and responsible, in our specific case, for the formation of the ventral and the cephalic furrows and the germ band extension, may in turn trigger new active forces elsewhere in the embryo. This key aspect has been amply studied by Farge and co-workers for the germ band extension. In fact they have demonstrated that the tissues extension at the ventral region leads to a consequent pressure at the anterior pole where, therefore, the expression of the *twist*, a gene which normally is only ventrally expressed, is observed (Brouzés and Farge [2004], Farge [2003]). This means that not only there is a continuous and concatenate series of mechanical forces developing during embryogenesis, but also and more importantly that such forces may highly influence the expression of specific genes also at long distance in the embryo, which implies a mechanotransduction pattern throughout the development.

For this reason we believe it is important to evaluate how the tissues adjacent to the active regions respond and behave when the active forces are applied. In order to do so, we are going to analyze the volume variation $\triangle V$ within the mesoderm, which indicates if the cells compress or expand. We can write

$$\triangle V = \frac{dV - dV_0}{dV_0} = \frac{dV}{dV_0} - 1 = det\mathbf{F} - 1 \tag{3.33}$$

From the definition of the Right Cauchy-Green deformation tensor $\mathbf{C}$ (Eq.[A.11]), we have

$$\mathbf{C} = \mathbf{F}^T\mathbf{F} = \mathbf{I} + 2\,\mathbf{E} \tag{3.34}$$

$$(det\mathbf{F})^2 = det(\mathbf{I} + 2\,\mathbf{E}) \tag{3.35}$$

Then, by a 1st order approximation, we obtain

$$det\mathbf{F} \cong 1 + tr\mathbf{E} \tag{3.36}$$

and Eq.[3.33] becomes

$$\triangle V \cong tr\mathbf{E} \tag{3.37}$$

Consequently, the pressure force that can be engendered within the embryo is calculated as

$$p_m = \frac{tr\mathbf{S}_m}{3} = k_m tr\mathbf{E}_m = \frac{E}{3(1-2\,\nu)} tr\mathbf{E}_m \tag{3.38}$$

where $\mathbf{S}_m$ is the Second Piola-Kirchhoff tensor which provides the constitutive law of the mesoderm (Eq.[2.35]), $k_m$ is the coefficient of compressibility for the mesoderm and $\mathbf{E}_m$ is the Green-Lagrange tensor as defined in Eq.[2.36], which varies between the active and the passive regions.

We are now going to estimate, for each morphogenetic movement, the magnitude of the induced pressure forces. First of all it has to be noticed that for the simulation of the ventral and the cephalic furrows the strains are highly concentrated at the active zone, so that the forces slightly spread around. In the case of the germ band extension instead, we observe that, even if at a lower rate, the strains can also be transmitted at long distance, as later on described.

For the ventral furrow (when both apical constriction and apico-basal elongation are implemented) we observe the elongation of the basal surfaces of the cells at the median hinge point, while the apical surface are constricted as expected; also tissues extend internally at the dorso-lateral hinge points, even if the amplitude of such extension is much smaller than the former one (Fig. 3.22). The same observations can be drawn for the cephalic furrow where, according to the elementary active force introduced (apical constriction), we have a compression of the cells on the external surface, while they enlarge at the internal surface. From a quantitative point of view it is possible to estimate the range of values for $p_m^{VFI}$ and $p_m^{CF}$ in the active

and passive region (all the parameters are the same as described in Sec. 3.5 and 3.6 respectively) as reported here below

$$\text{active region} \begin{cases} -167Pa < & p_m^{VFI} < & 1906Pa \\ -193Pa < & p_m^{CF} < & 1770Pa \end{cases} \tag{3.39}$$

$$\text{passive region} \begin{cases} -447Pa < & p_m^{VFI} < & 447Pa \\ -440Pa < & p_m^{CF} < & 209Pa \end{cases} \tag{3.40}$$

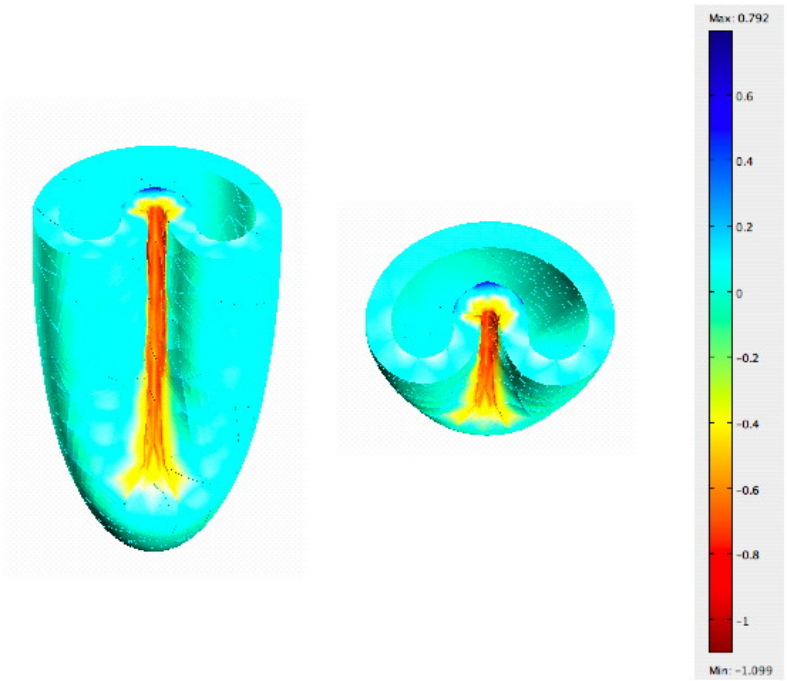


*Figure 3.22:* Volume variation $\triangle V$ for the VFI simulation. On the left a bottom view, on the right a cross-sectional view.

The analysis of the germ band extension is more interesting because the results can be compared with experimental observations. The convergent-extension movement of the cells is implemented for this simulation in order to obtain the final extension of the germ band at the ventral area of the embryo. The dorso-lateral tissues around the active region undergo a compression along the dorsal-ventral axis, while in the ventral area tissues elongate thus an extension is observed. Such extension reaches the anterior and posterior poles, where it is restrained by the sharpened curvature of the embryo and where a slight compression occurs on the dorsal side.

It is possible to locally evaluate the volume variation so that we find $\triangle V = -0.0014$ and $\triangle V = -0.007$ respectively at the anterior and the posterior pole (Fig. 3.23). The negative sign clearly indicates a compression of the cells whose magnitude is in the order of the mean sagittal deformation that have been experimentally determined (Desprat et al. [2008], Supatto [2005]). The estimated pressure when the germ band extension occurs can be calculated again for the active and the passive regions and we obtain

$$\begin{cases} \text{active region} & -13Pa < p_m^{GBE} < 23Pa \\ \text{passive region} & -43Pa < p_m^{GBE} < 7Pa \end{cases} \tag{3.41}$$

and specifically at the anterior and the posterior pole, which are included in the passive region, we find $-0.46Pa$ and $-2.33Pa$ respectively. These data confirm therefore, from a qualitative point of view, the experimental observations that show the presence of a compression at the anterior pole. In order to have a quantitative analysis, it would be necessary to evaluate the magnitude of the real pressure, to compare it with the value found for our simulation.

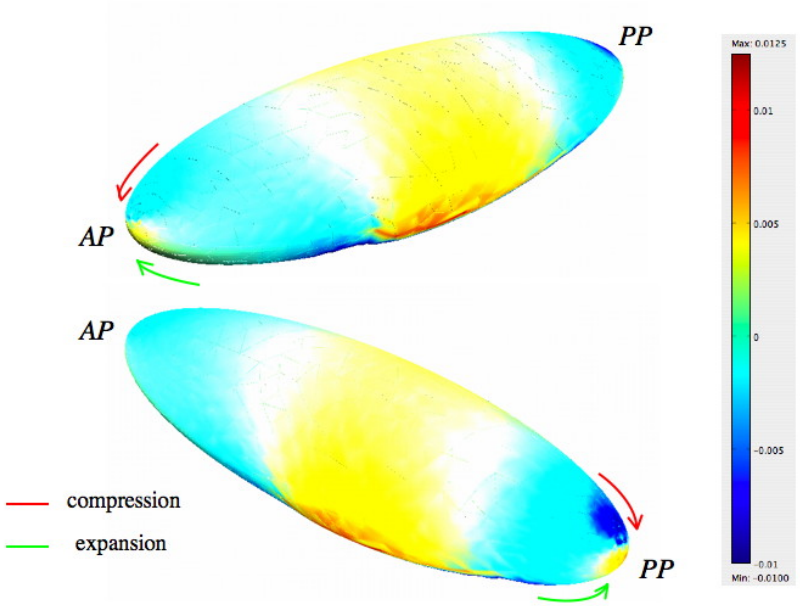


*Figure 3.23:* Volume variation $\triangle V$ for the GBE simulation. Here the values scale has been adapted to highlight the effects on the anterior and posterior pole.

## 3.10 Estimation of the induced shear stress through the embryo

If the variation of the mesoderm volume previously calculated indicates how the cells compress or expand, the norm of the deviator of the Green-Lagrange tensor $\mathbf{E}_m$ for the passive deformation, as similarly as for the Von Mises criterion, consents to determine how the cells behave with respect to one another. It provides the distribution of the shear deformations through the mesoderm domain and it is defined as follows

$$\|dev\,\mathbf{E}_m\| = \sqrt{\begin{array}{l}\mathbf{E}^2_{m_{xx}} + \mathbf{E}^2_{m_{yy}} + \mathbf{E}^2_{m_{zz}} - \mathbf{E}_{m_{xx}}\mathbf{E}_{m_{yy}} - \mathbf{E}_{m_{yy}}\mathbf{E}_{m_{zz}} - \mathbf{E}_{m_{xx}}\mathbf{E}_{m_{zz}} \\ +3\,\mathbf{E}^2_{m_{xy}} + 3\,\mathbf{E}^2_{m_{yz}} + 3\,\mathbf{E}^2_{m_{xz}}\end{array}} \tag{3.42}$$

For the germ band extension, when the parameters are the same as the ones obtained in Sec. 3.7, we find $dev\,\mathbf{E}_m = 0.01$ and $dev\,\mathbf{E}_m = 0.014$ respectively at the anterior and the posterior pole. In order to estimate the magnitude of the strain induced at the two poles by the extension of the germ band, $dev\,\mathbf{E}_m$ can be compared, at first approximation, to the shear deformation $\gamma$, so that we can write

$$\tau = \mu\,\gamma \simeq \mu_L \|dev\mathbf{E}_m\| \tag{3.43}$$

where $\tau$ is the shear stress and $\mu_L$ the Lame's coefficient (Eq.[2.37]). Therefore, having $\mu_L = 34.4$, we obtain $\tau_{GBE} \simeq 0.34Pa$ at the anterior pole and $\tau_{GBE} \simeq 0.48Pa$ at the posterior pole; globally $\tau_{GBE}$ varies from a minimal value of about $0.01Pa$ to a maximal value of $6.88Pa$. For the ventral and the cephalic furrow we find instead $0.13Pa < \tau_{VFI} < 198Pa$ and $0.07Pa < \tau_{CF} < 190Pa$ respectively; these values are largely greater than the ones obtained for the GBE, where the strains are less concentrated and may be transmitted at long distance within the embryo. Actually, if we ma ke a comparison with experimental data, we notice that the maximal value for $\tau_{GBE}$ is in the order of the laminar shear stress applied on cells placed in a bioreactor over $24h$, that is usually comprised between 10 and $30Pa$ (Traub and Berk [1998]). At this intensity the shear stress may induce several cellular effects such as coagulation, migration, proliferation or adhesion.

## 3.11 Influence of the geometry on VFI and GBE

As described in Sec. 3.1, the embryo is parametrically represented here by an ellipsoid in a cylindrical coordinates system. However, the real embryo presents a non-perfect symmetry between the anterior and the posterior pole which may influence those morphogenetic movements that take place along the horizontal axis.

Furthermore it is possible to observe several changes in curvature that one must take into account. Therefore we present an analysis of the curvature radius $\rho(z)$ (Eq.[3.3]) for the particular cases of the ventral furrow invagination and the germ band extension. It has to be said that for the VFI we have implemented here only the apical constriction and, for both the events (VFI and GBE), all the variables are set as in Sec. 3.2 and 3.3. Any modification of $\rho(z)$ will affect the initial position of the points $\mathbf{p}$ within the thikness of the mesoderm (Eq.[3.4]) and therefore the expression of the intermediate position $\bar{\mathbf{x}}$ will change too. This specific study has been conducted in collaboration with Anne-Sophie Mouronval of the MSSMat Laboratory and it has been proposed for the first time at the 9ème Colloque National en calcul de structure de Giens (Mouronval et al. [2009]).

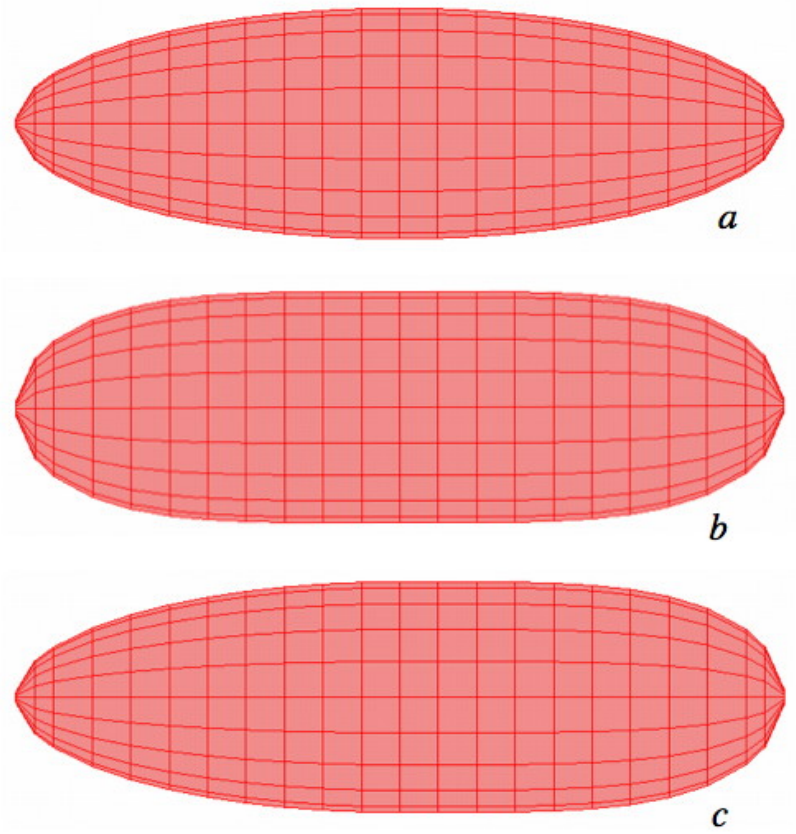


*Figure 3.24:* Three different geometries have been tested. (a) The regular ellipsoid (b) A symmetric geometry where both the poles are enlarged (c) A non-symmetric geometry where only the posterior pole is more rounded.

So far three geometries have been tested: the ellipsoid (1st case), a symmetric

geometry with respect to the vertical axis where the poles are enlarged (2nd case), an asymmetric case with only one enlarged pole (3rd case) (Fig. 3.24). All the geometries are obtained using the *loft* function in Matlab, which allows to construct a three dimensional object from an adjacent series of two dimensional surfaces.

**1st case**

The first case is represented by the ellipsoid that is parametrically obtained by $\rho(z)$ as defined in Eq.[3.3] (Fig. 3.24a).

**2nd case**

Here the symmetry with respect to the vertical axis is maintained, but the radius $\rho(z)$ is modified and can be written as

$$\rho(z) = b\sqrt{1-\left(\frac{z}{a}\right)^4} \tag{3.44}$$

which provides a global geometry as in Fig. 3.24b, where the two poles are more rounded than for the ellipsoid.

**3rd case**

The third case is a combination of the classical ellipsoid (1st case) and the previous geometry (2nd case). Actually $\rho(z)$ changes according to the horizontal coordinate as follows

$$\begin{cases} z<0 & \rho(z) = b\sqrt{1-\left(\frac{z}{a}\right)^2} \\ z>0 & \rho(z) = b\sqrt{1-\left(\frac{z}{a}\right)^4} \end{cases} \tag{3.45}$$

so that the embryo is represented as in Fig. 3.24c. This geometry better reproduces the real embryo since the symmetry with respect to the dorsal-ventral axis of the embryo is no more respected and only the posterior pole is more rounded.

**Results**

When comparing the three cases for the VFI (Fig. 3.25, 3.26), we observe a greater invagination for the case of the ellipsoid for any $z$ considered and in particular at $z = 0$. The invagination for the the 3rd case is asymmetric and similar to the first case for $z < 0$ and to the second one for $z > 0$, while at $z = 0$ the amplitude is intermediary between the two previous cases.

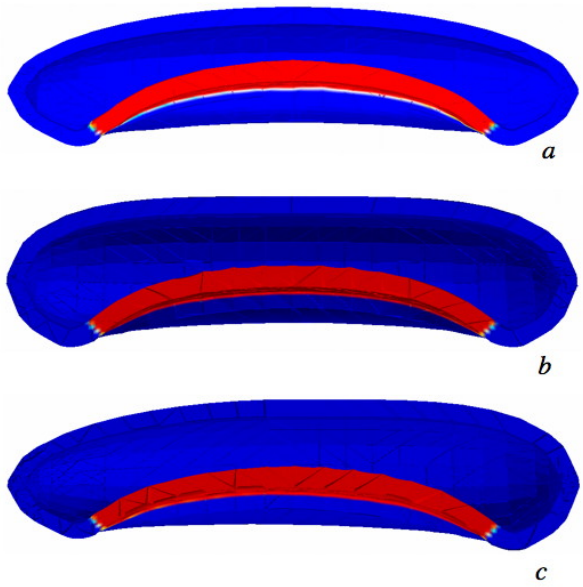


*Figure 3.25:* Frontal sections of the ventral furrow invagination for the 1st geometry (a), the 2nd (b) and the 3rd (c).

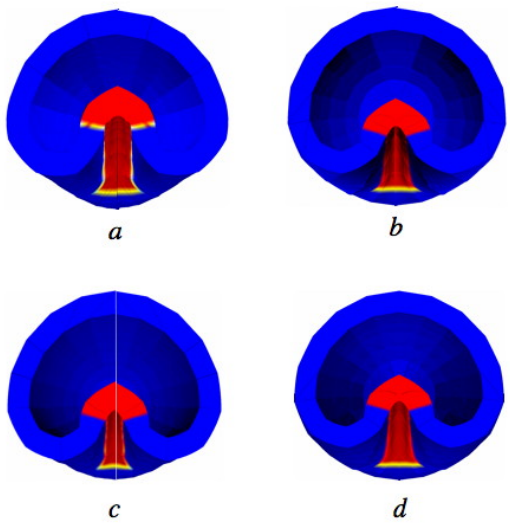


*Figure 3.26:* Cross sections of the ventral furrow invagination. (a) and (b) represent the 1st and the 2nd geometries, while (c) and (d) correspond to $z < 0$ and $z > 0$ respectively for the 3rd case.

For the simulation of the GBE (Fig. 3.27) it is evident from the 2nd and the 3rd geometries that when the anterior or the posterior pole are more rounded, the tissues are able to extend more toward the dorsal region of the embryo than for the case of the regular ellipsoid. Such greater elongation at the posterior pole is actually observed in real embryos and, because of the presence of the cephalic furrow which constipate the displacements, leads to the formation of little invaginations at the dorsal region that are not reproduced for our simulation.

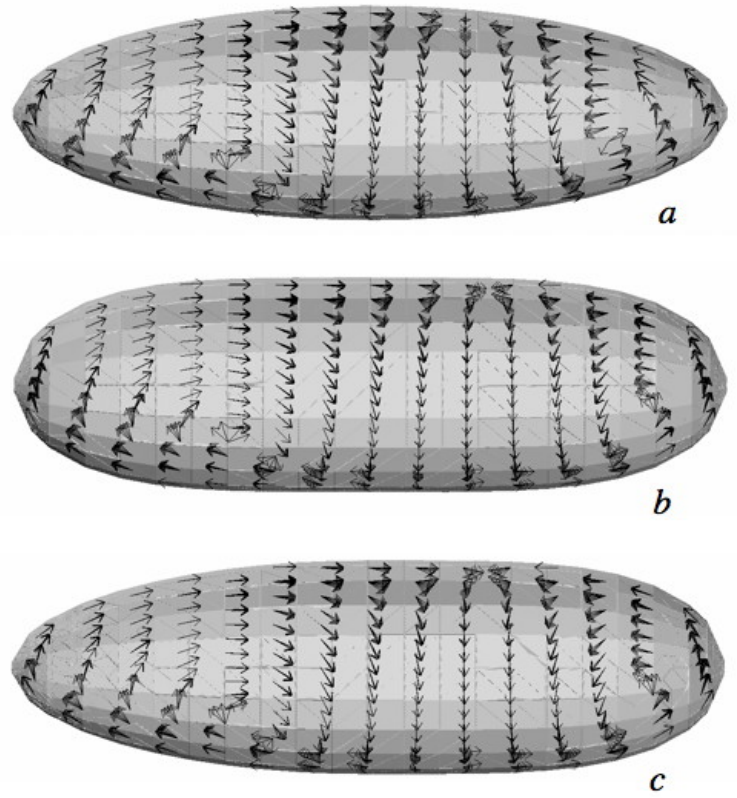


*Figure 3.27:* Results for the GBE when the three geometries are used (a) 1st case (b) 2nd case (c) 3rd case.

These results show how a local change of $\rho(z)$ may non-locally influence the final configurations because of the longitudinal displacements. In particular a larger curvature of the poles influences the global displacements, especially for the case of the GBE at the posterior pole. On the other hand the non-symmetry with respect the dorsal-ventral axis of the embryo does not provide evident differences between the anterior and the posterior poles for what concerns the deformations. At present we are working on two other geometries that take into account the flattening of

the mesoderm on the dorsal region of the embryo and the greater curvature at the ventral part.

**4th case**

Here $\rho(z)$ is still the same as for the ellipsoid but any point $\mathbf{p}_0$ on the middle surface will be expressed this time as

$$\mathbf{p}_0 = \rho(z)\mathbf{i}_r(\theta) + z\,\mathbf{i}_z + \beta\left(\frac{z}{a}\right)^2 \mathbf{i}_x \tag{3.46}$$

where the last term consents to displace the two dimensional surfaces, used to obtain the three dimensional geometry, along the vertical axis of the embryo of a constant $\beta$, so that the symmetry with respect to the anterior-posterior axis is no more respected (Fig. 3.28). The new equation for $\mathbf{p}_0$ is not defined in a proper cylindrical polar basis anymore, thus the *covariant* and *contravariant* basis must be recalculated. With this representation the dorsal region will be flatter, while the ventral region more rounded and still symmetric with respect to the dorsal-ventral axis.

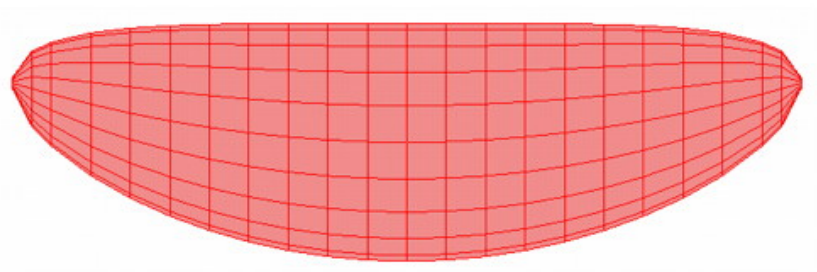

*Figure 3.28:* A symmetric geometry with respect the vertical axis, but asymmetric with respect to the horizontal axis. The dorsal region is flatter while the ventral one more rounded.

**5th case**

The last case is the most complex, but also the most realistic; it results by the combination of the 3rd and the 4th case. All the points $\mathbf{p}_0$ on the middle surface of the mesoderm are still defined as in Eq.[3.46], but this time also $\rho(z)$ changes according to Eq.[3.45]. This geometry is the most accurate since it allows to reproduce both the flattening of the dorsal region of the embryo and the asymmetry between the anterior and the posterior pole.

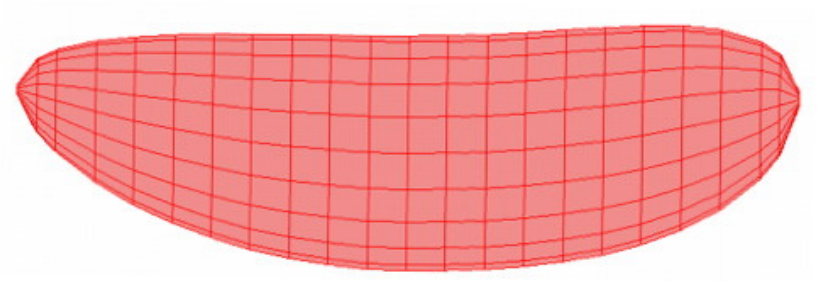

*Figure 3.29:* An asymmetric geometry with respect to both the vertical and the horizontal axis. Actually the dorsal region is flatter and the posterior pole is more rounded than the anterior one.

## 3.12 Conclusions

We consider that the model we have presented here is innovative and original for several aspects.

First of all, it allows to simulate three morphogenetic movements: ventral furrow invagination, cephalic furrow formation and germ band extension. Two of them have been investigated for long time and many models have been proposed in literature (Chapter 1); for what concerns the cephalic furrow instead, this is, to the best of our knowledge, the first time it has been reproduced. The three morphogenetic events are therefore obtained using the same model, which constitutes one of the main advantages of the present work. This is possible because, by the parametric description of the geometry of the embryo, each active deformation gradient $\mathbf{F}_a^i$ has a proper expression according to the movement considered and it is user defined, which consents to easily modified it.

The elements of the mesh used for our simulations do not coincide with the cells of the mesoderm. This choice has been made for multiple reasons:

- given the small dimensions of the system we are working with, it would have not been trivial to obtain a mesh whose elements are exactly equivalent to the cells of the single layer composing the mesoderm;
- in order to get a higher precision for the results, it would have been probably necessary to refine the mesh much more than a single cells size, thus more computer time consuming would have been demanded to run the simulations;
- a mesh element does not correspond to a specific geometrical object, contrarily to the meshed region (the embryo), but it rather supplies the functions by which we express the unknown displacements field.

The elementary active forces introduced for each movement are then mesh independent, but it is however possible to visualize, through specific analytical markers, the material cells and the relative deformations that they undergo all long the simulation.

To represent the mesoderm we have decided to use a Saint-Venant material, which may appear at first sight an approach too simplistic and approximative for our problem, since we are treating with a biological system where many parameters have to be taken into account. Although, we have extensively compared the constitutive law we use with the models found in literature and have also showed that the results obtained for our simulations, specifically for the germ band extension, are not so different from the ones obtained for a Neo-Hookean material (Sec. 3.8). Therefore our choice results appropriate and the linearity of the constitutive law consents to skip out material's constants that are usually very difficult to detect. Nevertheless, so far we have not taken into account the visco-elasticity of the mesoderm, which may play a significant role and may affect the global response of the embryo. This is one of the aspects we would like to develop in the future and on which we are working in order to have a model completely coherent with the reality.

The simulation of the ventral furrow invagination provides very interesting results; if we compare it with the *in vivo* experiments we notice a strong similarity, except for the amplitude of the invagination into the yolk, which results more accentuated for our model. Together with an initial simulation where only apical constriction is introduced as active force on the cells (Sec. 3.5), we have done further analysis by which we have individuated the parameters that can influence the final configuration. Among them we find the size of the active region of the deformation (Sec. 3.5.1), the dimensions of the material cells (Sec. 3.5.2), the apico-basal elongation (Sec. 3.5.3) and the geometry of the embryo (Sec. 3.11). With this study we are able to confirm in part what has been pointed out by biologists and also to put forward a relevant conclusion, which may change the global view of the problem. Actually, by experimental observations, it has been possible to find five elementary cells deformations and it has been deduced that only two of them, the apical constriction and the apico-basal elongation, are active forces, while the other three could be considered passive responses of the cells. In spite of this consideration, in our first simulation, where only apical constriction is implemented, we obtain the invagination of the mesoderm: therefore we can conclude that probably only this active force really triggers the narrowing of the mesoderm, whereas all the others are effectively a passive reaction of the cells due to their need to find a final configuration assuring the integrity and the continuity of the system.

Even though, as mentioned before, the cephalic furrow has never been simulated and therefore our model can be considered forerunner in this sense, it presents some limitations on which we are trying to work to get a more realistic representation. In fact, observing experimental movies of the embryo development, we notice that the furrow starts to form vertically but then, probably pushed by the germ band

extension, it moves forwards, towards the anterior pole, so that its final position results to be inclined at 30° with respect to the dorsal-ventral axis of the embryo. The analysis of this peculiar characteristic would have probably demanded a Eulerian formulation of the problem, but for sake of simplicity we have decided to begin with an easier modelling. Therefore the active deformation region is placed vertically at one third of the horizontal length of the embryo. Given the considerations made for the ventral furrow simulation, here again we only implemented the apical constriction and we still get the narrowing of the mesoderm into the yolk: once more our conclusion can be considered valid and pertinent.

The simulation of the germ band extension has been the first to be performed because the convergent-extension movement seemed to be much simpler than the others to formulate and reproduce and also because many were the aspects to compare with the experimental observations. In particular, we have analyzed how the forces are transmitted through the embryo when the extension of the ventral tissues occurs; even if at lower rates, for this specific case, the strains are less concentrated than for the VFI and CF formation and easily spread around. Actually, we have found a compression at the anterior pole, in the order of some $Pa$, which may correspond to the one observed by biologists and responsible for the expression of the *twist*, a gene normally expressed at the ventral region only. This represents a significant support to the hypothesis according to which there would be a mechanotransduction pattern through the embryo allowing to transform a mechanical stimulus into a chemical signal. It is therefore necessary to take into account the fact that the passive forces, so far considered as a consequent response to the active ones directly introduced into the formulation, may play the role of active forces and lead to new strains elsewhere in the embryo.

Given the consistence of the results for the individual simulations of the three morphogenetic movements, we have decided to improve our model coupling together the single formulations in order to obtain a concurrent simulation of the events. In the next chapter we are going to present this last part of the work and the approaches that have been employed.

# Chapter 4

# Concurrent simulation of morphogenetic movements

Given the coherent results obtained for the individual simulations of the morphogenetic movements, we have decided to perfom a concurrent simulation. Such simulation allows to put together, by two or three, the events previously described (Sec. 3.2, Sec. 3.3) in the real chronological order, so that an exhaustive representation of the successive phases of the *Drosophila* gastrulation is provided. This part of the study represents the most innovative contribution of our work because, to the best of our knowledge, never before this aspect of the problem have been treated.

In this chapter we are going to describe the two methods proposed for this specific simulation. The first approach (Sec. 4.1) is the most intuitive and it does not require further manipulations to be tested. Actually it consists in coupling together the movements by the simple multiplication of the proper active deformation gradients $\mathbf{F}_a^i$, as found in Chapter 3. Therefore the final deformation is still the composition of the passive and the active deformations, but this time the latter is represented by the active gradients as many as the morphogenetic movements we want to reproduce. The results are interesting for the concurrent simulation of the two furrows, while when the germ band extension is introduced, the method presents some limitations. Thus a more adapted and precise formulation is necessary, that is an "updated" Lagrangian formulation, which consents to take into account some important aspects so far put aside. Above all, the fact that the cells, when belonging to more than one active deformation regions, are involved in successive elementary deformations implies that we have to consider the modification of the initial configuration. For this second method then, the final deformation of the mesoderm is decomposed into a series of intermediate deformations, so that the reference configuration is updated as similarly as for a Eulerian formulation. In Sec. 4.2 we describe in detail the approach that constitutes one of the major perspective of the present work.

## 4.1 Lagrangian formulation

When coupling together several morphogenetic movements it is necessary to evaluate peculiar aspects that generate the complexity of the problem.

First of all, each movement has a proper active deformation gradient $\mathbf{F}_a^i$, which has been analytycally obtained thanks to the parametrical description of the geometry and according to the elementary forces introduced. Therefore, when combining more than one event, the values of the constants $\alpha_i$ in the relative expressions of the deformation rates $\alpha^i(t) = \alpha_i \cdot t$, have to be adjusted in order to simultaneously satisfy the suitable properties of convergence and final consistent results.

Secondly, there is a time delay between the occurence of the events. Actually, the formation of the ventral and the cephalic furrows takes place at the same time (even if the cephalic furrow takes less time to complete); the germ band extension instead begins while the ventral furrow is not fully formed. For the sake of simplicity, we will assume here that the GBE occurs only once the ventral furrow has reached its final form.

Finally, each morphogenetic movement occurs at a different region of the embryo, therefore sometimes the intersection of these active regions may not be empty. For the cephalic and the ventral furrows the size of the intersection is very small, while a larger area has to be considered for the ventral furrow and the germ band, which might inhibit the deformations when the $\mathbf{F}_a^i$ are superposed. Additionally, from experimental movies, we can deduce that, once formed, the ventral furrow closes internally, so that the two strips of the mesoderm fuse together and the ventral region is no more deformed by the invagination, but a new tissue appears, similar to the initial one. The open question is then if the germ band extension involves cells that have already been deformed by the formation of the two furrows, or a population of new cells undergoes the convergence-extension movement on the dorsal-lateral area of the embryo.

For the first method, the Lagrangian formulation presented in Chapter 2 is maintained. The gradient decomposition is still applied, thus the final deformation can be written as the composition of the active and the passive deformations (Eq.[2.2]), but when coupling together more than one morphogenetic movement, the active deformation gradient is the multiplication of each active deformation gradient, as many as the events taken into account, so that we can write

$$\mathbf{F} = \mathbf{F}_m \mathbf{F}_a^n \mathbf{F}_a^{n-1} ... \mathbf{F}_a^1 \tag{4.1}$$

This approach is to be related to the multi-configuration advocated by Sidoroff (Sidoroff [1976]) in the modelization of large visco-elastic deformations with several Maxwell units.

### Concurrent simulation of VFI and CF formation

First of all, we simulate the ventral and the cephalic furrow formation since they occur at the same time. The active regions, where the elementary deformations are applied, are the same as the one described in Sec. 3.2; therefore, by the superposition of the two, an intersection appears at the ventral area of the embryo (Fig. 4.1).

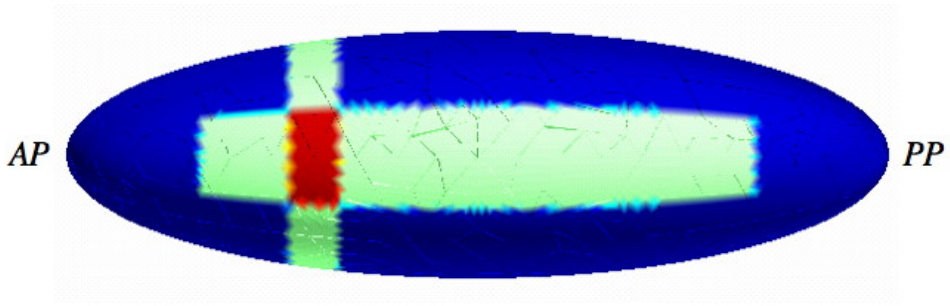


*Figure 4.1:* Ventral view of the embryo. Both the active regions for the ventral and the cephalic furrows are represented (light green); in red the intersection of the two.

From Eq.[4.1], we can write

$$\mathbf{F} = \mathbf{F}_m \mathbf{F}_a^{VFI} \mathbf{F}_a^{CF} \tag{4.2}$$

The active deformation gradients $\mathbf{F}_a^i$ are obtained from Eq.[3.6]. In order to take into account the time delay between the events, we have introduced a function $g(t)^i$ depending on the icremental parameter $t$; this function allows us to settle the beginning and the end of each morphogenetic movement (Fig. 4.2).

Therefore the active deformation gradient for the ventral furrow invagination (only apical constriction is introduced for this case (Eq.[3.31])) becomes

$$\begin{aligned}\mathbf{F}_a^{VFI} = &\left[1 + \alpha^{ac}(g(t)^{VFI})\frac{2\zeta}{h}m'(\theta)\right]\mathbf{i}_\theta(\tilde{\theta}) \otimes \mathbf{i}_\theta(\theta) \\ &+ \frac{\left[\rho'(z)\mathbf{i}_r(\tilde{\theta}) + \mathbf{i}_z\right]}{(1+\rho'^2(z))} \otimes \left[\rho'(z)\mathbf{i}_r(\theta) + \mathbf{i}_z\right] \\ &+ \left[\frac{2\alpha^{ac}(g(t)^{VFI})}{h}m(\theta)\varphi_\theta \mathbf{i}_\theta(\tilde{\theta}) + \mathbf{n}_0(\tilde{\theta}, z)\right] \otimes \mathbf{n}_0(\theta, z)\end{aligned} \tag{4.3}$$

where

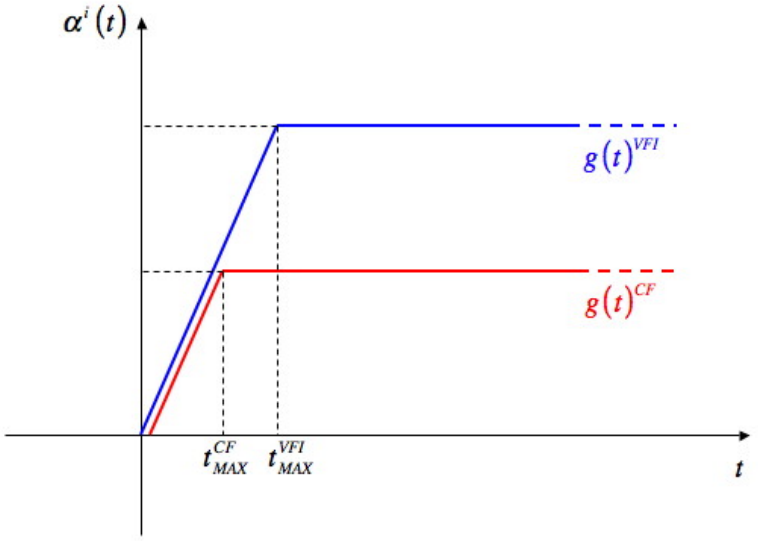


*Figure 4.2:* Both the furrows start to form at $t = 0$, but the cephalic furrow stops earlier ($t^{CF}_{MAX} = 0.01$), while the ventral one takes more time to completely form ($t^{VFI}_{MAX} = 0.03$).

$$g(t)^{VFI} = \begin{cases} t < t^{VFI}_{MAX} & \alpha_{ac} \cdot t \\ t \geqslant t^{VFI}_{MAX} & \alpha_{ac} \cdot t^{VFI}_{MAX} \end{cases} \tag{4.4}$$

For the cephalic furrow, according to Eq.[3.23], we have

$$\begin{aligned} \mathbf{F}^{CF}_a =& \frac{\tilde{\varphi}^{CF}_\theta}{\varphi_\theta} \mathbf{i}_\theta(\theta) \otimes \mathbf{i}_\theta(\theta) \\ &+ \frac{\left[1 + \alpha^{ceph}(g(t)^{CF}) \frac{2\zeta}{h} m'(z)\right] \tilde{\varphi}^{CF}_z}{\varphi_z(1 + \rho'^2(z))} (\rho'(\tilde{z})\mathbf{i}_\theta(\theta) + \mathbf{i}_z) \otimes (\rho'(z)\mathbf{i}_r(\theta) + \mathbf{i}_z) \\ &+ \left[\frac{2\alpha^{ceph}(g(t)^{CF})}{h} m(z) \tilde{\varphi}^{CF}_z (\rho'(\tilde{z})\mathbf{i}_r(\theta) + \mathbf{i}_z)\right] + \mathbf{n}_0(\theta, \tilde{z}) \otimes \mathbf{n}_0(\theta, z) \end{aligned} \tag{4.5}$$

with

$$g(t)^{CF} = \begin{cases} t < t^{CF}_{MAX} & \alpha_{ceph} \cdot t \\ t \geqslant t^{CF}_{MAX} & \alpha_{ceph} \cdot t^{CF}_{MAX} \end{cases} \tag{4.6}$$

The two furrows start at the same time at $t = t^{VFI}_{min} = t^{CF}_{min} = 0$, but, since involving a smaller number of epithelial cells, the cephalic furrow takes less time to form. Thus its process of formation stops at $t^{CF}_{MAX} = 0.01$, while the ventral furrow keeps to develop until $t^{VFI}_{MAX} = 0.03$, when the convergent-extension movement would start and the furrow has completed the invagination into the yolk. It has to be noticed that the values of $t^{VFI}_{MAX}$ and $t^{CF}_{MAX}$ are larger than the ones found for the individual simulations, even if the maximal values of deformations for the VFI and CF formation are the same as the previous ones, respectively $\cong 7\mu m$ and $\cong 5\mu m$. This is mostly due to the high non-linearity of the problem which requires a diminution of the $\alpha_i$ in the expression of the deformation amplitudes in order to match the right properties of convergence; therefore the smaller the $\alpha_i$, the greater $t^i_{MAX}$.

The results are very interesting (Fig. 4.3); the two furrows are clearly developed and, at the intersection of the two active regions of deformation, it is possible to observe a further invagination of the mesoderm probably due to the superposition of the apical constriction along the anterior-posterior axis for the cephalic furrow and along the radial direction for the ventral furrow.

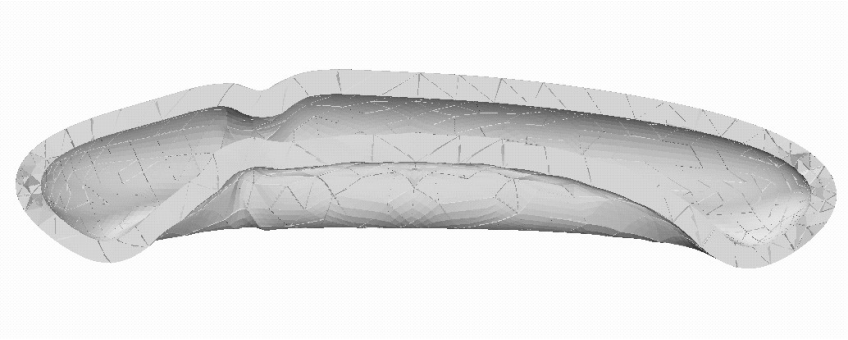

*Figure 4.3:* Cross sectional view of the embryo for the concurrent simulation of the ventral furrow invagination and the cephalic furrow formation ($t = 0.03$).

**Concurrent simulation of VFI , CF formation and GBE**

When adding the germ band extension, which is the last morphogenetic movement to take place, the total deformation gradient $\mathbf{F}$ can be written as

$$\mathbf{F} = \mathbf{F}_m \mathbf{F}^{GBE}_a \mathbf{F}^{VFI}_a \mathbf{F}^{CF}_a \tag{4.7}$$

where $\mathbf{F}^{VFI}_a$ and $\mathbf{F}^{CF}_a$ are the same of Eq.[4.3, 4.5], while $\mathbf{F}^{GBE}_a$ is equal to

$$\begin{aligned}\mathbf{F}_a^{GBE} =& \frac{(1+\alpha_\theta^{GBE}(g(t)^{GBE})\tilde{\varphi}_\theta^{GBE}}{\varphi_\theta}\mathbf{i}_\theta(\tilde{\theta})\otimes\mathbf{i}_\theta(\theta)\\ &+\frac{(1+\alpha_z^{GBE}(g(t)^{GBE})\tilde{\varphi}_z^{GBE}}{(1+\rho'^2(z))\varphi_z}(\rho'(\tilde{z})\mathbf{i}_r(\tilde{\theta})+\mathbf{i}_z)\otimes(\rho'(z)\mathbf{i}_r(\theta)+\mathbf{i}_z)\\ &+\mathbf{n}_0(\tilde{\theta},\tilde{z})\otimes\mathbf{n}_0(\theta,z)\end{aligned} \tag{4.8}$$

and $g(t)^{GBE}$ is slightly different from $g(t)^{VFI}$ and $g(t)^{CF}$. In fact, even if in reality the GBE starts while the process of invagination of the ventral furrow is still taking place, here we assume that the convergent-extension movement begins once the VFI has completed. Thus we set $t_{min}^{GBE} = t_{MAX}^{VFI} = 0.007$ while the cephalic furrow completes its formation at $t_{MAX}^{CF} = 0.001$ and $t_{MAX}^{GBE}$ has been found at $t = 0.02$.

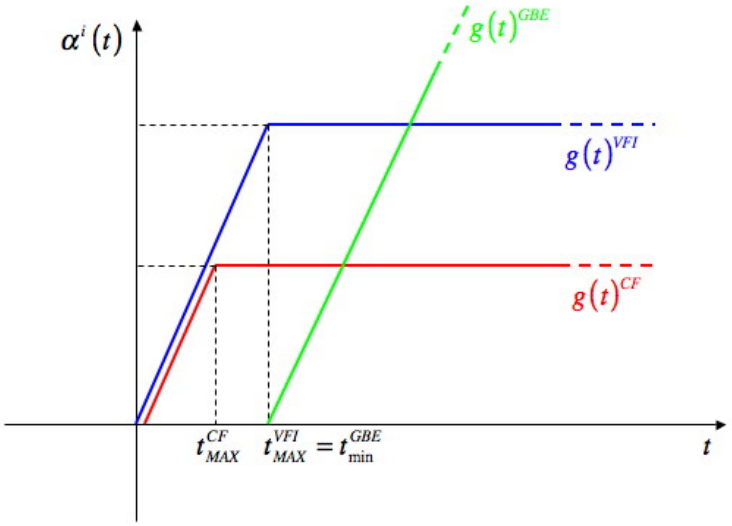


*Figure 4.4:* The furrows start their formation at $t = 0$; the cephalic furrow stops earlier ($t_{MAX}^{CF} = 0.001$) and once the ventral furrow has completed formed ($t_{MAX}^{VFI} = t_{min}^{GBE} = 0.007$), the germ band begins to elongate and will stop at $t = 0.02$.

As mentioned earlier, for this specific case we have assumed that the cells involved firstly in the ventral furrow invagination process are later interested by the convergent-extension movement. Therefore, when superposing the relative active regions, we obtain this time two intersection: again for the ventral and the cephalic

furrow and now also for the ventral furrows and the germ band extension (Fig. 4.5).

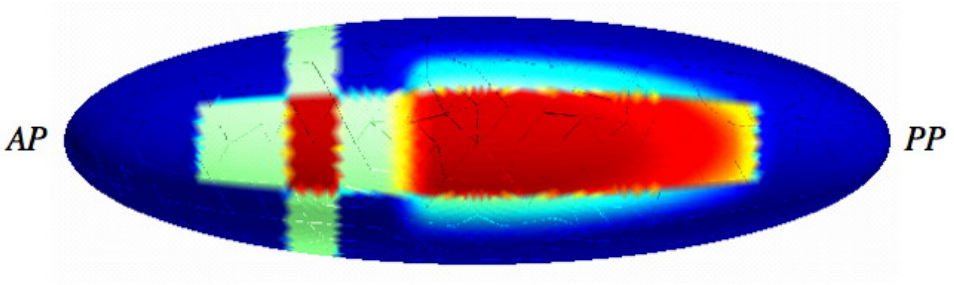


*Figure 4.5:* Ventral view of the embryo. The three active regions are represented (light green: VFI and CF, light blue: GBE); in red the relative intersections.

If for the ventral and the cephalic furrows, the maximal apical constrictions for each cell are very similar to the ones found for the previous concurrent simulation, respectively $\cong 5\mu m$ along the cross section and $\cong 4\mu m$ along $z$, we can not state the same for the germ band extension. In fact for $t^{GBE}_{MAX} = 0.02$ we obtain an elongation of about $2.5 \cdot 10^{-2}\mu m$ and a shortening of $2 \cdot 10^{-2}\mu m$. This is probably due to the fact that the cells in the ventral region of the embryo, that are completely internalized and apically deformed by now, are not able anymore to undergo the same convergent-extension movement as observed during the individual simulation. Such peculiar aspect constitutes an important limitation for our model and it is possible to notice it if we observe the successive phases of the simulation shown in Fig. 4.6. The formation of the two furrows is clearly evident as for the individual simulations; the GBE instead is not so pronounced, except at the posterior pole where a beginning of a vortex movement is noticeable. Furthermore the presence of the cephalic furrow toward the anterior pole seems to highly inhibit the extension of the tissues. We remark also the fact that the ventral furrow, which is supposed to stop its invagination at $t^{VFI}_{MAX} = 0.007$, seems to keep internalizing (Fig. 4.6f), probably triggered by the convergence of the cells involved in the elongation of the germ band.

In order to sort out such inconveniences, we propose two different solutions. The first one concerns the active deformation region for the GBE. So far we have considered that most of the cells involved in ventral furrow invagination, are successively deformed by the convergent-extension movement (Fig. 4.5), however in reality such cells, that completely internalized, later spread through the yolk so that a new tissue forms. Therefore it seems to us that a new population of cells, still affected but more slightly by the previous elementary deformations, undergoes the extension of the germ band. Since it would be too difficult to numerically simulate the closure

of the ventral furrow, we could imagine that the active region for the GBE is constituted by those cells that, at the onset of gastrulation, were placed dorso-laterally and now, once the furrow has formed, probably pulled by the invagination itself, are placed latero-ventrally. Even if not totally realistic, this solution could be useful to obtain the concurrent simulation.

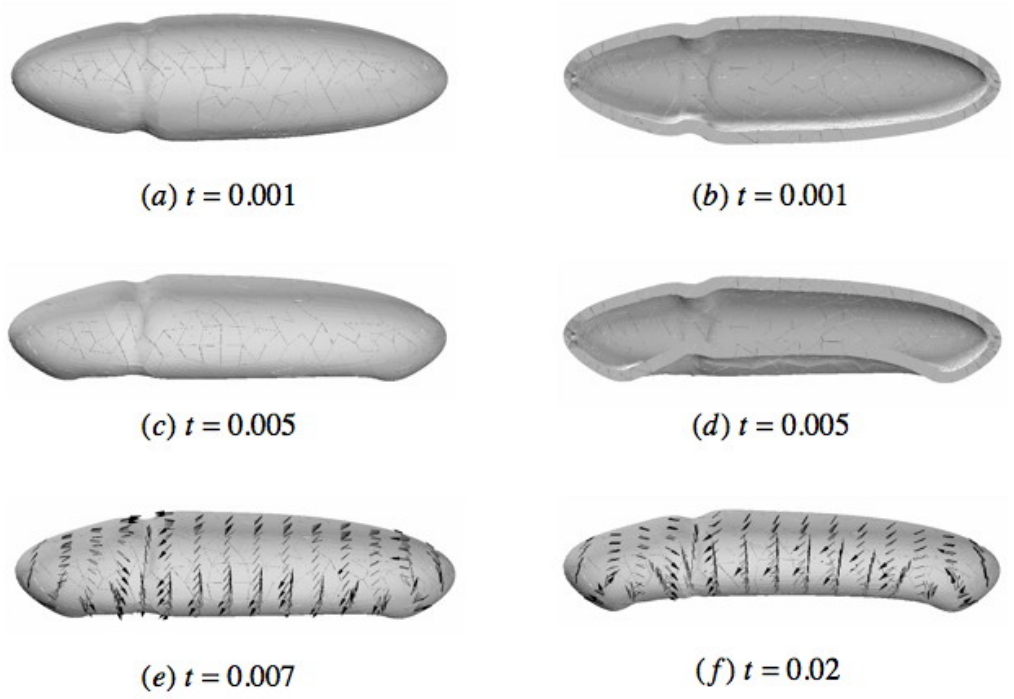


*Figure 4.6:* Successive phases of the concurrent simulation for the three morphogenetic movements. (a) Frontal view of the embryo at $t_{MAX}^{CF} = 0.001$, when the cephalic furrow has formed and the ventral furrow starts to invaginate (b) Cross sectional view at $t_{MAX}^{CF} = 0.001$ (c) Frontal view of the embryo when the furrow has almost completely internalized ($t = 0.005$) (d) Cross sectional view at $t = 0.005$ (e) At $t_{MAX}^{VFI} = t_{min}^{GBE} = 0.007$ the extension of the germ band starts; we notice a beginning of the tissue elongation at the posterior pole (f) The simulation finishes at $t = 0.02$. The ventral furrow has invaginated more, probably triggered by the convergence movement of the GBE, which is still not so evident except at the posterior pole (The black arrows indicate the displacements field).

Nevertheless, it is necessary to take into account that, when the GBE starts, the initial configuration has changed and it needs therefore to be recalculated. Furthermore, the initial regular geometry representing the embryo, is not an ellipsoid anymore so that the parametrical description has to be adapted. For this reason we propose a second solution consisting in introducing an "updated" Lagrangian formulation that allows to decompose the total deformation into several intermediary steps, so that the reference configuration is updated, as for the case of a Eulerian formulation. In the next section we are going to analyze more in detail this new approach.

## 4.2 Updated Lagrangian formulation

This method is very similar to the one used by Sidoroff (Sidoroff [1976]) to define the behaviour of a visco-elastic material. He demonstrated that the greater the number of the internal variables, the more accurate and rigorous the description of a real material. The approach fits very well for our specific case since allows us to introduce the germ band extension on a configuration modified by the formation of the two furrows, the ventral and the cephalic ones.

### 4.2.1 Kinematic description

Let us analyze the scheme proposed in Fig. 4.7. The total deformation $\mathbf{F}$ is decomposed into several intermediate steps that, from the initial undeformed position $\mathbf{p}$ of a generic material point (as defined in Eq. [3.4]), lead to the final configuration $\mathbf{x}_2$ corresponding to the final shape after the three morphogenetic movements have taken place. Practically we have two main phases:

- the first one when the elementary cell deformations triggering the formation of the two furrows are applied; the incremental parameter $t$ runs from $t_0$ to $t_1$. From $\mathbf{p}$ we pass to $\mathbf{x}_1$ through $\mathbf{F}_1$, which can be written as

$$\mathbf{F}_1 = \mathbf{D}_{\mathbf{p}}\mathbf{x}_1 = \mathbf{F}_{m_1}\mathbf{F}_{a_1} = \mathbf{D}_{\bar{\mathbf{x}}_1}\mathbf{x}_1\mathbf{D}_{\mathbf{p}}\bar{\mathbf{x}}_1 \tag{4.9}$$

  with $\mathbf{F}_{a_1}$ and $\mathbf{F}_{m_1}$ the further active and the passive deformation gradients respectively;

- the second phase corresponds to the extension of the germ band, which is introduced considering $\mathbf{x}_1$ the new reference position (here $t$ runs from $t_1$ to $t_2$). So, if previously the initial configuration corresponded to $\mathbf{p}$, now we have $\mathbf{x}_1 = \mathbf{p} + \mathbf{u}_1$, where $\mathbf{u}_1$ is the displacement during the first phase. As for the first part, we can write

$$\mathbf{F}_2 = \mathbf{D}_{\mathbf{x}_1}\mathbf{x}_2 = \mathbf{F}_{m_2}\mathbf{F}_{a_2} = \mathbf{D}_{\bar{\mathbf{x}}_2}\mathbf{x}_2\mathbf{D}_{\mathbf{x}_1}\bar{\mathbf{x}}_2 \tag{4.10}$$

where here again $\mathbf{F}_{a_2}$ and $\mathbf{F}_{m_2}$ are the active and the passive deformation gradients. The main idea is that now the subsequent cell deformations occur relative to the new deformed shape and not to the initial one anymore.

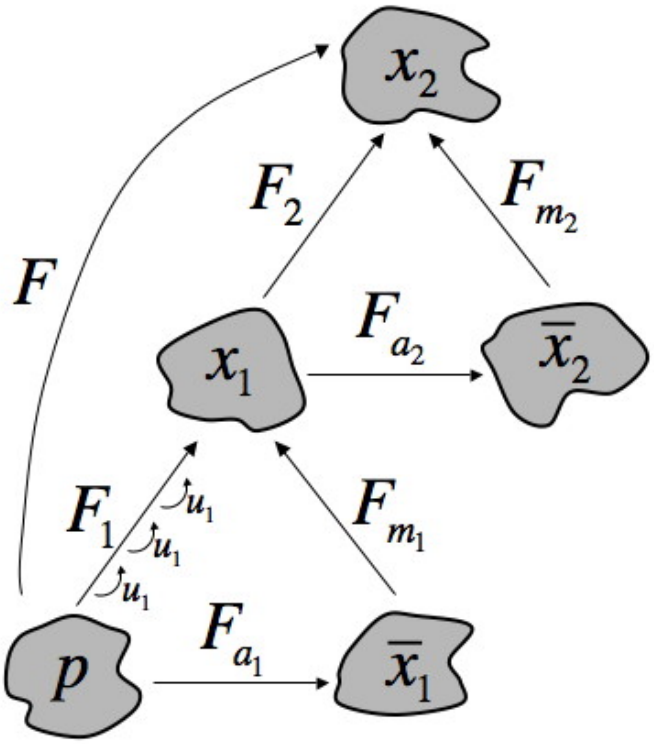


*Figure 4.7:* The gradient decomposition method when more than two movements are simulated. At the end of the first phase the displacement $\mathbf{u}_1$ is saved so that the reference configuration for the second phase become $\mathbf{x}_1 = \mathbf{p} + \mathbf{u}_1$.

The total deformation of the mesoderm can therefore be expressed as follows

$$\mathbf{F} = \mathbf{D}_{\mathbf{p}}\mathbf{x}_2 = \mathbf{F}_2\mathbf{F}_1 \tag{4.11}$$

It has to be noticed that, in applying the elementary cell deformations, we followed the temporal succession of the events, which provides in order the formation of the cephalic and ventral furrows and subsequently the convergent-extension movement of the tissues at the germ band region. Additionally, we have again for this simulation a multiplicative decomposition, but this time each factor itself is the composition of an active and a passive contributions.

**First phase**

We are now going to focus on the first part of the simulation. Given the considerations made in the previous chapter, only apical constriction is introduced along the section and the horizontal axis of the embryo, in order to get respectively the ventral and the cephalic furrows. Any point $\mathbf{p}$ at the initial configuration is defined as in Eq.[3.4]; the intermediate configuration $\bar{\mathbf{x}}_1$ can be written as

$$\bar{\mathbf{x}}_1 = \rho(\bar{z}_1)\mathbf{i}_r(\bar{\theta}_1) + \bar{z}_1\mathbf{i}_z + \zeta\bar{\mathbf{n}}_1(\bar{z}_1, \bar{\theta}_1) \tag{4.12}$$

with $\zeta$ the distance between the generic point $\mathbf{p}$ and its projection $\mathbf{p}_0$ on the middle surface (Eq. [3.2]), along the normal vector $\mathbf{n}_0(\theta, z)$ (Eq. [3.5]). $\bar{\mathbf{n}}_1(\bar{z}_1, \bar{\theta}_1)$ is the normal vector to the intermediate position $\bar{\mathbf{x}}_1$ and is equal to

$$\bar{\mathbf{n}}_1 = \frac{\mathbf{i}_r(\bar{\theta}_1) - \rho'(\bar{z}_1)\mathbf{i}_z}{\sqrt{1+\rho'(\bar{z}_1)^2}} \tag{4.13}$$

$\bar{\theta}_1$ and $\bar{z}_1$ are defined as in Eq. [3.16] and [3.20] as follows

$$\begin{aligned} \bar{\theta}_1 &= \theta + \alpha^{ac}(t)\frac{2\zeta}{h}m(\theta) \\ \bar{z}_1 &= z + \alpha^{ceph}(t)\frac{2\zeta}{h}m(z) \end{aligned} \tag{4.14}$$

where $\alpha^{ac}(t)$ and $\alpha^{ceph}(t)$ are the amplitudes of the elementary deformations and depend on the evolution parameter $t$ (see Chapter 3). Only apical constriction has been implemented since we have demonstrated in Chapter 3 that it is actually the active deformation leading to the invagination of the mesoderm for both the furrows. $h$ is the thickness of the mesoderm and $m(\theta)$ and $m(z)$ are the periodic functions as defined in Eq. [3.17]. The active deformation gradient $\mathbf{F}_{a_1}$ can be directly deduced from Eq. [3.6], so that we obtain

$$\begin{aligned}\mathbf{F}_{a_1} =& \frac{\left[1+\alpha^{ac}(t)\frac{2\zeta}{h}m'(\theta)\right]\bar{\varphi}_{1\theta}}{\varphi_\theta}\mathbf{i}_\theta\left(\bar{\theta}_1\right)\otimes\mathbf{i}_\theta(\theta)\\ &+\frac{\left[1+\alpha^{ceph}(t)\frac{2\zeta}{h}m'(z)\right]\bar{\varphi}_{1z}}{\varphi_z\left(1+\rho'^2(z)\right)}\left[\rho'\left(\bar{z}_1\right)\mathbf{i}_r\left(\bar{\theta}_1\right)+\mathbf{i}_z\right]\otimes\left(\rho'(z)\mathbf{i}_r(\theta)+\mathbf{i}_z\right)\\ &+\left[\bar{\varphi}_{1\theta}\frac{2\alpha^{ac}(t)}{h}m(\theta)\mathbf{i}_\theta\left(\bar{\theta}_1\right)+\bar{\varphi}_{1z}\frac{2\alpha^{ceph}(t)}{h}m(z)\left(\rho'\left(\bar{z}_1\right)\mathbf{i}_r\left(\bar{\theta}_1\right)+\mathbf{i}_z\right)\right.\\ &\left.+\bar{\mathbf{n}}_1\left(\bar{\theta}_1,\bar{z}_1\right)\right]\otimes\mathbf{n}_0(\theta,z)\end{aligned} \tag{4.15}$$

where $\varphi_\theta$ and $\varphi_z$ are the ones of Eq. [3.12], while $\bar{\varphi}_{1\theta}$ and $\bar{\varphi}_{1z}$ are

$$\begin{aligned}\bar{\varphi}_{1\theta} &= \left[\rho\left(\bar{z}_1\right)+\frac{\zeta}{\sqrt{1+\rho'^2\left(\bar{z}_1\right)}}\right]\\ \bar{\varphi}_{1z} &= \left[1-\frac{\zeta\rho''\left(\bar{z}_1\right)}{1+\rho'^2\left(\bar{z}_1\right)^{(3/2)}}\right]\end{aligned} \tag{4.16}$$

**Second phase**

Once the two furrows have formed, we can implement the convergent-extension movement, which provides the second and final configuration of the entire system $\mathbf{x}_2$. However, we have to take into account the fact that the new embryo geometry does not correspond to an ellipsoid anymore, therefore we consider it as a general shell on which we apply the further elementary strains triggering the germ band extension. In Fig. 4.8 we show the typical active deformations applied on a cell, which could be placed at the intersection of the VFI and GBE active regions, that is therefore apically constricted at $t_1$ along $\psi^2$. Similar considerations could be done for a cell at the intersection of the CF and GBE active regions, even if in that case the cell would be apically constricted along $\psi^1$.

Let us call $\mathbf{x}_{1_0}[\psi^1(\theta),\psi^2(z)]$ all the points on the deformed middle surface of the mesoderm, with $\psi^1$ and $\psi^2$ the variables of the new system of curvilinear coordinates and depend on $\theta$ and $z$. Since the active deformations are still defined with respect to the middle surface, we need to calculate the "updated" reference position of any point $\mathbf{x}_1[\psi^1(\theta),\psi^2(z),\zeta^1(\zeta)]$ through the thickness of the mesoderm as follows

$$\mathbf{x}_1(\psi^1,\psi^2,\zeta^1)=\mathbf{x}_{1_0}(\psi^1,\psi^2)+\zeta^1\mathbf{n}_{1_0}(\psi^1,\psi^2) \tag{4.17}$$

where $\zeta^1$ is the distance between $\mathbf{x}_1$ and $\mathbf{x}_{1_0}$ along the normal $\mathbf{n}_{1_0}(\psi^1,\psi^2)$ passing by $\mathbf{x}_1$ to the middle surface (Fig. 4.9).

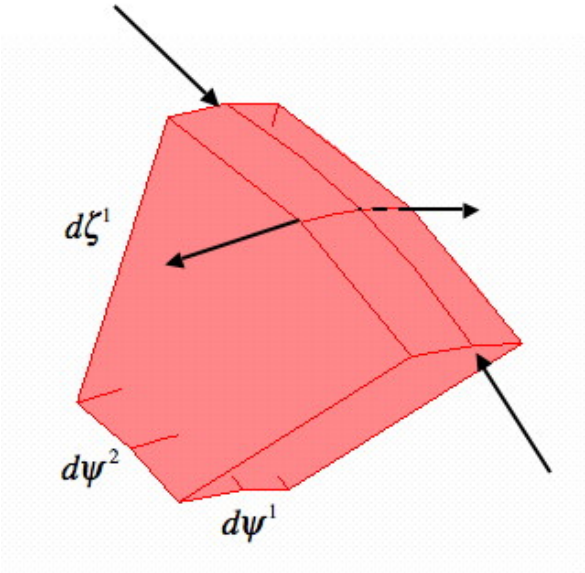


*Figure 4.8:* Convergence-extension movement on a cell that is apically constricted along $\psi^2$.

When applying the convergence from the dorsal to the ventral region of the embryo, therefore along $\psi^2$, and the extension along the anterior-posterior axis, therefore along $\psi^1$, the intermediate position $\bar{\mathbf{x}}_2$ can be expressed as

$$\bar{\mathbf{x}}_2 = \mathbf{x}_{1_0}(\bar{\psi^1}, \bar{\psi^2}) + \zeta^1 \mathbf{n}_{1_0}(\bar{\psi^1}, \bar{\psi^2}) \tag{4.18}$$

where

$$\begin{aligned} \bar{\psi^1} &= (1 + \alpha_z^{GBE}(t))\psi^1 \\ \bar{\psi^2} &= (1 + \alpha_\theta^{GBE}(t))\psi^2 \end{aligned} \tag{4.19}$$

with, once again, $\alpha_\theta^{GBE}(t)$ and $\alpha_z^{GBE}(t)$ are the amplitudes of the active deformations, as defined in Chapter 3. As previously mentioned, by the formation of the two furrows, the embryo is not an ellipsoid anymore; thus the expression of the intermediate position $\bar{\mathbf{x}}_2$ can not correspondingly be calculated. Therefore, we rather proceed in the following way. The initial middle surface is obtained by its CAD representation (patches of Béziers surfaces) and the initial normal $\mathbf{n}_0(\psi^1, \psi^2)$ is computed over it. The deformed surface at $t_1$ is numerically obtained and its relative unit normal is given by

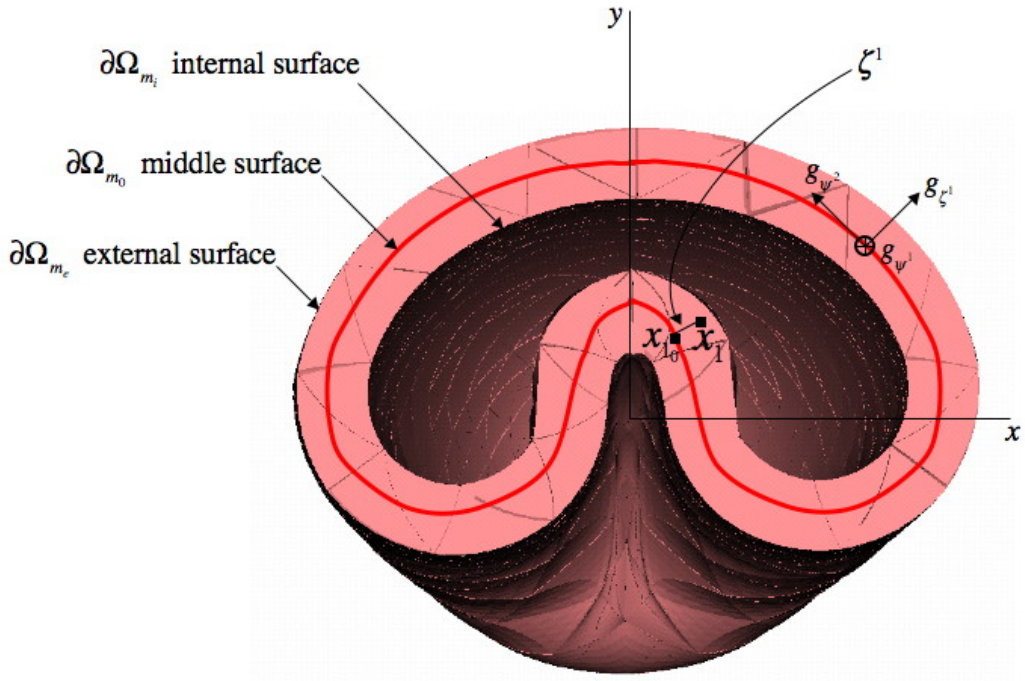


*Figure 4.9:* Cross-sectional view of the embryo at the end of the first phase ($z = 0, t = t_1$).

$$\mathbf{n}_{1_0}(\psi^1,\psi^2) = \frac{\mathbf{F}_1^{-T}\left[\mathbf{n}_0(\psi^1,\psi^2)\right]}{\|\mathbf{F}_1^{-T}\left[\mathbf{n}_0(\psi^1,\psi^2)\right]\|} \tag{4.20}$$

This normal is extended through the thickness of the mesoderm at the same position, so that the full kinematic supplied by Eq.[4.18] can be formulated.

The active deformation gradient $\mathbf{F}_{a_2}$ in the "updated" curvilinear system can be classically obtained as

$$\mathbf{F}_{a_2} = \frac{\partial\bar{\mathbf{x}}_2}{\partial\psi^1}\otimes\boldsymbol{\nabla}_{\mathbf{x}_1}\psi^1 + \frac{\partial\bar{\mathbf{x}}_2}{\partial\psi^2}\otimes\boldsymbol{\nabla}_{\mathbf{x}_1}\psi^2 + \frac{\partial\bar{\mathbf{x}}_2}{\partial\zeta^1}\otimes\boldsymbol{\nabla}_{\mathbf{x}_1}\zeta^1 \tag{4.21}$$

The vectors

$$\begin{aligned}\boldsymbol{\nabla}_{\mathbf{x}_1}\psi^1 &= \frac{\mathbf{g}_{\psi^2}\wedge\mathbf{g}_{\zeta^1}}{g}\\ \boldsymbol{\nabla}_{\mathbf{x}_1}\psi^2 &= \frac{\mathbf{g}_{\zeta^1}\wedge\mathbf{g}_{\psi^1}}{g}\\ \boldsymbol{\nabla}_{\mathbf{x}_1}\zeta^1 &= \frac{\mathbf{g}_{\psi^1}\wedge\mathbf{g}_{\psi^2}}{g}\end{aligned} \tag{4.22}$$

form the new *contravariant* basis, with $g$ defined as in Eq.[2.15]. $\mathbf{g}_{\psi^1}, \mathbf{g}_{\psi^2}, \mathbf{g}_{\zeta^1}$ are instead the new tangent vectors when $\zeta^1 \neq 0$ and they are expressed as

$$\begin{aligned}\mathbf{g}_{\psi^1} &= \frac{\partial \mathbf{x}_1}{\partial \psi^1}\\ \mathbf{g}_{\psi^2} &= \frac{\partial \mathbf{x}_1}{\partial \psi^2}\\ \mathbf{g}_{\zeta^1} &= \frac{\partial \mathbf{x}_1}{\partial \zeta^1}\end{aligned} \tag{4.23}$$

Actually, such tangent vectors can be expressed in function of the initial tangent vectors at $t_0$, numerically computed in the new system of curvilinear coordinates $(\psi^1, \psi^2, \zeta^1)$. Thus, they can be rewritten as follows

$$\begin{aligned}\mathbf{g}_{\psi^1} &= \mathbf{F}_1(\mathbf{g}_{0_{\psi^1}}) = \mathbf{F}_1\frac{\partial \mathbf{p}(\psi^1,\psi^2,\zeta^1)}{\partial \psi^1}\\ \mathbf{g}_{\psi^2} &= \mathbf{F}_1(\mathbf{g}_{0_{\psi^2}}) = \mathbf{F}_1\frac{\partial \mathbf{p}(\psi^2,\psi^2,\zeta^1)}{\partial \psi^2}\\ \mathbf{g}_{\zeta^1} &= \mathbf{F}_1(\mathbf{g}_{0_{\zeta^1}}) = \mathbf{F}_1\frac{\partial \mathbf{p}(\psi^1,\psi^2,\zeta^1)}{\partial \zeta^1}\end{aligned} \tag{4.24}$$

and Eqs. 4.22 become

$$\begin{aligned}\boldsymbol{\nabla}_{\mathbf{x}_1}\psi^1 &= \mathbf{F}_1^{-T}\left(\nabla_{\mathbf{p}}\theta\right)\\ \boldsymbol{\nabla}_{\mathbf{x}_1}\psi^2 &= \mathbf{F}_1^{-T}\left(\nabla_{\mathbf{p}}z\right)\\ \boldsymbol{\nabla}_{\mathbf{x}_1}\zeta^1 &= \mathbf{F}_1^{-T}\left(\nabla_{\mathbf{p}}\zeta\right)\end{aligned} \tag{4.25}$$

### 4.2.2 The Principle of the Virtual Power and stress updated scheme

As already mentioned, the concurrent simulation proposed in this section is composed by two separated phases (Fig. 4.10):

- the first one starts at $t_0$ and stops at $t_1$, when both the ventral and the cephalic furrows have formed. We calculate $\mathbf{F}$ which corresponds here to $\mathbf{F}_1$;

- the second one runs from $t_1$ to $t_2$, when the process of convergence-extension ends. $\mathbf{F}$ is calculated on the deformed geometry and is the composition of $\mathbf{F}_2$ and $\mathbf{F}_1$, this last one fixed.

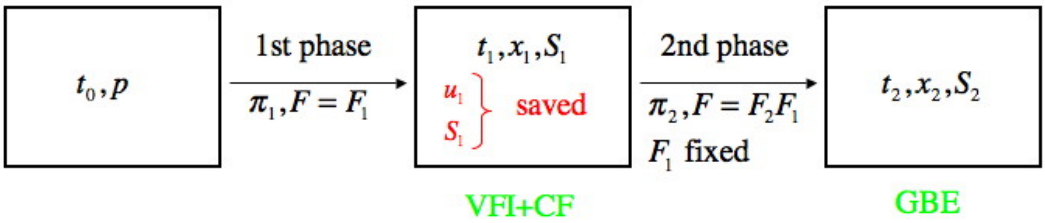


*Figure 4.10:* Successive phases of the updated concurrent simulation.

The Principle of the Virtual Power is still employed. Thus, for the first part, Eq.[2.28] defines the mechanical equilibrium of the system, with the First Piola-Kirchhoff tensor $\boldsymbol{\pi}_1$ expressed as in Eq.[2.34]; the displacements $\mathbf{u}_1$ are saved so that we are able, once the ventral and the cephalic furrows have formed at $t_1$, to obtain the "updated" reference position $\mathbf{x}_1$. Therefore, for the second part of the simulation, not only we will apply the further active deformations on this new and deformed initial configuration, but we will also need to take into account the stresses that have been developed during the first phase. Since the First Piola-Kirchhoff tensors $\boldsymbol{\pi}_1$ and $\boldsymbol{\pi}_2$ can not be added because defined over two configurations, we must consider the Second Piola-Kirchhoff tensors $\mathbf{S}_1$ and $\mathbf{S}_2$ that are referred to only one configuration.

In order to do so, as similarly as for the displacements, we save at $t_1$ the Second Piola-Kirchhoff tensor $\mathbf{S}_1$, which is equal to

$$\mathbf{S}_1 = J_{a_1} \mathbf{F}_{a_1}^{-1} \mathbf{S}_{m_1} \mathbf{F}_{a_1}^{-T} \tag{4.26}$$

with $J_{a_1}$ the determinant of $\mathbf{F}_{a_1}$ and $\mathbf{S}_{m_1}$ the Second Piola-Kirchhoff tensor relative to the intermediate configuration of the first phase. For the second phase instead, we have

$$\mathbf{S}_2 = J_{a_2} J \left(\mathbf{F}_{a_2} \mathbf{F}_1\right)^{-1} \mathbf{S}_{m_2} \left(\mathbf{F}_{a_2} \mathbf{F}_1\right)^{-T} \tag{4.27}$$

with $J_{a_2}$ the determinant of $\mathbf{F}_{a_2}$ and $\mathbf{S}_{m_2}$ the Second Piola-Kirchhoff tensor relative to the intermediate configuration of the second phase.

Therefore $\boldsymbol{\pi}_2$ is still expressed as in Eq.[2.29], but this time we have

$$\boldsymbol{\pi}_2 = \mathbf{F}\,(\mathbf{S}_1 + \mathbf{S}_2) \tag{4.28}$$

It has to be noticed that, for both the first and the second phases, the boundary conditions do not change since they are defined with respect to the very initial configuration; therefore their expression is the sames as in Eq.[2.28].

## 4.3 Conclusions

In this chapter we propose the concurrent simulation of the three morphogenetic movements that have been individually obtained in Chapter 3.

In the first part a preliminary tentative is proposed. The method used is the most intuitive since it allows to couple the events, following their chronological succession, by simply multiplying the active deformation gradients; therefore no further manipulations of the single formulation are required. Two simulations are shown: the first one allows to reproduce the formation of the two furrows, for the second one also the germ band extension is introduced. If in the first case the results are consistent and interesting, for the second one some limitations are observed. In particular, we notice that the convergent-extension movement is not so pronounced compared to the individual simulation; this is probably due to the fact that the cells involved in this process have already been deformed by the elementary forces triggering the ventral and the cephalic furrows. Additionally, the embryo geometry, once the two furrows have completely formed, is not an ellipsoide anymore, thus the reference configuration with respect to which the germ band extension is applied has changed too. A more accurate and reliable approach is necessary.

In the second part of the chapter we amply describe the theory of a new "updated" Lagrangian formulation, which allows to take into account the two important aspects previously pointed out. Specifically, the total deformation is decomposed into several steps so that the reference configuration is constantly updated; two main phases are contemplated. During the first one the two furrows are obtained and the analytical formulation of the active deformation gradient directly couple together the elementary forces triggering the two movements. During the second one the germ band is observed; the initial geometry at the beginning of this phase has changed, thus a new curvilinear system is introduced and both the convergence and the extension of the tissues are applied. Even though the results for this second essay are still in progress, we think that the new approach represents one of the major perspective of the present work. Firstly because of the accuracy in the geometrical description that rarely has been so detailed; secondly because we will be able to provide a very

realistic representation of part of the gastrulation process, with the most important events simulated. Neverthelss, the main difficulty in setting up this simulation is due to the complexity of the several changes in shape undergone by the tissues and furthermore by the fact that they are perfectly synchronized in the real embryo.

# Chapter 5

# Conclusions and perspectives

In this work we present a three dimensional finite element model of the *Drosophila* embryo by which we reproduce part of the gastrulation, one of the most important phases of the developmental process. If the approach used has often been employed for similar studies and therefore largely known in mechanics, we think on the other hand that the results obtained here can be considered rather original for two principal reasons. First of all, with a single model we are able to simulate three morphogenetic movements that induce important shape changes of the embryonic tissues; specifically ventral furrow invagination, cephalic furrow formation and germ band extension. We can provide both the individual simulation of the main events and the concurrent simulation by two or three of them, which constitutes the most innovative feature of our work. Secondly, not only we have confirmed most of the hypotheses put forward by biologists, but we have also found new hints of discussions that may lead to new interpretations of the problem; therefore our model can be considered a very useful tool for further analyses.

In the first chapter we have proposed a general overview of the *Drosophila* embryogenesis so that the major events are traced and the relevant aspects are pointed out. In particular we have focused on the strong connection between genetics and mechanics that has actually been observed for long time in *in vivo* studies. Each one of the morphogenetic movement considered here is controlled by specific genes that exert then an important influence on the elementary forces acting on the cells. Only recently also the inverse process has been detected; it seems in fact that a certain number of mechanical deformations occurring to the tissues may favour the expression of genes at different spots than the usual ones. However, it is still unclear how the mechanical stimuli are transformed into chemical signals, so that such phenomenon, better known as mechanotransduction, remains enigmatic. In this section of the work we also provide a brief review on previous works that have been found in literature. Most of them allow to reproduce the invagination of the ventral furrow and the convergent-extension of the cells, while, to the best of our knowledge, none

consents to simulate the formation of the cephalic furrow that is instead presented here. The first models are constituted of structural elements, usually trusses or bars, that play the role of actuators to reproduce the cytoskeleton components (i.e. microtubules and microfilaments). In despite of this, many of them do not take into account external components to the epithelial layer such as the yolk, which fills the internal cavity, and the vitelline membrane that surrounds the embryo. This is their main drawback since the absence of one or both of these components may engender final configurations that do not match with experimental observations. Also it has to be noticed that the embryo has often been represented in a two dimensional space which does not assure a realistic reproduction of the biological system. Few recent works provide three dimensional models of ventral furrow invagination; the embryo is described as a continuum on which the active and the passive forces acting on the cells, that are strongly related, are applied. So far then, the models are specific to a single event, while here we show how the analytical formulation can be modified and adapted so that more than one movement can be simulated.

A gradient decomposition method is used and it is exhaustively described in the second chapter. This method allows to take into account both the active and the passive contributions; the former corresponds to the natural tendency of the cells to deform as if they were completely free, which can lead to geometrical incompatibilities. Therefore the latter occurs, a consequent response of the tissues in order to guarantee the continuity of the system. Different interpretations of the approach can be contemplated, as amply discussed in this section; in particular we propose a comparison with an equivalent thermal dilatation and we analyze the potential effects of the local active forces on both the active and passive domains and in particular at the internal and external cellular interfaces. The mechanical equilibrium is expressed by the Principle of the Virtual Power so that the internal forces are included together with the yolk pressure and the contact between the mesoderm and the vitelline membrane. We have also treated here the choice of the material describing the mesoderm, which is assumed to constitute the most part of the embryonic tissues. Given the very few information about the mechanical characteristics required here, that are often difficult to detect, we have opted for a linear Saint-Venant constitutive law, which does not take into account the non linearities engendered by the visco-elastic properties of the embryonic tissues, but may be anyway a useful tool for a first qualitative analysis of the problem. Nevertheless, aware of such limitations, we have compared our model to the Hyperelastic one, which has normally been employed in previous studies.

Chapter three focuses on the analysis of each morphogenetic movement and the relative results. In the first part we describe how the analytical expressions of the active deformation gradients are obtained, according to the elementary cell deformations introduced. Such formulations, coupled with the passive gradients, will be implemented in the Principle of the Virtual Power, together with the boundary conditions of the system, in order to get the final tissues deformation. In the second

part of the chapter we analyze the results for each morphogenetic movement; for the three events the agreement with the experimental observations is rather consistent, thus most of the hypotheses made by biologists are confirmed. Additionally we have been able to put forward some new aspects which may lead to interesting conclusions and therefore further hints of discussion. Here we resume the major remarks that can be deduced from the numerical simulations:

- first of all, a parametrical study has been conducted for the ventral furrow, which has pointed out the influence exerted by some variables such as the size of the active deformation region and the dimensions of the material cells. In particular we have observed that, when let varying these parameters, the invagination is almost the same for all the cases, while the phenomenon of the self-contact between the two strips of the mesoderm may be evidently inhibited or enhanced;

- by manipulations on mutants, biologists have individuated only two active forces leading to ventral furrow invagination: apical constriction and apico-basal elongation. Although, for our simulation, we have first implemented only the former and the invagination of the mesoderm still occurs; this allows us to conclude that probably apical constriction is actually the only responsible of the entire process of invagination, while apico-basal elongation, together with the other three elementary deformations detected, are passive responses of the cells. This hypothesis has been also confirmed through the simulation of the cephalic furrow, for which again only apical constriction has been introduced and, even if a small number of cells is involved, the invagination takes place;

- for the germ band extension, the final displacements found for our simulation reproduce pretty well the real convergence-extension of the tissues; in particular we have observed the vortex movements at the anterior and posterior poles, as in the real embryo. Also we have compared the velocity field with experimental data available in literature and they present almost the same trend through the embryo;

- the Hyperelastic constitutive law, amply discussed in the second chapter, has been tested for the simulation of the germ band extension. The results are not so different from the ones obtained with the Saint-Venant model used all long our analysis, which confirms that our first choice, even if presenting some limitations, can anyway be considered appropriate for the present work;

- we have estimated the induced forces, specifically pressures and shear stresses, that may develop through the embryo when the three morphogenetic movements take place. These forces can be compared to the usual ones applied on cells placed in a bioreactor over $24h$ that may engender several cellular activities such as migration, proliferation or adhesion. Most importantly, for the

specific case of the germ band extension we have found that the convergent-extension movement of the tissues actually leads to a compression at the anterior pole which triggers, as observed during experiments, the expression of the gene *twist*, normally expressed at the ventral region of the embryo. This result could confirm the presence of a mechanotransduction pattern by which a mechanical stimuli is transformed into a chemical signal, even at long distance;

- finally, aware that the geometry of our model is a simplification of the real embryo, we have conducted an interesting analysis to evaluate how the variation of the curvature radius may affect the final configuration during ventral furrow invagination and germ band extension. So far three geometries have been tested and other two are in progress in order to take into account two important aspects: the non symmetry with respect to the vertical axis of the embryo, which provides a more rounded posterior pole, and the flattening of the dorsal region.

Given the consistence of the results for the individual simulations of the three morphogenetic movements, we have decided to perform the concurrent simulation of the events, which is the object of the fourth chapter. A preliminary essay is presented which provides a consistent final configuration for the simulation of the two furrows, but some limitations are observed when the germ band extension is introduced. Therefore a second method, more closely related to the observed succession of movements, is proposed. It allows to take into account several peculiar aspects so far put aside, that may instead play a significant role in the global response of the embryo. Even though the results for this second simulation are still in progress and thus not presented here, we think that this part of the work represent one major contribution of the present study, thus an interesting perspective to pursue.

**The mechanical properties of the mesoderm and sensibility analysis**

During development the thin tissues composing the embryo undergo several movements and deformations that are crucial to normal morphogenesis. Thus, it is very important to know the mechanical properties of the embryonic structures which unfortunately so far, compared to orthopaedic or cardiac mechanics, have been very difficult to detect. Actually, if many progresses have been made for measuring the mechanical characteristics of individual cells and bulk tissues, still little has been done to improve methods allowing to obtain information from specimens of embryonic epithelium. These data play a significant role in biomechanics and especially in embryogenesis, where materials can exhibit elastic, visco-elastic, viscous or plastic properties and the consequences of these differences may be substantial for morphogenetic movements. Our model, as many among the previous ones, is based on several approximations concerning such properties, so that its validation may appear uncertain. Therefore, in order to refine this key aspect so far rarely

explored in numerical simulations, we would like to introduce a visco-elastic model to describe the mesoderm, which must then be supported by experimental observations. Nonetheless, if on one hand it is essential to determine the right mechanical characteristics of the tissues in order to obtain consistent results, on the other it would be equally interesting to perform a sensibility analysis, which will allow to evaluate the influence of specific parameters, such as the Young's modulus, on the final configurations relative to each morphogenetic movement.

**Cephalic furrow simulation**

For the cephalic furrow simulation a few simplifications have been made. Actually, by experimental movies, it has been observed that the furrow starts vertically, at about 60% of the horizontal length of the embryo, but, throughout its formation, it is pushed, probably triggered by the extension of the germ band, toward the anterior pole. Thus, at the final configuration, once the cells in the active region have completely internalized, the furrow is inclined at about 30° with respect to the dorsal-ventral axis; the cells apically constrict and simultaneously skew, so that their curvilinear coordinate $\theta$ changes too. For the present work we have decided to model the furrow parallel to the vertical axis of the embryo, without taking into account its movement during the invagination process. The next step would be to implement an Eulerian formulation which will provide the expression of the intermediate position $\bar{\mathbf{x}}$ that will include both the deformation of the cells along the cross section and the displacement of the tissues associated to a determined velocity.

**From the embryo to the single cell**

In the present work, the mesoderm is represented as a continuum on which the elementary forces, that trigger the different morphogenetic movements, are applied. We use then a macro-scale approach of the problem, whereas the active deformations involve the membranes of the cells that compose the embryonic tissue at a micro-scale level. Nevertheless our model provides the useful tools to perform a more detailed analysis, where each cell will be described including some of its essential components such as the nucleus, the micro filaments and other elements of the cytoskeleton. In this way, we will be able to test also other types of strain, such pressure and shear stress, to which cells in culture or bioreactor are usually submitted to.

# Appendix A

# Large deformation theory

All biological tissue can in general undergo large deformation in physiological activity. Large deformation is typically defined as anything greater 3 to 5 % strain. When the deformation is small, we can use the small deformation linear strain tensor and the Cauchy stress tensor. However, once deformations exceed 5% strain, we must use the appropriate stress and strain tensor, constitutive relations that account for large deformations.

## A.1 The deformation gradient tensor

The first step in defining large deformation strain measures is to determine the relationship between what is known as the reference, initial or undeformed configuration and the deformed configuration of a body. The reference, initial or undeformed configuration is the condition of the body in a 3D space before loads and constraints have been applied to it. The deformed configuration is the location and the shape of the body after loads have been applied to it. Obviously the body can undergo rigid body motions in addition to strain when loads are applied to it. An illustration of the relationship between the initial and deformed configuration is shown below.

We defined two different vectors: one in the reference configuration $\mathbf{p}$ and one for the deformed configuration $\mathbf{x}$. The relationship between the two position vectors is the displacement vector.

By vector addition, we can directly write the equation defining it:

$$\mathbf{x} = \mathbf{p} + \mathbf{u} \tag{A.1}$$

If we consider the vectors describing material orientation in each configuration, these vectors essentially describe an infinitesimal piece of material of the body. We will note these vectors as $d\mathbf{p}$ in the reference configuration and $d\mathbf{x}$ in the deformed configuration and so, applying the chain rule, we obtain a mapping between the

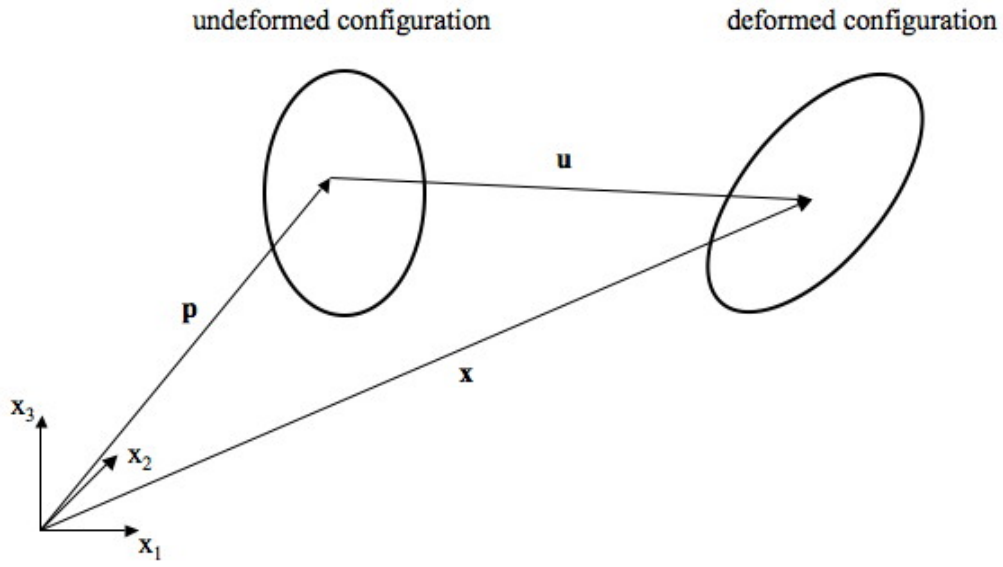


*Figure A.1:* Undeformed and deformed configurations.

material orientation vector in the initial and the deformed configuration:

$$d\mathbf{x} = \frac{\partial \mathbf{x}}{\partial \mathbf{p}} d\mathbf{p} \tag{A.2}$$

and let us define the deformation gradient tensor as:

$$\mathbf{F} = \frac{\partial \mathbf{x}}{\partial \mathbf{p}} \tag{A.3}$$

By the rules of index notation, we know that $\mathbf{F}$ is a second order tensor since it has two independent indices and it is not symmetric. Let us take into consideration the displacement equation (Eq.[A.1]), so that the deformation gradient defined in Eq.[A.3] can be written as

$$\mathbf{F} = \mathbf{I} + \frac{\partial \mathbf{u}}{\partial \mathbf{p}} \tag{A.4}$$

Because **F** is a one to one mapping from the undeformed to the deformed configuration, then the inverse mapping must exists ($\mathbf{F}^{-1}$). The following relationships involving **F** are useful since they allow us to map the area and the volume between the undeformed and the deformed configurations. If we map a volume, using the 3rd invariant or determinant of the deformation gradient tensor, we have:

$$dV_x = det\mathbf{F}\, V = JdV \tag{A.5}$$

For the area, considering the drawings of area change given in Fig. A.2.

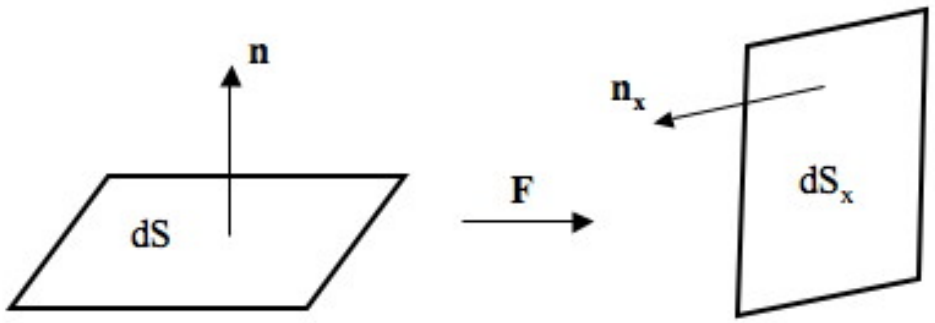


*Figure A.2:* Differential area element before and after deformation.

The mapping between the two configurations is (Smith [1993], Taber [2004]):

$$\mathbf{n}_x\, dS_x = J\, \mathbf{F}^{-T}\mathbf{n}\, dS \tag{A.6}$$

## A.2 Strain and deformation measures

Although the deformation gradient tensor defined above is one measure of how a body changes under load, it cannot be used directly for strain characterization because it contains rigid body motions. To define a strain measure, we will try to

measure the change in length squared in a material vector in going from the initial configuration to the deformed configuration and these measures should be independent of rigid body rotation. For the reference configuration, the length squared of a vector can be merely written as the dot product with itself:

$$(dS)^2 = dl\, dl \tag{A.7}$$

and the same for the deformed configuration:

$$(dS_x)^2 = dl_x\, dl_x \tag{A.8}$$

A strain measure should be a mapping that tell us how much a piece of material is squeezed when going from one to the other configuration, specifically how length and angle change. Thus for a strain tensor $\mathbf{E}$ we write:

$$(dS_x)^2 - (dS)^2 = dl_x dl_x - dl\, dl = 2\, d\mathbf{p}\, \mathbf{E}\, d\mathbf{p} \tag{A.9}$$

where

$$\mathbf{E} = \frac{1}{2}(\mathbf{F}^T\mathbf{F} - \mathbf{I}) \tag{A.10}$$

We have not made any assumptions about the magnitude of the deformation, so the strain tensor given above is exact for any size deformation and it is known as the Green-Lagrange strain tensor. An often used quantity to define constitutive equations for large deformations, is the Right Cauchy deformation tensor:

$$\mathbf{C} = \mathbf{F}^T\mathbf{F} \tag{A.11}$$

substituting this in Eq.[A.10] we have:

$$\mathbf{E} = \frac{1}{2}(\mathbf{C} - \mathbf{I}) \tag{A.12}$$

This tensor is symmetric and positive definite.

## A.3 Large deformation stress measures

We must now define new stress measures and they have to be appropriate when coupled with the strain measures that we have defined in the previous section. We have already encountered one stress measure, the Cauchy stress tensor; this stress is basically defined as force on unit deformed area. The problem with using the Cauchy stress tensor for analyzing materials undergoing large deformation is that we generally do not know the area in the deformed configuration, thus we need to define a stress measure that we can use in the reference configuration. The first principle used when trying to derive a stress tensor with respect to the reference configuration is that the stress tensor in the reference configuration area should give the same force as the Cauchy stress tensor defined in the deformed configuration. Recalling that the traction is a force on a surface and is the product of the stress and the normal vector to the surface, we can define the total force in the deformed configuration as:

$$d\mathbf{P}_x = \boldsymbol{\sigma}\, \mathbf{n}_x dS_x \tag{A.13}$$

where $d\mathbf{P}_x$ is the total force, $\boldsymbol{\sigma}$ is the Cauchy stress tensor, $\mathbf{n}_x$ is the normal vector to the surface of the deformed configuration, and $dS_x$ is the surface area in the deformed configuration. Noting that we would like the same force developed by the new stress tensor, $\mathbf{T}$, in the reference configuration with normal $\mathbf{n}$ and area $dS_x$, we define:

$$d\mathbf{P}_x = \boldsymbol{\pi}\, \mathbf{n}\, dS \tag{A.14}$$

where $\boldsymbol{\pi}$ is then the 1st Piola-Kirchoff stress tensor. Now recalling the mapping between reference and deformed configuration surface areas, we can write the definition of the force in the deformed configuration as:

$$\boldsymbol{\pi}\, \mathbf{n} dS = \boldsymbol{\sigma}\, \mathbf{n}_x\, dS_x = \boldsymbol{\sigma} J\, \mathbf{F}^{-T}\, \mathbf{n}\, dS \tag{A.15}$$

Now that we have the expressions for the total force consistent in terms of the normal and area, we can substract the two expressions and set the result equal to zero, so that we obtain:

$$\boldsymbol{\pi} = J\, \boldsymbol{\sigma} \mathbf{F}^{-T} \tag{A.16}$$

therefore the 1st Piola-Kirchoff stress gives us the actual force rendered in the undeformed surface area.

The 1st Piola-Kirchoff stress tensor is not symmetric; this makes it more difficult to use with numerical analyses like the finite element method. Furthermore, it is not directly relied to **E**, thus we need to look further for an appropriate stress tensor. An additional step we can take is not to derive a stress tensor based on the force $d\mathbf{P}_x$ in the deformed configuration, but rather map the force $d\mathbf{P}_x$ back into the undeformed configuration using the inverse of the deformation gradient tensor. Doing this we obtain:

$$d\mathbf{P} = \mathbf{F}^{-1} d\mathbf{P}_x \tag{A.17}$$

if we define another stress tensor, **S**, which gives the total force on the area in the undeformed configuration, we obtain:

$$d\mathbf{P} = \mathbf{S}\,\mathbf{n}\,dS \tag{A.18}$$

then

$$d\mathbf{P} = \mathbf{F}^{-1}\boldsymbol{\sigma}\,J\,\mathbf{F}^{-T}\mathbf{n}\,dS \tag{A.19}$$

Now we can compare the third stress tensor **S**, which is the 2nd Piola-Kirchoff stress tensor, to the Cauchy stress tensor as:

$$\mathbf{S} = J\,\mathbf{F}^{-1}\boldsymbol{\sigma}\,\mathbf{F}^{-T} \tag{A.20}$$

The number of indices and different stress tensors being thrown around can be quite confusing; the deformation gradient maps forward to the deformed configuration, while the inverse deformation gradient maps backwards to the initial configuration.

One difficulty with all these stress tensors is how to envision their physical meaning. In truth, the physical meaning of the 2nd PK stress is hard to interpret. It is mainly used as a vehicle to get what is called an objective constitutive equation, after which the Cauchy stress is computed from the 2nd PK stress.

# Appendix B

# Mechanics of growing mass

When talking about tissues, one must distinguish between hard tissues, such as bones and teeth, and soft tissues, such as blood vessels, tendons and ligaments. In contrast with hard tissues, that usually undergo only small deformations and grow by simple deposition on a surface, soft tissues can experience large deformations (see Appendix A) and their growth and remodeling take place during the normal process of growth, healing process or pathological conditions (Asaro and Lubarda [2006]). Generally, the changing processes of a tissue are due to the use of the tissue itself. For instance a cyclical stress leads to the formation of a new bone, while the high blood pressure enhances the remodeling of the heart to obviate the hyperthropy. Therefore, by remodeling and modifying their structure, tissues adapt themself to the loading conditions they are affected to. Taber (Taber [1995]) and Humphrey (Humphrey [1995]) both analyzed the biomechanical aspects of growth, defined as a change in volume, remodeling, a change in properties, and morphogenesis, an isovolumic change in shape and they concluded that the three processes are clearly correlated and overlapped.

To study the growth in plants and animals, many mathematical descriptions have been proposed (see review Taber [1995]), most of which provide an analysis of the problem from a kinematic point of view. It has been observed that, if the growth strains of each element of an unloaded body are geometrically compatible, then the body remains stress-free after the growth occurs. On the other hand when the growth strains are incompatible, a residual stress is generated and it remains after all external loads are removed. Even if in the last decades the residual stress has been largely studied, it is still not clear the purpose of its existence; the main hypothesis is that it could assure a more uniform distribution of the loads through the tissue so that the global structure can better tolerate them. There are essentially two types of growth: the surface growth, which occurs without generation of residual stress and by adding or resorption at a surface and the volumetric growth, which is very similar to thermal expansion.

## B.1 Surface growth

This type of growth usually involves bones, shells, horns and branches. Let us consider this time a surface $S_0$ including two material regions $R_1$ and $R_2$ on each side (Fig. B.1a). Each point of the domain can be located by the surface coordinates $\xi_\alpha$ with $\alpha = 1, 2$. At the initial time $t = 0$, the surface grows from both of its side so that two new regions come to form, $R_3$ and $R_4$ (Fig. B.1b), that push $R_1$ and $R_2$ outward and are separated from them by surfaces $S_1$ and $S_2$.

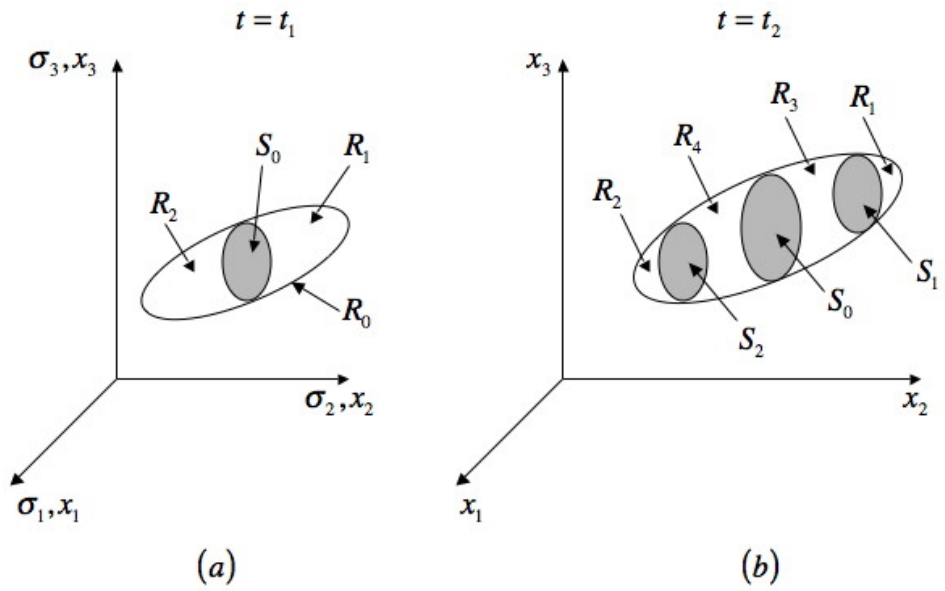


*Figure B.1:* Geometry for the surface growth of a mass (modified from Taber [1995]).

At $t = 0$, each point is located by $\mathbf{x}_0$, but when growth process starts, each point on the surface $S_0$ generates an infinite number of particle in the new regions $R_3$ and $R_4$. An additional time variable $\tau$ is introduced in order to skip out the redundancy of the material coordinates; this new variable provides the time at which each particle has formed so that we can write

$$\mathbf{x} = \mathbf{x}(\xi_\alpha, \tau, t) \tag{B.1}$$

with $0 < \tau < t$. The new surfaces $S_1$ and $S_2$ can be considered the first ones of the new material configuration, so that their points are defined by $\mathbf{x}(\xi_\alpha, 0, t)$, whilst

the position of $S_0$ at any time is $\mathbf{x}(\xi_\alpha, t, t)$. Therefore, the velocities can be written respectively

$$\mathbf{v}_0 = \dot{\mathbf{x}}_0(\xi_\alpha, t) \qquad \text{for a point on } S_0 \tag{B.2}$$

$$\mathbf{v} = \dot{\mathbf{x}}(\xi_\alpha, \tau, t) \qquad \text{for a point on } R_3 \text{ and } R_4 \tag{B.3}$$

The velocity $\mathbf{v}$ adjacent to $S_0$ might differ from the surface velocity $\mathbf{v}_0$ because of the relative growth velocity, which is

$$\mathbf{v}_g = \mathbf{v} - \mathbf{v}_0 \tag{B.4}$$

According to the side of $S_0$ we are considering, the normal component of $\mathbf{v}_g$ to this surface can be either positive in a case of accretion or negative in a case of resorption.

## B.2 Volumetric growth

In the case of volumetric growth, for linear elastic problems, it is possible to superpose the growth stresses, but in non-linear problems it is necessary to use another approach. The strains measured for each material element are referring to the current zero-stress configuration, which changes according to the growth of the element. Other than the specific case of *Drosophila* embryo the deformation gradient decomposition method was first used in 1969 by Lee (Lee [1969]). He applied the method for elastic-plastic deformations occurring when both components of strain are finite; doing so, the kinematics are modified to include finite elastic and plastic strain components. Particularly, he introduced two coupled thermodynamic systems: one compromising termo-elasticity at finite strain and the other the irreversible process of dissipation and absorption of plastic work. For what concerns biomechanics, Rodriguez (Rodriguez et al. [1994]) studied cardiac hypertrophy during which alterations in wall stress arising from changes in mechanical loading lead to cardiac growth and remodeling. To describe the shape change undergone by an unloaded tissue during growth, he introduced a mapping decomposed into two deformations. The first one indicates the local zero-stress reference state, while the second one is the accompanying elastic transformation that ensures the compatibility of the total deformation. Also Taber (Taber and Perucchio [2000]) used this approach for the analysis of growth, remodeling and morphogenesis of cardiac development. This method is very similar to the one used for the present work, thus in this section we describe it more precisely (for further details please refer to Taber [1995]).

Let us consider a body $B$, which at time $t_0$ is free stress (Fig. B.2); the body is constituted by infinitesimal elements that undergo volumetric growth and that, after

growing, remain stress free. These particular deformations may not be geometrically compatible; thus the elements of $B(t_1)$ must be deformed again in order to make them fit together. Therefore three deformation gradients have to be taken into account:

- the growth deformation gradient $\mathbf{F}_g$, which can be deduced by experiments ;
- the elastic deformation gradient $\mathbf{F}_e$, which allows to maintain the integrity of the body and cause the presence of a residual stress $\boldsymbol{\sigma}_0$;
- the external deformation gradient $\mathbf{F}_l$.

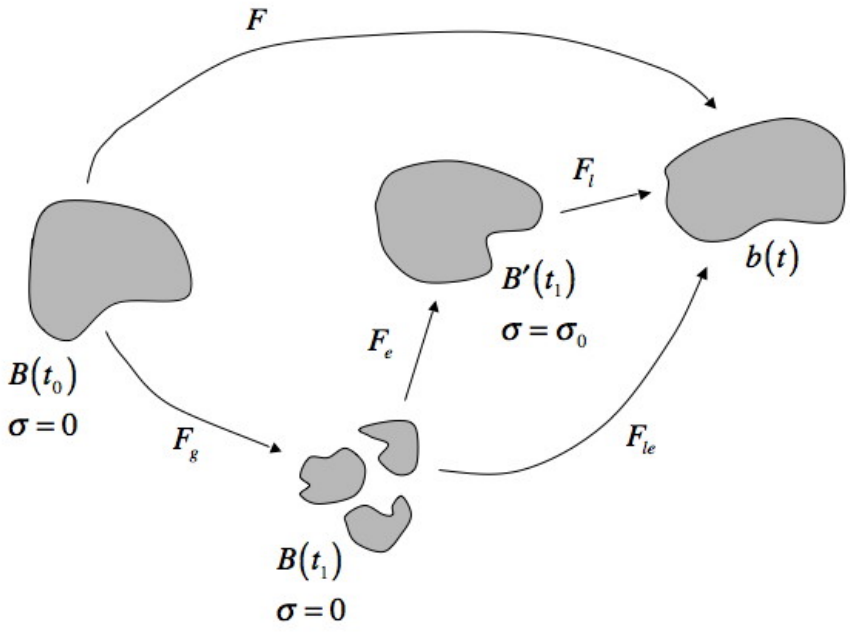


*Figure B.2:* Successive configurations for a growing mass (modified from Taber [1995]).

This is a case of a Lagrangian description where a reference configuration ($B(t_0)$) is chosen and it is not changing through the time. Once the growth completed instead, $B^{'}(t_1)$ can be used as reference for the loading step. The total deformation gradient can be finally expressed as follows

$$\mathbf{F} = \mathbf{F}_l \mathbf{F}_e \mathbf{F}_g \tag{B.5}$$

For what concerns the stresses, two of them are particularly interesting: the residual stress $\boldsymbol{\sigma}_0$, associated to the $B^{'}(t_1)$ configuration, and the total stress $\boldsymbol{\sigma}$ in $b(t)$. To find the residual stress it is necessary that $\mathbf{F} = \mathbf{F}_e\mathbf{F}_g$ with $\mathbf{F}_l = \mathbf{I}$ and traction-free boundary conditions. A similar approach can be used for $\boldsymbol{\sigma}$ but this time $\mathbf{F}_l \neq \mathbf{I}$ and the boundary conditions are inhomogeneous. It has to be notice that the growth is not isovolumic trough the time, therefore $det\,\mathbf{F}_g \neq 1$, specifically $det\,\mathbf{F}_g > 1$ when there is addition of volume and $det\,\mathbf{F}_g < 1$ when remotion occurs. Finally if the material is incompressible, except for the growth, then we have $\mathbf{F}_{le} = \mathbf{F}_l\mathbf{F}_e$.

The previous analysis takes into account the effects of growth on stress, but the inverse process must be considered to know how stress influences growth. So far, even if experimental data pointed out how stress, strain or strain energy can modulate growth, it is not well understood which one of this quantity play the most significant role. However it is possible to write a constitutive relation of a stress-dependent growth as follows

$$\mathbf{F}_g = \mathbf{F}_g(\boldsymbol{\sigma}) \tag{B.6}$$

where $\boldsymbol{\sigma}$ is an implicit fonction of the time. There is another form of the prior equation

$$\dot{\mathbf{F}}_g = \dot{\mathbf{F}}_g(\boldsymbol{\sigma}) \tag{B.7}$$

which results to be more accurate from a physiological point of view since it has been demonstrated that the higher the magnitude of the applied stress, the higher the growth rate. A rigid-body rotational term is included in $\mathbf{F}_g$, but it might not affect the stresses and can be directly reassembled into the deformation provided by $\mathbf{F}_{le}$.

The growth rate of deformation tensor can be obtained, once $\dot{\mathbf{F}}_g$ and $\mathbf{F}_g$ have been determined, from (Rodriguez et al. [1994])

$$\mathbf{D}_g = \frac{1}{2}\left(\dot{\mathbf{F}}_g\mathbf{F}_g^{-1} + \mathbf{F}_g^{-T}\dot{\mathbf{F}}_g^{T}\right) \tag{B.8}$$

where dot indicates the partial differentiation with respect to the time $t$. Furthermore the rate of volumetric growth can be expressed as

$$\frac{1}{V}\frac{dV}{dt} = tr\,\mathbf{D}_g \tag{B.9}$$

with $V$ the growth volume.

# Appendix C

# Special coordinate system

## C.1 Cylindrical polar coordinates

The geometry of the coordinates system is shown in the figure

**Geometry:**

$$(x^1, x^2, x^3) = (r, \theta, z)$$

$$\begin{aligned} x &= r\,cos(\theta) & r &= \sqrt{x^2 + y^2} \\ y &= r\,sin(\theta) & \theta &= arctg\frac{y}{x} \end{aligned}$$

$$\begin{aligned} \mathbf{i}_r &= cos(\theta)\,\mathbf{i}_x + sin(\theta)\,\mathbf{i}_y \\ \mathbf{i}_\theta &= -sin(\theta)\,\mathbf{i}_x + cos(\theta)\,\mathbf{i}_y \\ \mathbf{i}_z &= \mathbf{i}_z \end{aligned}$$

$$\begin{aligned} \mathbf{g}_r &= \mathbf{i}_r \\ \mathbf{g}_\theta &= r\,\mathbf{i}_\theta \\ \mathbf{g}_z &= \mathbf{i}_z \end{aligned}$$

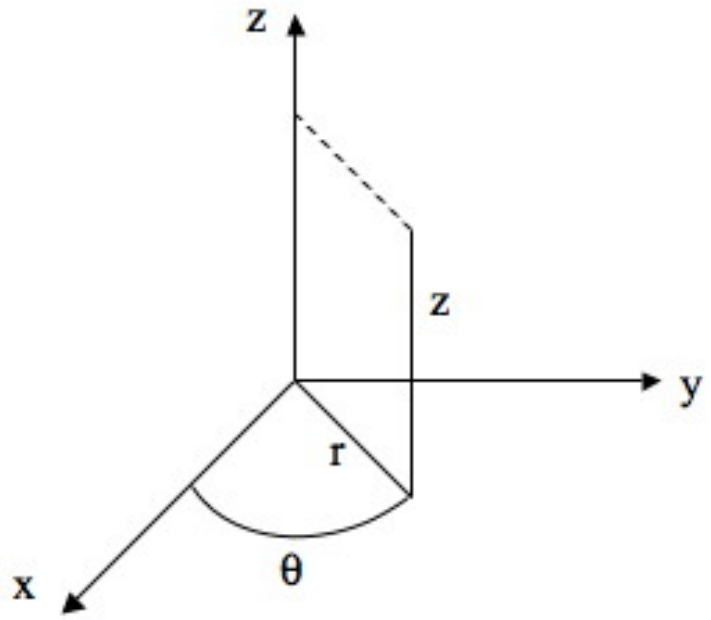


*Figure C.1:* Cylindrical polar coordinates.

**Differential operator:**

$$\boldsymbol{\nabla} = \frac{\partial}{\partial r}\,\mathbf{i}_r + \frac{1}{r}\frac{\partial}{\partial \theta}\,\mathbf{i}_\theta + \frac{\partial}{\partial z}\,\mathbf{i}_z$$

**Deformation gradient:**

$$\mathbf{F}_{\mathbf{i}_i,\mathbf{i}_j} = \begin{bmatrix} \frac{\partial r}{\partial R} & \frac{1}{R}\frac{\partial r}{\partial \Theta} & \frac{\partial z}{\partial Z} \\ r\frac{\partial \theta}{\partial R} & \frac{r}{R}\frac{\partial \theta}{\partial \Theta} & r\frac{\partial \theta}{\partial Z} \\ \frac{\partial z}{\partial R} & \frac{1}{R}\frac{\partial z}{\partial \Theta} & \frac{\partial z}{\partial Z} \end{bmatrix}$$

where $(R, \Theta, Z)$ are the cylindrical coordinates in the reference configuration.

## C.2 Spherical polar coordinates

The geometry of the coordinates system is shown in the figure

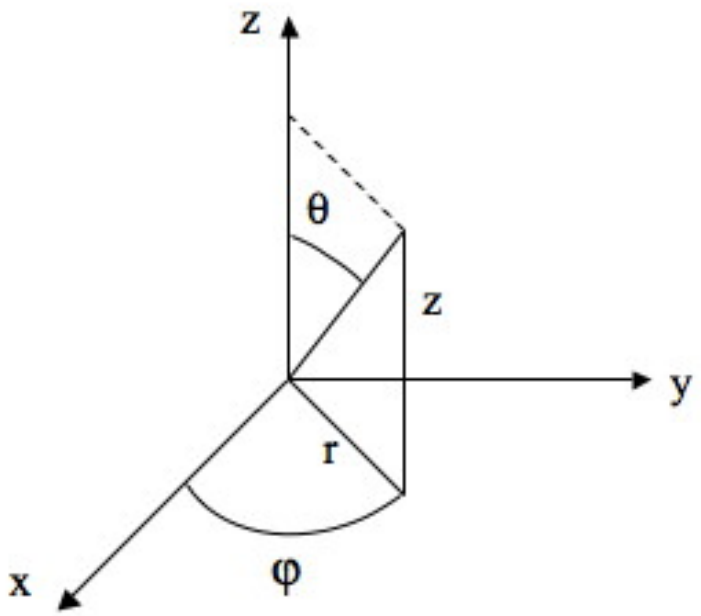


*Figure C.2:* Spherical polar coordinates.

**Geometry:**

$$(x^1, x^2, x^3) = (r, \theta, \varphi)$$

$$\begin{aligned} x &= r\, sin(\theta) cos(\varphi) \\ y &= r\, sin(\theta) sin(\varphi) \\ z &= r\, cos(\theta) \end{aligned}$$

$$\mathbf{g}_1 = \mathbf{i}_x sin(\theta)cos(\varphi) + \mathbf{i}_y sin(\theta)sin(\varphi) + \mathbf{i}_z cos(\theta) = \mathbf{i}_r$$
$$\mathbf{g}_2 = r(\mathbf{i}_x cos(\theta)cos(\varphi) + \mathbf{i}_y cos(\theta)sin(\varphi) - \mathbf{i}_z sin(\theta)) = r\mathbf{i}_\theta$$
$$\mathbf{g}_3 = r\, sin(\theta)(-\mathbf{i}_x sin(\varphi) + \mathbf{i}_y cos(\varphi)) = r\, sin(\theta)\mathbf{i}_\varphi$$

**Differential operator:**

$$\boldsymbol{\nabla} = \mathbf{i}_r \frac{\partial}{\partial r} + \mathbf{i}_\theta \frac{1}{r}\frac{\partial}{\partial \theta} + \mathbf{i}_\varphi \frac{1}{r\, sin(\theta)}\frac{\partial}{\partial \varphi}$$

**Deformation gradient:**

$$\mathbf{F}_{\mathbf{i}_i,\mathbf{i}_j} = \begin{bmatrix} \frac{\partial r}{\partial R} & \frac{1}{R}\frac{\partial r}{\partial \Theta} & \frac{1}{R\, sin\Theta}\frac{\partial r}{\partial \Phi} \\ r\frac{\partial \theta}{\partial R} & \frac{r}{R}\frac{\partial \theta}{\partial \Theta} & \frac{r}{R\, sin\Theta}\frac{\partial \theta}{\partial \Phi} \\ r\, sin(\theta)\frac{\partial \varphi}{\partial R} & \frac{r\, sin(\theta)}{R}\frac{\partial \varphi}{\partial \Theta} & \frac{r\, sin(\theta)}{R\, sin\Theta}\frac{\partial \varphi}{\partial \Phi} \end{bmatrix}$$

# Bibliography


M.D. Adams, S.E. Celniker, and R.A. Holt *et al.* The genome sequence of Drosophila Melanogaster. *Science*, 287:2185–95, 2000.

R. Allena, A.-S. Mouronval, E. Farge, and D. Aubry. Concurrent simulation of morphogenetic movements in *Drosophila* embryo. *IFMBE Proceedings, Springer Berlin Heidelberg*, 287:1829–1832, 2008.

R.J. Asaro and V.A. Lubarda. *Mechanics of solids and materials.* Cambridge, 2006.

K. Barrett, M. Leptin, and J. Settleman. The Rho GTPase and a putative RhoGEF mediate a signaling pathway for the cell shape changes in drosophila gastrulation. *Cell*, 91:905–915, 1997.

L.V. Beloussov. *The dynamic architecture of a developing organism: an interdisciplinary approach to the development of organisms.* Kluwer, Dordrecht, 1998.

L.V. Beloussov and V.I. Grabovsky. Information about a form (on the dynamic laws of morphogenesis). *BioSystems*, 87:204–214, 2007.

L.V. Beloussov and A.V. Lakirev. Generative rules for the morphogenesis of epithelial tubes. *J. Theor. Biol.*, 152:455–468, 1991.

T. Belytschko, W.G. Liu, and B. Moran. *Non linear finite elements for continua and structures.* Wiley, 2000.

G.W. Brodland and D.A. Clausi. Mechanical evaluation of theories of neurulation using computer simulations. *Development*, 118:1013–1023, 1993.

E. Brouzés and E. Farge. Interplay of mechanical deformation and patterned gene expression in developing embryos. *Curr. Opin. Genet. Dev.*, 14:367–74, 2004.

J.A. Campos-Ortega and V. Hartenstein. *The embryonic development of Drosophila Melanogaster.* Springer-Verlag, 1985.

V. Conte, J. Muñoz, and M. Miodownik. A 3D finite element model of ventral furrow invagination in the Drosophila Melanogaster embryo. *Journal of the mechanical behavior of biomedical materials*, 1:188–198, 2008.

M. Costa, D. Sweeton, and E. Wieschaus. How do Sea Urchins invaginate? using biomechanics to distinguish between mechanisms of primary invagination. *Development*, 121:425–465, 1993.

L. Davidson, M.A. Koehl, R. Keller, and G.F. Oster. How do sea urchins invaginate? using biomechanics to distinguish between mechanisms of primary invagination. *Development*, 121:2005–2018, 1995.

L. Davidson, G.F. Oster, R.E. Keller, and M.A.R. Koehl. Measurements of mechanical properties of the blastula wall reveal which hypothesized mechanisms of primary invagination are physically plausible in the Sea Urchin stronglylocentrotus purpuratus. *Dev Biol*, 209:221–238, 1999.

J.A. Davies. *Mechanism of morphogenesis: the creation of biological form.* Elsevier Academic Press, 2005.

N. Desprat, W. Supatto, P.A. Pouille, E. Beaurepaire, and E. Farge. Tissue deformation modulates *twist* expression to determine anterior midgut differentiation in Drosophila embryos. *Developmental cell*, 15:470–477, 2008.

C. Nusslein-Volhard E. Wieschaus and H. Kluding. Kruppel, a gene whose activity is required early in the zygotic genome for normal embryonic segmentation. *Dev Biol*, 104:172–186, 1984.

E. Farge. Mechanical induction of Twist in the Drosophila foregut/stomodeal primordium. *Curr. Biol.*, 13:1365–1377, 2003.

V.E. Foe, G.M. Odell, and B.A. Edgar. Mitosis and morphogenesis in the Drosophila embryo: point and counterpoint. *The development of Drosophila Melanogaster*, pages 149–300, 1993.

G. Forgacs and S.A Newman. *Biological physics of the developing embryo.* Cambridge University press, 2006.

G. Forgacs, R.A. Foty, Y. Shafrir, and M.S. Steinberg. Viscoelastic properties of living embryonic tissues: a quantitative study. *Biophys*, 74:2227–2234, 1998.

H.G. Frohnhofer and C. Nusslein-Volhard. Organization of anterior pattern in the Drosophila embryo by the maternal gene Bicoid. *Nature*, 324:120–125, 1986.

A. Gierer. Physical aspects of tissue evagination and biological form. *Q. Rev. Biophys.*, 10:529–593, 1977.

J. Hardin and L.Y. Cheng. The mechanisms and mechanics of archenteron elongation during Sea Urchin gastrulation. *Dev. Biol.*, 115:490–511, 1986.

G.A. Holzapfel. *Non linear solid mechanics. A continuum approach for engineers.* J Wiley Sons Ltd, 2000.

J.D. Humphrey. Mechanics of the arterial wall: review and directions. *Critical reviews in Biomed. Eng.*, 23:1–162, 1995.

K.D. Irvine and E. Wieschaus. Cell intercalation during Drosophila germ band extension and its regulation by pair-rule segmentation genes. *Development*, 120: 827–41, 1994.

A.G. Jacobson. Computer modeling of morphogenesis. *Am. Zool.*, 20:669–677, 1980.

A.G. Jacobson and R. Gordon. Change in the shape of the developing vertebrate nervous system analyzed experimentally, mathematically and by computer simulation. *J. Exp. Zool.*, 197:191–246, 1976.

A.G. Jacobson, G.F. Oster, G.M. Odell, and L.Y. Cheng. Neurulation and cortical tractor model for epithelial folding. *J. Embryol. Exp. Morph.*, 96:19–49, 1986.

R. Keller. The celular basis of epiboly: a SEM study of deep cell rearrangement during gastrulation in Xenopus Laevis. *J. Embryol. Exp. Morphol.*, 60:201–234, 1980.

R. Keller and P. Tibbetts. Mediolateral cell intercalation in the dorsal axial mesoderm in the Xenopus Laevis. *Dev. Biol.*, 131:539–549, 1989.

R. Keller, J. Shih, and P. Wilson. *Cell motility, control and function of convergence and extension during gastrulation of Xenofus. In* Gastrulation: movements, patterns and molecules. Plenum, 1991a.

R. Keller, J. Shih, P. Wilson, and A. Sater. *Pattern and function of cell motility and cell interactions during convergence and extension in Xenofus. In* 49th Symposium of the Society for Developmental Biology: cell-cell interactions in early development. J Wiley Sons Ltd, 1991b.

R. Keller, L. Davidson, A. Edlund, T. Elul, M. Ezin, D. Shook, and P. Skoglund. Mechanisms of convergence and extension by cell intercalation. *Philos. Trans. R. Soc. Lond. B. Biol. Sci.*, 355:1399, 2000.

R. Keller, L.A. Davidson, and D.R. Shook. How we are shaped: the biomechanics of gastrulation. *Development*, 71:171–205, 2003.

C. Kimmel, R. Warga, and R. Kane. Cell cycles and clonal strings during formation of the Zebrafish central nervous system. *Development*, 120:265–276, 1994.

V. Kolsch, T. Seher, G.J. Fernandes-Ballester, G.J. Serrano, and M. Leptin. Control of Drosophila gastrulation by apical localization of adherens junctions and RhoGEF2. *Science*, 132:384–6, 2007.

T. Lecuit and P.-F. Lenne. Cell surface mechanics and the control of cell shape, tissue patterns and morphogenesis. *Nature reviews*, 8:633–643, 2007.

E.H. Lee. Elastic-plastic deformation at finite strains. *J of Applied Mechanics*, 36: 6, 1969.

A. LeMoigne and J. Foucrier. *Biologie du développement*. Dunod, 2004.

M. Leptin. Drosophila gastrulation: from pattern formation to morphogenesis. *Annu. Rev. Cell Dev.*, 11:189–212, 1995.

M. Leptin. Gastrulation in Drosophila: the logic and the cellular mechanisms. *EMBO J*, 18:3187–3192, 1999.

M. Leptin and B. Grunewald. Cell shape changes during gastrulation in Drosophila. *Development*, 110:73–84, 1990.

J.E. Mitthenthal. The shaping of shell sheets: an application of mechanics in developmental biology. *Biomechanics of cell divisions*, pages 327–346, 1987.

A.S. Mouronval, R. Allena, and D. Aubry. Simulations numériques des mouvements morphogénétiques dans l'embryon de Drosophile: influence de la géométrie initiale. *Proceedings of 9ème Colloque National en calcul de structures, Giens, 25-29 Mai*, 2009.

J. Muñoz and G. Jelenic. Sliding contact conditions using the master-slave approach with application on the geometracally non-linear beams. *Int. J. Solids Struct*, 41: 6963–6992, 2004.

J. Muñoz, K. Barrett, and M. Miodownik. A deformation gradient decomposition method for the analysis of the mechanics of morphogenesis. *Journal of Biomechanics*, 40:1372–1380, 2007.

A. Nicolas, B. Geiger, and S. A. Safran. Cell mechanosensitivity controls the anisotropy of focal adhesions. *PNAS*, 101:12520–12525, 2004.

H. Oda and S. Tsukita. Real-time imaging of cell-cell adherens junctions reveals that Drosophila mesoderm invagination begins with two phases of apical constriction of cells. *Journal of cell science*, 114:493–501, 2000.

G.M. Odell, G. Oster, O. Alberch, and P. Burnside. The mechanical basis of morphogenesis. I. Epithelial folding and invagination. *Dev. Biology*, 85:446–462, 1981.

S. Osher and R. Fedkiw. *Level set method and dynamic implicit surfaces*. Springer, 2003.

G.F. Oster and O. Alberch. Evolution and bifurcation of developmental programs. *Evolution*, 36:444–459, 1982.

PA. Pouille and E. Farge. Hydrodynamic simulation of multicellular embryo invagination. *Physical biology*, 5:015005, 2008.

A. Ramasubramanian and L.A. Taber. Computational modelling of morphogenesis regulated by mechanical feedback. *Biomechan. Model. Mechanobiol.*, 7:77–91, 2006.

L.T. Reiter. A systematic analysis of human disease-associated gene sequences in Drosophila Melanogaster. *Genome Res*, 11(6):1114–25, 2001.

E.K. Rodriguez, A. Hoger, and A.D. McCulloch. Stress-dependent finite growth in soft elastic tissues. *Journal of Biomechanics*, 27:455–467, 1994.

S. Roth. *Gastrulation in other insects*. Cold Spring Harbor Laboratory Press, 2004.

G.C. Schoenwolf and I. Alvarez. Roles of neuroepithelial cell rearrangement and division shaping of the avian neural plate. *Development*, 106:427–439, 1989.

J.A. Sethian. *Level set method*. Cambridge University Press, 1996.

F. Sidoroff. Variables internes en viscoelasticité. milieux avec plusieurs configurations intermédiaires. *Journal de mécanique*, 15, 1976.

D. Smith. *An introduction to continuum mechanics*. Kluwer Academic Publisher, 1993.

W. Supatto. *Imagérie multiphoton quantitative et ablation laser par impulsions femtosecondes pour l'étude de l'expression génétique mécano-sensible chez l'embryon de Drosophile sauvage*. PhD thesis, Institut Curie Laboratoire Physico-Chimie, 2005.

W. Supatto, D. Débarre, B. Moulia, E. Brouzés, J.-L. Martin, and E. Farge. In vivo modulation of morphogenetic movements in drosophila embryos with femtosecond laser pulses. *PNAS*, 102:1047–1052, 2005.

D. Sweeton, S. Parks, M. Costa, and E.Wieschaus. Gastrulation in Drosophila: the formation of the ventral furrow and posterior midgut invaginations. *Development*, 112:775–789, 1991.

L.A. Taber. Biomechanics of growth, remodeling and morphogenesis. *Appl. Mech. Rev.*, 48(8):487–545, 1995.

L.A. Taber. *Non linear elasticity: applications in biomechanics.* World Scientific Publ, 2004.

L.A. Taber. Theoretical study of Beloussov's hyper-restoration hypothesis for mechanical regulation of morphogenesis. *Biomechan. Model. Mechanobiol.*, 7(6):427–441, 2007.

L.A. Taber and R. Perucchio. Modeling heart development. *Journal of elasticity*, 61:165–197, 2000.

O. Traub and B.C. Berk. Laminar shear stress. mechanisms by which endothelial cells transduce an atheroprotective force. *Arteriosclerosis, thrombosis and vascular biology*, 18:677–685, 1998.

A. Vincent, J.T. Blankenship, and E. Wieshaus. Integration of the head and trunk segmentation systems controls cephalic furrow formation in Drosophila. *Development*, 124:3747–3754, 1997.

C. H. Waddington. *Organizers and genes.* Cambridge University press, 1940.

M. Weliky and G. Oster. The mechanical basis of cell rearrangement. *Development*, 106:372–386, 1990.

M. Weliky, S. Minauk, R. Keller, and G. Oster. Notochored morphogenesis in Xenopus Laevis: simulation of cell behavior underlying tissue convergence and extension. *Development*, 113:1231–1244, 1991.

C. Wiebe and G. Brodland. Tensile properties of embryonic epithelia measured using a novel instrument. *Journal of Biomechanics*, 38:2087–2094, 2005.

D. Zinemanas and A. Nir. Fluid mechanical simulations of cell furrowing due to anisotropic surface forces. *Trends in Genetics*, 21, 1987.

S.B. Zusman and E. Wieshaus. Requirements for zygotic gene activity during gastrulation in Drosphila Melanogaster. *Dev. Biol.*, 111:359–371, 1985.